1 2 9 0

UNIVERSIDADE Ð
COIMBRA

Ariana Coelho Ferreira dos Santos

The Solid Products of *L*–arginine and Divalent Metal Ions – Synthesis, Physicochemical Characterization and Biological Properties.

Dissertação no âmbito do Mestrado em Química Medicinal orientada pela Professora Doutora Lígia Salgueiro, pela Professora Doutora Agnieszka Wojciechowska e pela Professora Doutora Maria José Gonçalves, e apresentada ao Departamento de Química da Faculdade de Ciências e Tecnologia da Universidade de Coimbra

November 2020

Ariana Coelho Ferreira dos Santos

The solid products of *L*−arginine and divalent metal ions – synthesis, physicochemical characterization and biological properties

Dissertação apresentada para as provas do Mestrado em Química Medicinal

Orientação:

Professora Doutora Lígia Salgueiro

Professora Doutora Agnieszka Wojciechowska

Professora Doutora Maria José Gonçalves

Novembro 2020

Universidade de Coimbra

Acknowledgements

Since I was little, I remember people saying "*Slow and steady wins the race*" and it is true. Step by step I built my way and, after 5 years, here I am ready to close another chapter of my life. It has been 5 years of conquers, good memories and some challenges.

I came to Poland to start my thesis project and I could not be prouder of myself. I went alone and it was scaring at the beginning. I was afraid of going to a "new world" just by myself. I was going to meet different people with different costumes and leaving my comfort zone… but now I see it was worth it! I am very thankful to Professor Agnieszka Wojciechowska for all her help and unconditional support during the first semester.

To Professor Maria José Gonçalves that helped me in the second part of this adventure and was always available to clarify my doubts. To Professor Lígia Salgueiro for her orientation, without leaving me apart. To all pharmacognosy group for accepting me so well.

From the bottom of my heart, a very special thank you to Professor António Paixão, that also helped me in the concretization of my master thesis.

To my family, my shelter, for making this journey possible. Without them, nothing of this would be possible! To my mom, for all her support and patience to hear me and advise me when things were not going in the best way. To my dad, for always knowing what to say and giving me the tranquility I need. To my sister, for being my best friend and for always saying "*Go! Take the risk*". To my grandparents, because they are the stars that light and guide my way. They got my back.

To my friends, for all the good shared moments.

A very deep thank you to Professor Ermelinda Eusébio and all the remaining Molecular Thermodynamics and Solid State Chemistry Laboratory research group for all the help and wisdom they gave me!

And last, but not the least, to Roque. I must express my deepest appreciation for the guidance, friendship and advices that this amazing person gave me! Since my first year, he was there to help and support me, so thank you. Without you, I would not have grown as much as a person or as a professional.

Thank you all of you! Thank you Coimbra.

Ariana Santos

“Keep your eyes on the stars and your feet on the ground.”

Theodore Roosevelt

Contents

Abstract ... ix

Resumo ... xi

Nomenclature and abbreviations ... xiii

  Nomenclature ... xiii

  Abbreviations ... xv

Figures index ... xvii

Tables index ... xxi

Equations index ... xxiii

Introduction ... 3

1.1. Metal complexes ... 3

  1.1.1. Werner's theory of coordinated compounds ... 3

  1.1.2. Ligands ... 5

  1.1.3. Crystal Field Theory ... 8

  1.1.4. Applications of coordination compounds in the bioinorganic chemistry field ... 12

1.2. Objectives ... 17

Experimental section: Materials and methods ... 21

2.1. Materials ... 21

2.2. Methods ... 22

  2.2.1. Preparation of the solutions ... 22

  2.2.2. General synthesis of the complexes ... 22

  2.2.3. Single crystal and powder X-Ray diffraction ... 23

  2.2.4. Infrared spectroscopy ... 23

  2.2.5. Magnetic studies ... 23

  2.2.6. Antimicrobial activity ... 24

Results and discussion ... 25

3.1. Synthesis of the complexes ... 27

3.2. X-Ray diffraction analysis and structure determination.. 30

3.3. Infrared spectroscopy 46

3.3. Magnetic properties... 53

3.4. Antimicrobial studies 57

Conclusions and future perspectives 61

References 63

Supplementary material... 73

Abstract

Two of the biggest purposes in Medicinal Chemistry are to synthetize new drugs or to increase the quality/potency of the ones that are commercially available, while limiting side-effects. The present work focused on the synthesis of new coordination compounds. Over the years, metal-based compounds have shown, in general, noteworthy improved biological activities comparing to the parent standalone drug. In this endeavor, it was attempted the synthesis of new metal complexes with calcium(II), magnesium(II), copper(II) and zinc(II) ions as the central metal atoms. Eight coordination compounds were successfully synthesized from the copper(II) salts. Besides *L*−arginine (an important amino acid involved in several biological functions), the chemically alike SCN^- and N_3^- ions were used as ligands in order to understand its structural effect in the metal complex, *i.e.* whether they would serve only as counterions to balance the positive charge of [metal−*L*−arginine] cations, or if they were also able to coordinate with the metal ion and consequently originate coordination compounds with diverse and unique geometries.

All of the single-crystals of all the obtained products, $\{[Cu(L{-}arg)_2](NO_3)_2{\bullet}3H_2O\}_n$ **(1)**, $[Cu(L{-}arg)_2(SCN)_2]{\bullet}2H_2O$ **(2)**, $[Cu(L{-}arg)(SCN)_2]$ **(3)**, $[Cu(L{-}arg)_2(N_3)_2][Cu(L{-}arg)_2Cl](N_3){\bullet}7H_2O$ **(4)**, $\{[Cu_2(L{-}arg)_2(N_3)_2(\mu{-}1,3{-}N_3)(\mu{-}1,1{-}N_3)][Cu(L{-}arg)(N_3)(\mu{-}1,1{-}N_3)]{\bullet}3H_2O\}_n$ **(5)**, $[Cu(L{-}arg)_2(N_3)_2][Cu(L{-}arg)_2(N_3)](N_3){\bullet}6H_2O$ **(6)**, $[Cu(L{-}arg)_2(H_2O)_2](N_3)_2$ **(7)** and $\{[Cu(L{-}arg)(N_3)(\mu{-}1,3{-}N_3)]\}_n$ **(8)** were synthetized by slow crystallization from aqueous solutions. The morphology and color of the synthesized crystals were unique for each metal complex. The metal complexes were characterized by the means of single-crystal and powdered X-ray crystallography and infrared spectroscopy. The single-crystal structure of products 1 and 3 has already been solved, whereas for the remaining products were solved for the first time.

Due to the paramagnetic properties of copper(II) ions, and to establish a magneto-structural correlation, magnetic studies for all the metal complexes (T = 1.8−300 K) were also carried out, except for products 1 and 3 (already described in literature) and for product 5 (as a result of low quantity of material). Only product 8, with greenish single-crystals showed weak ferromagnetic interactions, *i.e.* below a certain temperature, the atomic magnetic moments tended to line up in a common direction. The others (products 2, 4, 6 and 7) presented the normal behavior of a paramagnetic specie, *i.e.* when exposed to an external magnetic field, the paramagnetic ions acquired a small magnetization.

Finally, the antimicrobial activity of the majority of the products was evaluated against *Candida albicans*, *Candida tropicalis*, *Trichophyton mentagrophytes*, *Microsporum gypseum* and *Epidermophyton floccosum* (fungi strains) and against *Escherichia coli* and *Staphylococcus aureus* (bacteria strains). All the products showed strong activity against dermatophytes. In particular products 3, 7 and 8 are highlighted for a much better MIC value comparing to the standard drug (Fluconazole). The tested products did not show activity against yeasts or bacteria in the tested concentrations.

Keywords: copper(II)−*L*−arginine complexes, X−ray crystallography, infrared spectroscopy, magnometry, antimicrobial activity.

Resumo

Dois dos grandes objetivos em Química Medicinal são sintetizar novos fármacos e aumentar a qualidade/potência dos que já se encontram comercialmente disponíveis, ao mesmo tempo que se pretende diminuir os efeitos secundários. Visto que, ao longo dos anos, os compostos de coordenação têm mostrado, de forma geral, propriedades biológicas bastante melhoradas em relação à molécula livre de origem, o trabalho apresentado na presente dissertação focou-se na síntese desses mesmos compostos.

Neste sentido, tentou-se sintetizar novos complexos metálicos contendo cálcio(II), magnésio(II), cobre(II) e zinco(II) como átomos metálicos centrais. Apenas com o cobre(II) se conseguiu obter, com sucesso, oito compostos de coordenação. Por sua vez, como ligandos recorreu-se ao uso da *L*−arginina (por se tratar de um aminoácido importante em diferentes processos biológicos), bem como aos iões SCN^- e N_3^-, por serem quimicamente muito idênticos. O recurso a estes aniões teve como objetivo perceber qual o efeito estrutural dos mesmos nos complexos metálicos, isto é, se apenas serviriam como contra-ião para balançar a carga positiva proveniente do catião [metal:*L*−arginina] ou se também eram capazes de coordenar com o ião metálico central e, consequentemente, originar compostos de coordenação com geometrias diversas e únicas.

Todos os mono-cristais dos compostos sintetizados $\{[Cu(\mathit{L}{-}arg)_2](NO_3)_2{\bullet}3H_2O\}_n$ **(1)**, $[Cu(\mathit{L}{-}arg)_2(SCN)_2]{\bullet}2H_2O$ **(2)**, $[Cu(\mathit{L}{-}arg)(SCN)_2]$ **(3)**, $[Cu(\mathit{L}{-}arg)_2(N_3)_2][Cu(\mathit{L}{-}arg)_2Cl](N_3){\bullet}7H_2O$ **(4)**, $\{[Cu_2(\mathit{L}{-}arg)_2(N_3)_2(\mu{-}1{,}3{-}N_3)(\mu{-}1{,}1{-}N_3)][Cu(\mathit{L}{-}arg)(N_3)(\mu{-}1{,}1{-}N_3)]{\bullet}3H_2O\}_n$ **(5)**, $[Cu(\mathit{L}{-}arg)_2(N_3)_2][Cu(\mathit{L}{-}arg)_2(N_3)](N_3){\bullet}6H_2O$ **(6)**, $[Cu(\mathit{L}{-}arg)_2(H_2O)_2](N_3)_2$ **(7)** e $\{[Cu(\mathit{L}{-}arg)(N_3)(\mu{-}1{,}3{-}N_3)]\}_n$ **(8)**, foram obtidos a partir de soluções aquosas através da cristalização lenta. A morfologia, bem como as cores de cada cristal, foram únicas para cada complexo metálico. Todos os complexos metálicos foram caracterizados por cristalografia de raios-X de cristal e de pó e por espectroscopia de infravermelho, concluindo-se que a estrutura cristalina dos produtos 1 e 3 já tinha sido resolvida, ao passo que todas as restantes foram resolvidas pela primeira vez.

Uma vez que os iões cobre(II) apresentam propriedades paramagnéticas, foram realizados estudos magnométricos para todos os complexos metálicos ($T = 1.8{-}300$ K), exceto para os produtos 1 e 3, que já se encontravam descritos na literatura, e para o produto 5, por não haver uma quantidade de material suficiente. Estes estudos tiveram como objetivo poder estabelecer uma correlação magneto-estrutural. Apenas o produto 8, cujos mono-cristais obtidos eram esverdeados, mostrou ter interações ferromagnéticas residuais, isto é, abaixo de uma certa temperatura, os momentos magnéticos atómicos tenderam em alinhar-se na mesma direção. Todos os restantes (produtos 2, 4, 6 e 7) mostraram ter um comportamento normal de paramagnetismo, ou seja, na presença de um campo magnético externo, os iões metálicos paramagnéticos ficaram magnetizados.

Finalmente, a atividade antimicrobiana da maioria dos compostos foi avaliada contra várias estirpes de leveduras e fungos filamentosos (*Candida albicans*, *Candida tropicalis*, *Trichophyton mentagrophytes*, *Microsporum gypseum* e *Epidermophyton floccosum*) e contra as bactérias *Escherichia coli* e *Staphylococcus aureus*. Todos os produtos mostraram uma forte atividade inibitória contra os dermatófitos. Em particular, sublinha-se a atividade dos compostos 3, 7 e 8 que apresentaram um melhor valor de MIC relativamente ao fármaco de referência (Fluconazole). Todos os produtos não apresentaram atividade contra as leveduras e bactérias no intervalo de concentrações testadas.

Palavras-chave: complexos de cobre(II)−*L*−arginina, cristalografia de raios-X, espectroscopia de infravermelho, magnometria, atividade antimicrobiana.

Nomenclature and abbreviations

Nomenclature

The nomenclature used in the present dissertation followed, in a general terms, the International Union of Pure and Applied Chemistry (IUPAC) standarts.[1]

The molecular nomenclature of the metal complexes was defined by the following procedure: the coordination sphere of the coordination compounds were placed within square brackets [ ]. These include the chemical symbol of the metal central ion, which was written first, and then the symbols or abbreviations of the ligands, which were placed within parentheses ( ). In the case of identical coordinated ligands, a right subscript following the enclosing marks was used to specify its amount. Bridging ligands, *i.e.* ligands that are coordinated to more than one central metal, were referred by a "µ" prefix followed by a hyphen and the rest of the ligands' name. The polymeric nature of the metal complex, if applied, was indicated by braces { } followed by an "n" letter in subscript. Finally, and separated by a central dot, it is specified the amount and the chemical designation of hydrates. Two illustrative examples of the metal complexes structure and nomenclature are shown in Table 1.

Table 1 – Schematic structure and nomenclature of two exemplificative coordinated compounds.

Description	**Molecular nomenclature**[a]	**Schematic illustration**
Di-hydrated metal complex with five L_B and one L_R ligands.	$[M(L_B)_5(L_R)]\bullet 2H_2O$	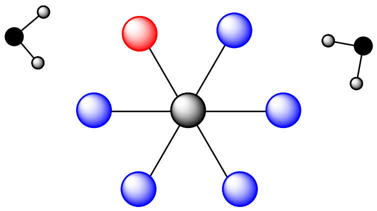
Metal complex with two different bridging ligands, L_B and L_R.	$[M_2(\mu\text{-}L_B)(\mu\text{-}L_R)(L_B)_4]$	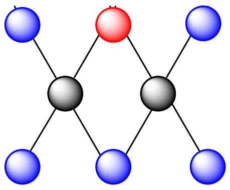

[a] M – central metal ion; L_B – blue ligand; L_R – red ligand

The vibrational characterization of the synthetized metal complexes, used in the present dissertation, followed the vibrational modes designation shown in Table 2.

Table 2 – Designation and representation of the atom displacement during vibrational motion.

Designation of the vibration mode	**Symbol used in this work**	**Schematic representation**[a)]
Stretching – successive distension and contraction of one or more chemical bonds.	$\nu_{as}(\ )$	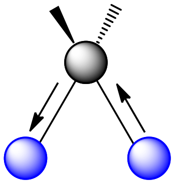 Asymmetric
	$\nu_{s}(\ )$	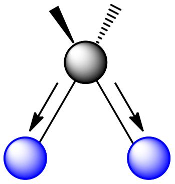 Symmetric
In-plane deformation vibration (scissoring)[b)] – displacement of two atoms in the ABA plane, leading to changes in valence angles.	$\delta(\ )$	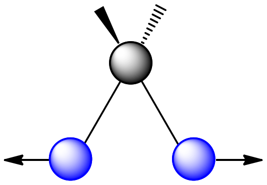 Scissoring
Out-of-plane deformation vibration (wagging)[b)] – displacement of two atoms out of the ABA plane, leading to changes in dihedral angles.	$\omega(\ )$	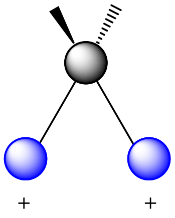 Wagging

[a)] The atoms in blue are designated by the letter A and the atoms in black are designated by the letter B. Due to simplification matters, the displacement of the central atom (black) is not shown.

[b)] Rocking and twisting are also in-plane and out-of-plane deformation vibrations, respectively. However, during the course of this dissertation, such vibrations will not be discussed.

Abbreviations

MC: metal complex

IUPAC: international union of pure and applied chemistry

CN: coordination number

CFT: crystal field theory

ROS: reactive oxygen species

LPS: lipopolysaccharide

MW: molecular weight

FT-IR: Fourier transformed infrared spectroscopy

ATCC: American type culture collection

CECT: colección Española de cultivos tipo

SDA: sabouraud dextrose agar

PDA: potato dextrose agar

MHA: Muller Hinton agar

RPMI: Roswell Park Memorial Institute medium

MIC: minimal inhibitory concentration

MLC: minimal lethal concentration

CLSI: clinical and laboratory standards institute

ZFC: zero field cooled

FC: field cooled

Figures index

Chapter 1

Figure 1. 1 – Two $[Co(NH_3)_4Cl_2]^+$ cations with different properties due to different arrangements of the same ligands. The a) *cis*−$[Co(NH_3)_4Cl_2]$ complex unit presents a red color, whereas the b) *trans*−$[Co(NH_3)_4Cl_2]$ complex unit has a green color. *Picture created with BioRender.com*. Adapted from ref. [13] 4

Figure 1. 2 – Structure of guanidine and its conjugated acid guanidinium. The dashed bonds represent the electrons resonance in guanidinium cation (so-called Y aromaticity). 5

Figure 1. 3 – Comparison of Netropsin and a $[Cu(L{-}Arg)_2]^{2+}$ complex cation that behaves as a structural mimic of the antibiotic. The inset highlights the (guanidinium) end group similarities. *Picture created with ChemDraw*. 6

Figure 1. 4 – Net atomic charges of the neutral form of *L*−arginine (values taken from ref. [27]). *Picture created with ChemDraw.* 6

Figure 1. 5 – Resonance structures of a) SCN^- and b) N_3^- ions. *Picture created with ChemDraw.* 7

Figure 1. 6 – Schematic representation of the five types of *d*-orbitals. The d_{z^2} orbital has maximum amplitude along the z axis, whereas $d_{x^2-y^2}$ has maximum amplitude along the x and y axes. On the other hand, the d_{xy}, d_{xz} and d_{yz} orbitals have maximum amplitude at 45º of x and y axes, x and z axes and y and z axes, respectively. *Picture created with ChemDraw.* 8

Figure 1. 7 – Schematic representation of the *d*-orbitals energy splitting in an a) octahedral field and b) tetrahedral field. Two types of *d*-orbitals ($d_{x^2-y^2}$ and d_{xy}) are illustrated to showcase the repulsion between the electrons of the orbitals and the incoming ligands. The energy splitting is represented in relative terms (Δ_o and Δ_r), where "o" and "r" correspond to octahedral and tetrahedral fields, respectively. *Picture created with ChemDraw.* Adapted from ref.[41] 10

Figure 1. 8 – Representation of the typical magnetic susceptibility of paramagnetic substances with the variation of temperature. *Picture created with BioRender.com*. Adapted from ref. [45] 12

Figure 1. 9 – Structural differences of Gram-negative and Gram-positive bacteria. The former ones have a more complex cell wall structure with an outer and inner membrane and a periplasmic space, while the latter have only a peptidoglycan cell wall and a plasma membrane. *Picture created with BioRender.com.* Adapted from ref. [74] 15

Figure 1. 10 –Schematic representation of the formation of the fungi cell wall and cell membrane. The cell wall is constituted mainly by different polysaccharides (β−glucans), whereas the cell membrane is constituted essentially by lipids. The 14α−demethylase is a cytochrome P450-dependent enzyme that allows the transformation of lanosterol to ergosterol. *Picture created with BioRender.com.* Adapted from ref. [79] 16

Chapter 3

Figure 3. 1 – Single-crystals obtained from the different synthetized products (1-8). 29

Figure 3. 2 – a) Unit cell of $[Cu(L{-}arg)_2](NO_3)_2{\bullet}3H_2O$ (1) single-crystals and b) 1D coordination polymer with atom numbering. The hydrogen atoms in b) were omitted for clarity. 31

Figure 3. 3 – PXRD pattern obtained for (1) (black line). The blue line diffractogram (at the bottom) shows the predicted positions and relative intensity of peaks calculated from the crystal structure obtained from the single X-ray diffraction. 32

Figure 3. 4 –Unit cell of a) $[Cu(L{-}arg)_2(SCN)_2]{\bullet}2H_2O$ (2) and of b) $[Cu(L{-}arg)(SCN)_2]$ (3) single-crystals with atom numbering. 34

Figure 3. 5 – PXRD patterns obtained for a) (2) and for b) (3) (black line). The blue line diffractograms (at the bottom) show the predicted positions and relative intensity of peaks calculated from the crystal structure obtained from the single X-ray diffraction. In product 2, the intensity of the peak marked with a tilde (~) was truncated. 35

Figure 3. 6 – Unit cell of a) $[Cu(L{-}arg)_2(N_3)_2][Cu(L{-}arg)_2Cl](N_3){\bullet}7H_2O$ (4) and b) $[Cu(L{-}arg)_2(N_3)_2][Cu(L{-}arg)_2(N_3)](N_3){\bullet}6H_2O$ (6) single-crystals with atom numbering. 37

Figure 3. 7 – Unit cell of $[Cu(L{-}arg)_2(H_2O)_2](N_3)_2$ (7) single-crystals with atom numbering. 39

Figure 3. 8 – PXRD patterns obtained for a) (4), b) (6) and c) (7) (black line). The blue line diffractograms (at the bottom) show the predicted positions and relative intensity of peaks calculated from the crystal structure obtained from the single X-ray diffraction. The inset highlights the mismatch between the experimental data (black line) and the theoretical one (blue line). The intensity of the peaks marked with a tilde (~) was truncated. 41

Figure 3. 9 – Unit cell of a) $\{[Cu_2(L{-}arg)_2(N_3)_2(\mu{-}1,3{-}N_3)(\mu{-}1,1{-}N_3)][Cu(L{-}arg)(N_3)(\mu{-}1,1{-}N_3)]{\bullet}3H_2O\}_n$ (5) and b) $\{[Cu(L{-}arg)(N_3)(\mu{-}1,3{-}N_3)]\}_n$ (8) single-crystals with atom numbering. 44

Figure 3. 10 – PXRD pattern obtained for (8) (black line). The blue line diffractogram (at the bottom) shows the predicted positions and relative intensity of peaks calculated from the crystal structure obtained from the single X-ray diffraction. The intensity of the peak marked with a tilde (~) was truncated. 46

Figure 3. 11 – FT-IR spectra of product 1 (black line) and *L*-arginine (blue line). 46

Figure 3. 12 – FT-IR spectra of product 2 (black line) and 3 (red line). The inset highligts the [2200 – 1200 cm^{-1}] region. 47

Figure 3. 13 – FT-IR spectra of products 4 (black line), 6 (red line) and 7 (green line). The inset highligts the [2200 – 1200 cm^{-1}] region. 48

Figure 3. 14 – FT-IR spectra of products 5 (black line) and 8 (red line). The inset highligts the [2200 – 1200 cm^{-1}] region. 49

Figure 3. 15 –Vibrational normal modes of the SCN^- ion. a) C−N stretching ν(CN), b) C−S stretching ν(CS) and c) degenerated in-plane and out-of-plane bending modes δ(NCS). Adapted from ref. [143]. 50

Figure 3. 16 – FT-IR spectra of pure KSCN (orange line), and of products 2 and 3 (black and red lines, respectively). 50

Figure 3. 17 –Vibrational normal modes of the N_3^- ion. a) asymmetric stretching $\nu_{as}(N_3)$, b) symmetric stretching $\nu_s(N_3)$ and c) degenerated in-plane and out-of-plane bending modes $\delta(N_3)$. Adapted from ref. [143]......51

Figure 3. 18 – FT-IR spectra of pure NaN_3 (orange line), and of products 4 (black), 5 (red), 6 (green), 7 (pink) and 8 (blue)......52

Figure 3. 19 – a) Representation of the magnetic molar susceptibility *versus* temperature and b) representation of the effective magnetic moment *versus* temperature for product 2. 54

Figure 3. 20 –Representation of the magnetic molar susceptibility *versus* temperature for a) (4) and for b) (6)......55

Figure 3. 21 –Representation of the effective magnetic moment *versus* temperature for a) (4) and for b) (6)......55

Figure 3. 22 – a) Representation of the magnetic molar susceptibility *versus* temperature and b) representation of the effective magnetic moment *versus* temperature for product 7. 56

Figure 3. 23 – a) Representation of the magnetic molar susceptibility *versus* temperature and b) representation of the effective magnetic moment *versus* temperature for product 8. 56

Figure 3. 24 – Isothermal magnetization (M) curves for products 2, 4, 6, 7 and 8. 57

Tables index

Chapter 1

Table 1. 1 – Schematic geometrical structures of the metal complexes according to their coordination number. 4
Table 1. 2 – Examples of two biologically active metal complexes, containing either SCN^{-} or N_3^{-} ligands. 8
Table 1. 3 – Examples of transition-metal complexes, containing *L*−arginine ligands, with enhanced biological activities. 13

Chapter 3

Table 3. 1 – Summary table of the synthesis of Cu(II) complexes. 28
Table 3. 2 – Crystallographic data and X-ray experimental details for (1). 31
Table 3. 3 – Selected geometric parameters (Å, deg) for (1), obtained by the X-ray diffraction studies. 31
Table 3. 4 – Crystallographic data and X-ray experimental details for (2) and (3). 34
Table 3. 5 – Selected geometric parameters (Å, deg) for (2) and (3) obtained by the X-ray diffraction studies. 34
Table 3. 6 – Crystallographic data and X-ray experimental details for (4) and (6). 38
Table 3. 7 – Selected geometric parameters (Å, deg) for (4) and (6) obtained by the X-ray diffraction studies. 38
Table 3. 8 – Crystallographic data and X-ray experimental details for (7). 39
Table 3. 9 – Selected geometric parameters (Å, deg) for (7) obtained by the X-ray diffraction studies. 40
Table 3. 10 – Crystallographic data and X-ray experimental details for (5) and (8). 44
Table 3. 11 – Selected geometric parameters (Å, deg) for (5) and (8) obtained by the X-ray diffraction studies. 45
Table 3. 12 – Vibrational frequencies (in cm^{-1}) of the $\nu(CN)$, $\nu(CS)$ and $\delta(NCS)$ bands for the pure KSCN and for the coordinated one (in products 2 and 3). 51
Table 3. 13 – Vibrational frequencies (in cm^{-1}) of the $\nu_{as}(N_3)$, $\nu_s(N_3)$, $\delta(N_3)$ and $\nu(MN)$ bands for the pure NaN_3 and for the coordinated one (in products 4-8). 52
Table 3. 14 - Antimicrobial activity of products 1, 2, 3, 4, 6, 7 and 8 against dermatophytes strains. 59

Equations index

Chapter 1

Eq.1. 1 11
Eq.1. 2 11
Eq.1. 3 11

Chapter 3

Eq.3. 1 37
Eq.3. 2 53
Eq.3. 3 53
Eq.3. 4 54

Chapter 1.

Introduction

1. Introduction

1.1. Metal complexes

A metal complex (MC), also called coordination compound, corresponds to an assembly of a metallic central atom coordinated with other molecular fragments, named ligands.[1,2] These ligands act as Lewis bases by sharing electrons and forming dative bonds with the metal ion. The central metal ion, on the other hand, behaves as a Lewis acid, *i.e.* as an electrons-pair acceptor.[1,3,4] This electrons-acceptor behavior of the metal ions towards ligands is very important to describe and/or understand the metal−ligand(s) interactions and can be generally divided into two classes: i) *hard* acids (or class A cations) and ii) *soft* acids (or class B cations).[4] According to the International Union of Pure and Applied Chemistry (IUPAC), a *hard* acid is *"a Lewis acid with an acceptor centre of low polarizability"*.[5] A *hard* acid prefers to coordinate, according to Hard Soft Acid Base (HSAB) theory, with a similar nonpolarizable ligand, *i.e.* a *hard* base. Conversely, a *soft* acid (that *"possesses an acceptor centre of high polarizability"*)[5] prefers to coordinate with a *soft* base.[4,6,7]

A transition-metal complex has a central atom that belongs to the *d*-block of the periodic table. According to IUPAC's definition, a transition metal is *"an element whose atom has an incomplete d sub-shell, or which can give rise to cations with an incomplete d sub-shell"*.[1] This feature, besides affecting their electronic configuration, also leads to a variable possibility of oxidation states, allowing transition metals to undergo oxidation and reduction reactions.[8,9,10,11] These *d*-block metals tend to interact and coordinate with biological ligands and, therefore, are able to provide a wide range of MC with unique geometry shapes, playing a central role in the bioinorganic chemistry field.[8,12]

1.1.1. Werner's theory of coordinated compounds

A "MC with unique geometry shapes", as mentioned above, is a result of a dynamic coordination system between the central metal ion and the (biological) ligand. In fact, the geometry of the MC depends not only on the metal ion, including its oxidation states, but also on the ligands that are coordinated.[2,8] Alfred Werner studied several metal halide complexes with ammonia. In his pioneering work, he synthetized two different $[Co(NH_3)_4Cl_2](Cl)$ coordination compounds and ascertained that, although their chemical composition was the same, the physical and chemical properties differed between each other (for example, one of the products was red while the other had the green color).[13] He thought that if the chemical composition was the same, the physical and chemical properties could only be related with the way how ligands were linked to the central metal ion. He recognized that the MC were geometrically different, having *cis*− and *trans*−conformations (see Figure 1. 1).[14] Furthermore, he postulate that the central atom contains two types of valency: i) primary valency, known as oxidation state, and ii) secondary valency, or coordination number. The primary valency is defined according to the positive charge in the central metal ion, while the secondary valency is associated with the number of ligands that are bonded to the central atom.[15,16]

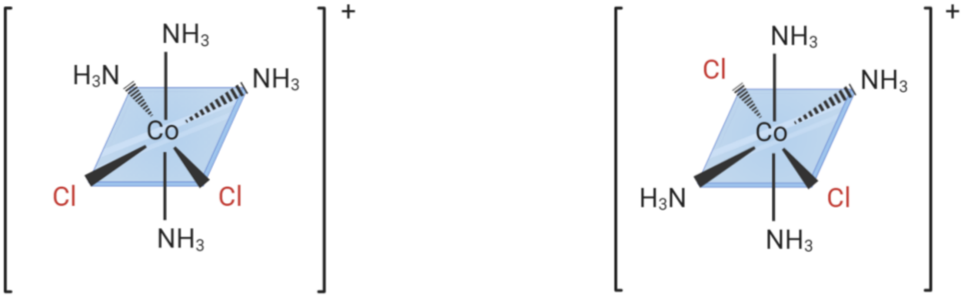

(a) **(b)**

Figure 1. 1 – Two $[Co(NH_3)_4Cl_2]^+$ cations with different properties due to different arrangements of the same ligands. The **a)** *cis*−$[Co(NH_3)_4Cl_2]$ complex unit presents a red color, whereas the **b)** *trans*−$[Co(NH_3)_4Cl_2]$ complex unit has a green color. *Picture created with BioRender.com*. Adapted from ref. [13]

Taking into account the coordination number, it is possible to predict the geometry of the MC (see Table 1. 1).

Table 1. 1 – Schematic geometrical structures of the metal complexes according to their coordination number.

Coordination number			
2	**3**	**4**	
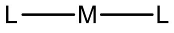	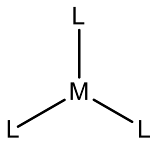	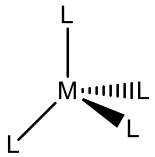	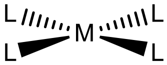
Linear	Trigonal planar	Tetrahedral	Square planar
5		**6**	
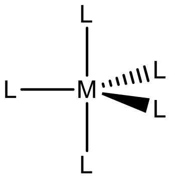	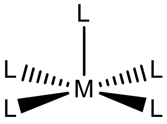	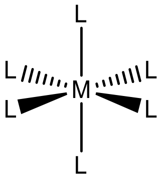	
Trigonal bipyramidal	Square pyramidal	Octahedral	

1.1.2. Ligands

Ligands play a central role in a MC by sharing their lone pair(s) of electrons with the metal ion. According to the number of electrons that are being shared, ligands can have different designations: *monodentate* if one lone pair of electrons is forming the coordinate bond or *polydentate* (bidentate, tridentate, etc.) if the ligands are sharing more than one pair to establish multiple bonds. Moreover, these polydentate ligands are able to bind to one central metal ion and form a ring (chelate), or to two or more metal ions and play as a bridge. In general terms, ligands (from organic or inorganic nature), can be simple ions (*e.g*. SCN^- or N_3^- ions), small molecules (*e.g. L*−arginine) or even macromolecules (*e.g*. proteins).[17]

L-arginine as an organic ligand

L−arginine (*L*−arg) is considered to be a semiessential amino acid, *i.e.* the human body can produce it in sufficient amounts through other precursors, but sometimes supplementation is needed.[18] This amino acid has in its chemical structure an important side chain guanidine base. In fact, guanidine's conjugated acid, the guanidinium cation, plays an important role in several biological processes.[19] Due to a high acid dissociation constant (pK_a) of 13.8, and such a remarkable stability (as a result of its electrons resonance, see Figure 1. 2), this group is able to form strong non-covalent interactions (ionic or hydrogen bonds) with anionic substrates. Moreover, it is typically involved in the inhibition of proteins aggregation and, specifically, interacts with the poly-anionic DNA.[20,21,22]

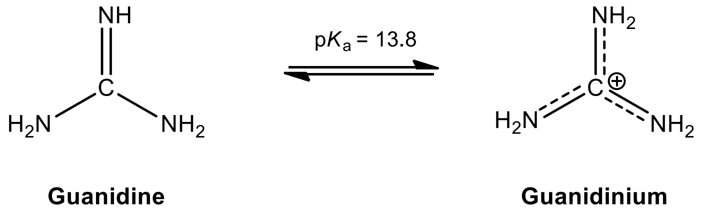

Figure 1. 2 – Structure of guanidine and its conjugated acid guanidinium. The dashed bonds represent the electrons resonance in guanidinium cation (so-called Y aromaticity).

The guanidinium group is also structurally important in metal complexes of copper(II) with *L*−arginine, in particular the ones with a $[Cu(L{-}arg)_2]^{2+}$ unit formula, since these type of complexes are considered to be structural analogs of Distamycin and Netropsin antibiotics (see Figure 1. 3).[23,24] As a matter of fact, the$[Cu(L{-}arg)_2](NO_3)_2$ coordination compound is a particular analogue of Netropsin and is known for binding the AT-DNA and, therefore, for regulating the process of replication and transcription.[23] The inhibition of these fundamental processes in microbes may be related with their growth[25] and thus *L*−arginine-based metal compounds are sometimes considered as potential antimicrobial agents.[23,25,26]

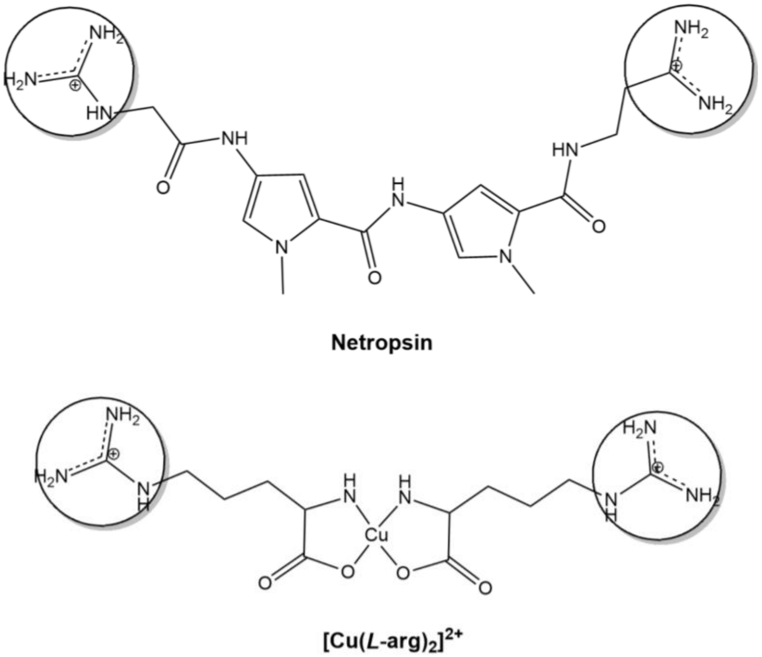

Figure 1. 3 – Comparison of Netropsin and a [Cu(*L*−Arg)$_2$]$^{2+}$ complex cation that behaves as a structural mimic of the antibiotic. The inset highlights the (guanidinium) end group similarities. *Picture created with ChemDraw*.

Despite of *L*−arginine net atomic charge values (Figure 1. 4), this amino acid typically coordinates with the central metal ion through nitrogen− and oxygen−electrons donor atoms from the amine and the carboxylate group, respectively.[21,23] In fact, the guanidinium group is not usually linked to metal ions.[21,22]

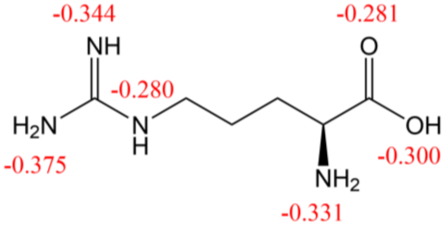

Figure 1. 4 – Net atomic charges of the neutral form of *L*−arginine (values taken from ref. [27]). *Picture created with ChemDraw.*

L−arginine is oxidized by an enzyme called nitric oxide synthase (NOS) and is the main source of nitric oxide (NO) production.[28] NO is a gaseous diatomic radical that plays essential roles (physiological responses) in different organisms, including bacteria and fungi.[29,30,31] In fact, NO is a potent antimicrobial compound[32] that is associated to membrane damage.[33] Its antimicrobial activity has been described by *Fang*[33]: i) during an infection, NO is efficiently produced by the host; ii) the withdrawal of NOS activity results in an increase of the microbial burden; iii) a variety of microbial targets have shown cytokine-inducible microbiostastic or microbicidal activity that is *L*−arginine-dependent; and iv) NO−donor compounds have the capacity to inhibit or kill microbes (when directly administered *in vitro*).

SCN$^-$ and N$_3$$^-$ ions as inorganic ligands

Potassium thiocyanate (KSCN) and sodium azide (NaN$_3$) do not possess any relevant biological activity. Chemically, SCN$^-$ and N$_3$$^-$ ions are structurally alike, since both are small triatomic molecules that present linear geometry and negative charge (that can either be localized in one of the terminal atoms or delocalized over the whole anion,[34] see resonance structures in Figure 1. 5).

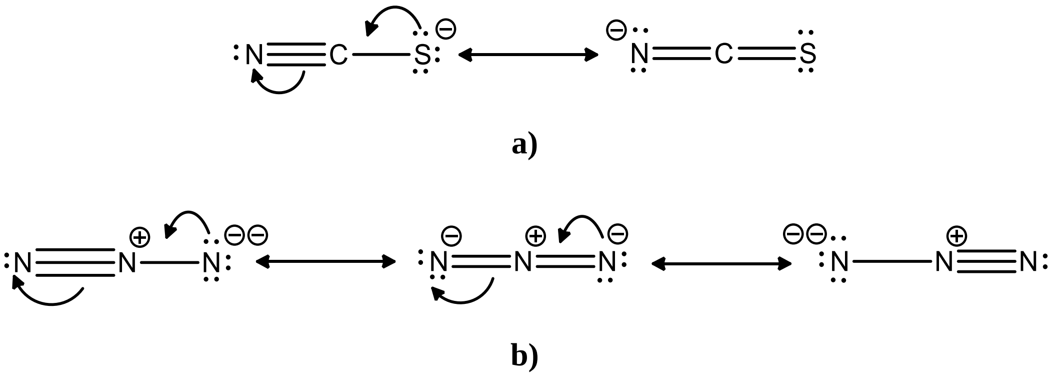

Figure 1. 5 – Resonance structures of **a)** SCN$^-$ and **b)** N$_3$$^-$ ions. *Picture created with ChemDraw.*

The thiocyanate and the azide ions play an important role in structural chemistry[34] for their ability of coordinating to the metal ion trough their corresponding electrons donor atoms, *i.e.* through the sulfur and nitrogen atoms[a] for the SCN$^-$ ion and through the nitrogen ones for the N$_3$$^-$ anion. Both species can either coordinated as a monodently or bidently (bridged) ligands.[35,36,37] Therefore, despite the lack of their biological activity, it may be a suitable strategy to employ these two anions in coordination chemistry since their metal−ligand complexes may have interesting and unique geometries (comparing to organic molecules) and thus form new bioactive metal-based drugs. As an example, two MC containing these two types of ligands and with enhanced biological activity (more precisely antimicrobial one) are shown in Table 1. 2.

---

[a] Note that when the SCN$^-$ ion coordinates through nitrogen atom, the –NCS chemical group it is called isothiocyanate.

Table 1. 2 – Examples of two biologically active metal complexes, containing either SCN^- or N_3^- ligands.

MC	Crystal structure	Observation	Ref.
MC of zinc(II) with thiocyanate	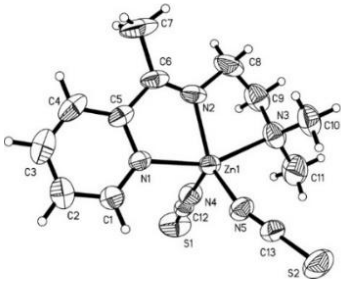	The complex shows greater antibacterial and antifungal activities against *Staphylococcus aureus*, *Escherichia coli and Candida albicans* species when compared to the free ligand.	38
MC of cadmium(II) with azide	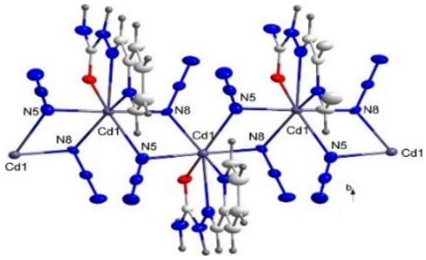	The complex has strong antimicrobial activity against *Bacillus subtilis*, *Staphylococcus aureus*, *Echerichia coli*, *Erwinia carotovora*, *Candida kefyr*, *Candida krusei and Aspergillus niger* species.	39

1.1.3. Crystal Field Theory

As mentioned before, a transition-metal complex has a central metal ion belonging to the *d*-block of the periodic table. Thus, its valence electrons are distributed along *d*-type orbitals. There are five types of these orbitals, d_{z^2}, $d_{x^2-y^2}$, d_{xy}, d_{xz} and d_{yz} (see Figure 1. 6), which are degenerated (have the same energy) in an isolated metal ion. However, upon complexation, the energy of the *d*-orbitals becomes non-degenerated.

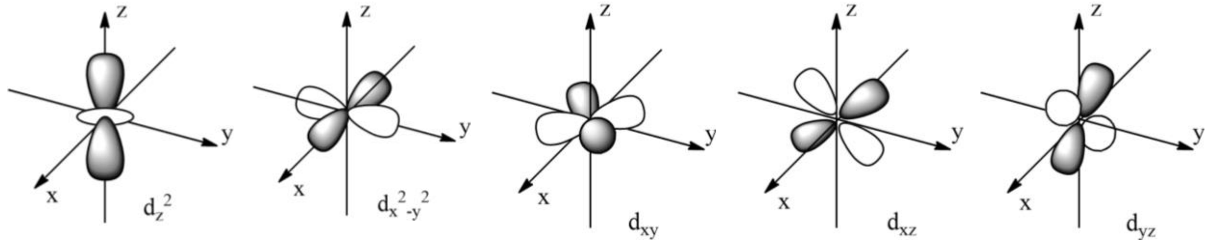

Figure 1. 6 – Schematic representation of the five types of *d*-orbitals. The d_{z^2} orbital has maximum amplitude along the z axis, whereas $d_{x^2-y^2}$ has maximum amplitude along the x and y axes. On the other hand, the d_{xy}, d_{xz} and d_{yz} orbitals have maximum amplitude at 45° of x and y axes, x and z axes and y and z axes, respectively. *Picture created with ChemDraw.*

According to crystal field theory (CFT), ligands are considered to be negative point charges. Hence, there is electrostatic repulsion between the ligands and the electrons of the *d*-orbitals, leading to an energy splitting (also called crystal field energy splitting, Δ_{CFES}).[40] In an octahedral field, the ligands are placed on-axis (higher repulsion) and so the destabilization of the d_{z^2} and $d_{x^2-y^2}$ orbitals is more pronounced comparing to the orbitals in between the axis (d_{xy}, d_{xz}, d_{yz}), that will have lower energy and be less affected by the repulsive character of the ligands (more stabilized, see Figure 1. 7a). Specifically, the d_{z^2} and $d_{x^2-y^2}$ orbitals are going to be destabilized by $+\frac{3}{5}\Delta_o$ (the "o" subscript on the Δ indicates that the complex has octahedral geometry), while the d_{xy}, d_{xz} and d_{yz} orbitals are going to be stabilized by $-\frac{2}{5}\Delta_o$. In a complex with tetrahedral geometry, the opposite splitting situation occurs, *i.e.* the ligands are off-axis and so the destabilization is going to be more pronounced in the d_{xy}, d_{xz} and d_{yz} orbitals. Indeed, the d_{xy}, d_{xz} and d_{yz} orbitals become destabilized by $+\frac{2}{5}\Delta_r$, while the d_{z^2} and $d_{x^2-y^2}$ orbitals become stabilized by $-\frac{3}{5}\Delta_r$ (the "r" subscript on the Δ indicates that the complex has tetrahedral geometry, see Figure 1. 7b). Different ligands will cause different energy splits of the *d*-orbitals (Δ_o, Δ_r, etc.). Moreover, in a MC with tetrahedral geometry, the ligands are not pointing directly to the *d*–orbitals, which results in an absolute smaller energy splitting when compared to the octahedral geometry ($\Delta_r < \Delta_o$).

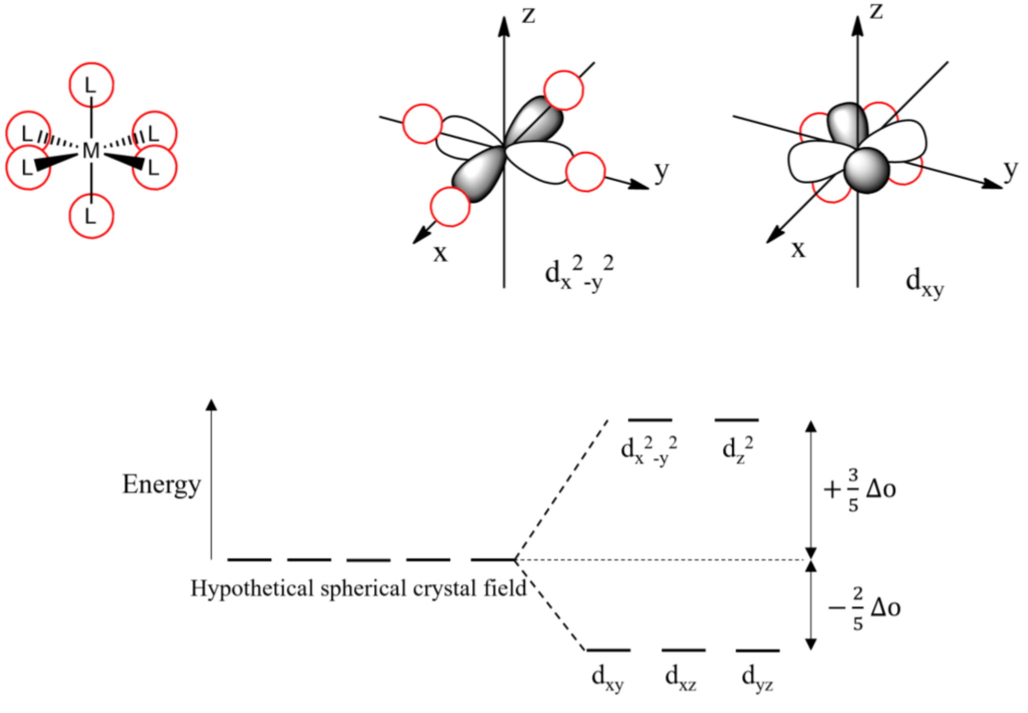

a)

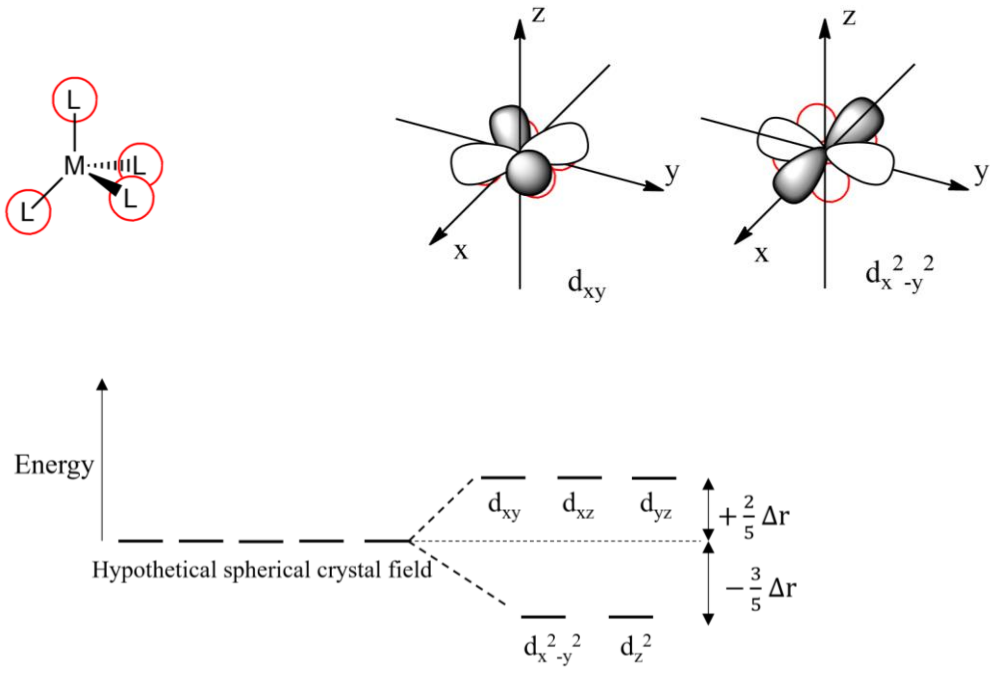

b)

Δ_o – octahedral crystal field splitting energy; Δ_r – tetrahedral crystal field splitting energy

Figure 1. 7 – Schematic representation of the *d*-orbitals energy splitting in an **a)** octahedral field and **b)** tetrahedral field. Two types of *d*-orbitals ($d_{x^2-y^2}$ and d_{xy}) are illustrated to showcase the repulsion between the electrons of the orbitals and the incoming ligands. The energy splitting is represented in relative terms (Δ_o and Δ_r), where “o” and “r” correspond to octahedral and tetrahedral fields, respectively. *Picture created with ChemDraw.* Adapted from ref.[41]

The Δ_{CFES} depends on the nature of the ligands and has consequences on the electronic configuration of the coordination compounds. For instance, if a ligand is considered to be highly repulsive, then a pronounced crystal field splitting is expected and the electrons will be firstly filled in the lower energy orbitals (pairing with each other, low spin). Conversely, in the presence of a slightly repulsive ligand, a small Δ_{CFES} is expected and the electrons will be distributed in both energy levels (following Hund’s rule, high spin). This non-degeneracy of the *d*-orbitals, leading to a low or high spin MC, results in the fascinating different colors and magnetic properties.[42]

Color and magnetic properties of the coordination compounds

When atoms or molecules absorb light at the proper frequency, their electrons are going to be excited to higher energy levels. In a MC, that energy of absorbed light is going to be equal to the CF energy splitting (Eq.1. 1). In other words, a MC will only absorb a photon of light if the energy of that photon is equal to the CF splitting difference.

$$E_{light} = hv = \Delta_{CFES} \qquad \text{Eq.1. 1}$$

where h stands for Planck's constant and ν for frequency.

The color of coordination compounds is essentially related with the oxidation state of the metal ion, the nature of the ligand(s) that are bounded to the central metal ion and with the geometry of the MC.[43] In general, a small Δ_{CFES} value indicates that low frequency photons are absorbed, *i.e.* in the range of yellow to red in the electromagnetic spectrum (560−860 nm). Therefore, the transmitted light is going to be between violet and green (400−560 nm). The relationship between the Δ_{CFES} and the absorbed photon's wavelength is described in Eq.1. 2:

$$c = \lambda v \gg \Delta = h\frac{c}{\lambda} \qquad \text{Eq.1. 2}$$

where λ is the wavelength and *c* the speed of light.

The magnetic properties of the coordination compounds are due to an orbiting electron motion around the nucleus or due to the intrinsic spin of the electron, a quantum property whose close classic analogue is a spinning electron that spins around its own axis.[44] So, according to the number of unpaired electrons, a MC can be considered either as diamagnetic or paramagnetic. The diamagnetic species are correlated with zero unpaired electrons and are weakly repelled by the magnetic field. Conversely, the paramagnetic species are associated with one or more unpaired electrons, providing these substances a magnetic moment in a magnetic field. For the paramagnetic species, it is possible to calculate their effective magnetic moment through the spin-only formula (Eq.1. 3):

$$\mu_{eff} = g\sqrt{S(S+1)} \qquad \text{Eq.1. 3}$$

where *g* is the Landé factor (= 2.0023) and *S* the spin angular momentum quantum number.

In addition to the common paramagnetic behavior, exchange interaction between the magnetic ions can result in ferromagnetic, antiferromagnetic or ferrimagnetic behavior, according to their spin coupling. If the magnetic moments of the unpaired electrons of the magnetic ions tend to align in the same direction, a ferromagnetic coupling is in order (and the substance is strongly attracted by the magnetic field). If the magnetic moments of neighbor ions have their spins pointing in opposite directions, then an antiferromagnetic order occurs. Finally, if the magnetic moments of the ion are also coupled in opposite directions, but not totally compensating each other, *i.e.* there are pointing more in one direction than the other, then a ferrimagnetic coupling is going to be witnessed. In many cases, the exchange interaction between magnetic ions is weak and no long-range order of the magnetic ions occurs at finite temperature, but antiferromagnetic or ferromagnetic short-range correlations are observed at low temperature.

It is important to notice that the magnetic susceptibility of paramagnetic compounds is strongly temperature-dependent. In fact, the magnetic susceptibility is inversely proportional to the temperature, which means that the magnetic properties of paramagnetic materials are stronger at low temperatures. Ferromagnetic and antiferromagnetic materials become paramagnetic at temperatures above the ordering temperature of the magnetic ions.[44] In Figure 1. 8, there is a schematic illustration of these temperature-dependence magnetic behaviors and two temperatures are highlighted: the Curie and the Neel ones. These temperatures correspond to the values above in which a paramagnetic behavior is observed for ferro/ferrimagnetic and antiferromagnetic materials, respectively.

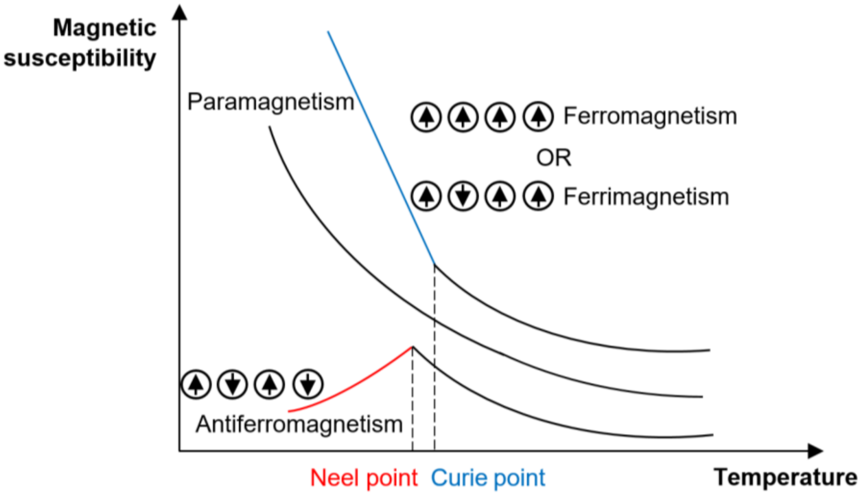

Figure 1. 8 – Representation of the typical magnetic susceptibility of paramagnetic substances with the variation of temperature. *Picture created with BioRender.com*. Adapted from ref. [45]

1.1.4. Applications of coordination compounds in the bioinorganic chemistry field

The bioinorganic chemistry field connects (inorganic) chemistry with physics, biology and medicine by studying coordination compounds of bioactive ligands.[29] In a diverse, sensitive and dynamic biological system, a variety of metal ions is found.[2] As a matter of fact, divalent metals are essential for the wellbeing of the eukaryotes (humans, other animals, plants and fungi) and prokaryotes (bacteria). Due to their involvement in several biological processes, their absence can be the key to an infection development.[46] On the other hand, if metal ions are present in high levels, some can be very toxic to the cells.[47,48] For example, low levels of calcium ions can result in a deficit cell regulation[49] and an absent of magnesium leads to the growth inhibition of certain fungi[50] or to a destabilization of membranes and ribosomes in bacteria.[51] A shortfall of zinc ions can lead to a slow growth of cells (having as consequence skin changes), but conversely, its excess can be toxic.[52] Similarly, an excess of copper can lead to a toxic effect because under aerobic conditions, copper is proposed to catalyze the production of reactive oxygen species (ROS), such as hydroxyl radicals.[53,54] Thereby, an ideal concentration of metal ions should be maintained in order to avoid opportunistic diseases.

When preparing metal-based compounds, it is important to consider not only a proper metal ion (Ca(II), Mg(II), Cu(II) and Zn(II) ions are biocompatible with the living organisms), but also a proper ligand (that has its own biological functionality). In fact, when an appropriate ligand is bonded to a metal atom, it can enhance the overall complex biological activities (*e.g.* antifungal, antibacterial or anticancer)[55,56,57,58,59] For instance, *Iqbal* and co-workers concluded that the free *L*−arginine does not possess antibacterial activity against *Escherichia coli, Staphylococcus aureus* and *Streptococcus pyogenes* bacteria.[60] However, upon coordination with copper(II) acetate salt, the resultant [Cu−*L*−arg] metal complex showed activity against all the tested strains, suggesting that *L*−arginine is an important agent that can improve the antimicrobial susceptibility of drugs.[25] In Table 1. 3 there are some examples of others *L*−arginine-based coordination compounds with enhanced biological activities.

Table 1. 3 – Examples of transition-metal complexes, containing *L*−arginine ligands, with enhanced biological activities.

MC	Crystal structure	Observations	Ref.
MC of copper(II) with *L*−arginine	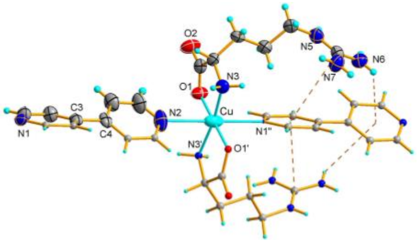 O2 O1' N3 N5 N6 N7 C3 N1 C4 N2 Cu N1'' N3' O1'	The complex presents strong activity against *Candida albicans* and against *Saccharomyces cerevisiae*; also shows activity against bacteria.	25
MC of silver(I) with *L*−arginine	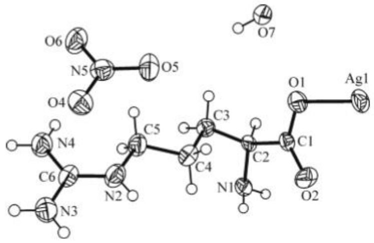 O6 O7 N5 O5 O4 O1 Ag1 N4 C5 C3 C1 C6 C4 C2 N2 N1 O2 N3	The complex shows good activity against Gram-negative bacteria and moderate activity against molds.	61

(to be continued)

MC of copper(II) and rhenium(VII) with *L*−arginine	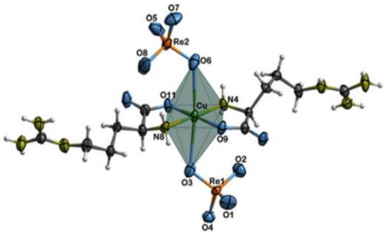	The complex exhibits potent *in vitro* antioxidant activity in dose-dependently.	62
MC of copper(II) with *L*−arginine	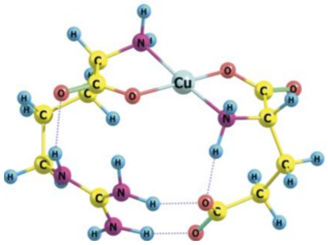	The complex induces a good inhibition of HePG2 (human cell lines hepatocellular carcinoma).	63
MC of silver(I) with *L*−arginine	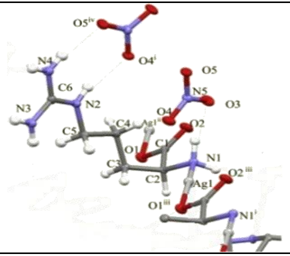	The complex inhibited the growth of four bacteria strains (*Escherichia coli*, *Pseudomonas aeruginosa*, *Bacillus subtilis and Staphylococcus aureus*) and one yeast (*Saccharomyces cerevisiae*).	64

Finally, it has been demonstrated that the *L*−arginine ligand is able to coordinate with other metal ions, namely Li^+, Na^+, K^+, Mg^{2+}, Ca^{2+}, Co^{2+}, Ni^{2+} or Zn^{2+}.[18,65,66,67] These metal ions are considered to be pharmacologically interesting since they are essential to maintain a healthy and vital human body.[68,69] Therefore, the synthesis of coordination compounds with *L*−arginine may be a suitable strategy to develop novel therapeutic agents for bacterial or fungal infections.[70]

Antimicrobial activity of the coordination compounds

Both bacteria and fungi can be considered as commensal species, *i.e.* if the host they are living in is healthy, then a symbiosis relationship can be sustained. However, if this synergetic and mutualistic association is disturbed (by a weak immune system of the host), some diseases may arise.[71,72]

Bacteria are prokaryotes cells that can exist in various shapes, being the most common ones the rod-like shape (*bacilli*), spherical or ovoid (*cocci*) and spiral-shaped. The bacteria cell envelope can be described as a complex of membranes (basically the cytoplasmic membrane and the cell wall), that are essential in the protection of the cytoplasm, in the control of permeability (barrier-selective) or in cell division.[73] According to the structure and composition of the cell envelope, bacteria can be considered either as Gram-positive or Gram-negative bacteria.[73,74] In Figure 1. 9 there is a schematic representation of these two types of bacteria.

Gram-negative bacteria have in its envelope: i) the outer membrane, which corresponds to a lipid bilayer composed essentially of lipopolysaccharide (LPS), capsular liposaccharides and porins; ii) the peptidoglycan cell wall, that is a rigid polymer that determines the cell shape; iii) the periplasm, that is an aqueous cellular compartment that delimits both outer and inner membranes; and finally iv) the inner cell membrane, a phospholipid bilayer with membrane proteins that delimits and protects the cytoplasmic organelles that are involved in essential cellular processes (such as proteins production).[74] Gram-positive bacteria, on the other hand, are essentially constituted by: i) many layers of peptidoglycan (the outer membrane is absent), ii) the periplasmic space and iii) the inner cell membrane. Threading through these layers of peptidoglycan are long anionic polymers, called teichoic acids, which are involved in the maintenance of the cell wall structure, and surface proteins, involved in the processes of recognition and adhesion.[73,74]

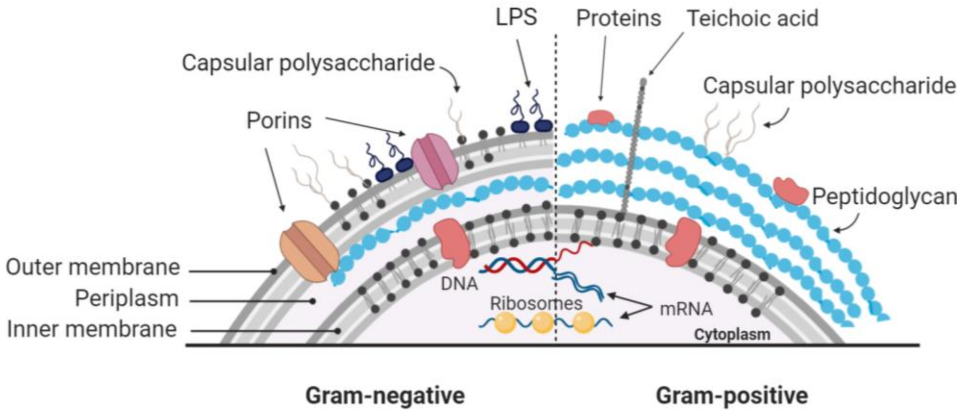

Figure 1. 9 – Structural differences of Gram-negative and Gram-positive bacteria. The former ones have a more complex cell wall structure with an outer and inner membrane and a periplasmic space, while the latter have only a peptidoglycan cell wall and a plasma membrane. *Picture created with BioRender.com.* Adapted from ref. [74]

Fungi are eukaryotic organisms that can exist as yeast (round and small cells), molds (filamentous strands) or a combination of both (dimorphic fungi).[75,76] Their complex cell structure is formed by a lipid bilayer with proteins and sterol embedded within it. The ergosterol (formed from lanosterol) provides a fluid, flexible and stable cell membrane, whereas the glucan synthase (enzyme) is responsible for the synthesis of the β-glucan polysaccharides that, in turn, helps in the formation of the rigid cell wall (protecting the cell membrane, see Figure 1. 10).[77,78]

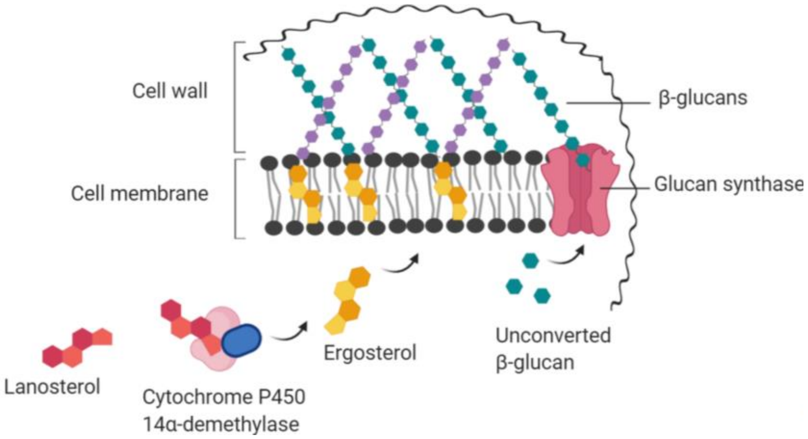

Figure 1. 10 –Schematic representation of the formation of the fungi cell wall and cell membrane. The cell wall is constituted mainly by different polysaccharides (β−glucans), whereas the cell membrane is constituted essentially by lipids. The 14α−demethylase is a cytochrome P450-dependent enzyme that allows the transformation of lanosterol to ergosterol. *Picture created with BioRender.com.* Adapted from ref. [79]

When preparing a potential drug capable of destroying these microbes, it is necessary to consider possible blocking targets. Generally, the main targets for bacteria are i) the inhibition of cell wall synthesis and ii) the inhibition of protein synthesis (directly or indirectly from DNA).[80,81] For fungi, it is possible to consider i) the inhibition of the synthesis of ergosterol and ii) the inhibition of the production of β-glucan.[82,83] One class of drugs used to treat bacterial infections are the lactams, whose final aim is to inhibit the synthesis of the bacterial cell wall (an important step to avoid the bacteria growth)[84]. For fungi, one of the few available drugs are the azoles, which work by inhibiting the production of β-glucan. Specifically, they bind the active site of cytochrome P450 14α−demethylase and inhibit the conversion of lanosterol to ergosterol, not allowing the fungal cell membrane formation.[85] However, due to an excessive use of the limited available medicines, some resistant strains (namely *Staphylococcus aureus* or *Candida tropicalis*) started to develop resistance mechanisms such as overexpression of efflux pumps proteins or formation of biolfilms,[82,86] resulting in treatment failure.[87]

It is known that complexation of a potential ligand with different metal ions can exhibit improved biological activity. In fact, two selected cases of coordination compounds with improved antibacterial and antifungal activity are discussed below. *Anacona* and co-workers synthetized novel manganese(II), cobalt(II), nickel(II), copper(II) and zinc(II) complexes of amoxicillin (an antibiotic that belongs to the lactams class) with promising bactericidal activity against *Escherichia coli, Staphylococcus aureus* and *Klebsiella pneumoniae* species.[88] On the other hand, *Castillo* and co-workers synthetized some copper(II), cobalt(II) and zinc(II) complexes using derivatives of the azoles as ligands.[85] All of the metal complexes showed good antifungal activity against the tested fungal strains. Additionally, the copper(II) coordination compound showed the highest antifungal effect by inhibiting the growth of all tested *Candida* and *Aspergillus fumigatus* species.

The enhanced biological activity can be explained on the basis of Overton's concept[89] and the chelation theory.[90] According to Overton's concept, the membrane that surrounds both bacteria and fungi species is selective and thus favors the passage of lipid-soluble components. Upon chelation, and stating chelation's theory, the polarity of the metal ion is reduced due to the overlap of the ligand orbitals and partial sharing of the positive charge of the metal ion with donor groups. Chelation may also increase the π−electrons delocalization on the chelate ring and, therefore, enhance the lipophilicity of the coordination compound (resulting on its better penetration into the lipid membrane of the microbe).[56,91,92,93] Consequently, the respiration process of the cell as well as the synthesis of proteins can be disturbed by the metal complex, causing the growth inhibition of the organism.[57,89,91,94]

1.2. Objectives

Two of the greatest goals in medicinal chemistry are to synthetize new drugs or to increase the quality/potency of the ones that are commercially available, while limiting side-effects.[95] For this reason, it is important to choose proper ligands when preparing metal-based drugs. To address such goals, it is fundamental to consider their electronic configuration (*i.e.* if they have electron donor and/or acceptor groups), their lipophilic/hydrophilic character (*e.g.* if they are too polar, they would not easily cross the cellular membrane), etc.[96]

L−arginine is an interesting and relevant amino acid in biology (since its guanidinium group is involved in several biological processes[19]), so to use it as a ligand can be a promising approach when synthetizing new coordination compounds. Normally, this group does not establish coordinate bonds with the central metal ion. In fact, due to its high pK_a value, the guanidinium group is found to be in its protonated (cationic) form in either aqueous solution or hydrophobic environment.[20,97] In addition, it can interact with the polyanionic components of the cell wall of microbes, due to a combined hydrogen-bonding and electrostatic forces, allowing the MC to penetrate the lipidic membrane wall of the organisms.[98]

The choice of the metal ion is also important, so in the present work, two first-row metal ions were chosen [zinc(II) and copper(II)], as well as two group 2 elements [magnesium(II) and calcium(II)]. All of these metals are present in bacteria and fungi in proper amounts to ensure these microbes homeostasis. A deficit or excess of these metal levels can lead to a perturbation of their equilibrium, affecting their growth.

Coordination compounds are found to have improved biological activities, such as antimicrobial or anticancer ones.[55,56,57,58,59] This enhanced biological activity may be explained by the light of Overton's concept[89] and the chelation theory.[90] This last concept states that complexation enhances the lipophilicity of the MC, leading to its better penetration through the lipid cell membrane of the microorganisms. Subsequently, the respiration and proteins synthesis processes of the fungi/bacteria can be disturbed, affecting the growth inhibition of these species.[57,89,91,94] Thereby, metal-based drugs may provide a better treatment of diseases caused by these microbes.[25,61,85]

Having this in mind, this piece of work has been devoted with the aim of synthetizing novel coordinated compounds of *L*–arginine, with potential antibacterial and antifungal activities. The physicochemical properties of the synthetized metal complexes were characterized by the means of X-ray crystallography and spectroscopic techniques. Magnetic studies were also carried out to understand and establish magneto-structural correlations. At a final stage, the antimicrobial activity of these metal complexes was evaluated against fungi, in particular against yeasts (*Candida albicans* and *C. tropicalis*) and dermatophyte strains (*Trichophyton mentagrophytes*, *Microsporum gypseum* and *Epidermophyton floccosum*), and bacteria, namely one Gram-negative bacterium (*Escherichia coli*) and Gram-positive bacteria (*Staphylococcus aureus*). Additionally, a benchmark between the MC structure and their biological activity against these species was derived.

Chapter 2.

Experimental section: Materials and methods

2. Experimental part: Materials and methods

2.1. Materials

The commercially available reagents: i) sodium azide (NaN_3, 65.009 g mol^{-1}), ii) *L*−arginine ($C_6H_{14}N_4O_2$,174.20 g mol^{-1}) and copper nitrate ($Cu(NO_3)_2{\bullet}2.5H_2O$, 232.59 g mol^{-1}) and iii) calcium chloride ($CaCl_2{\bullet}2H_2O$, 147.01 g mol^{-1}), calcium nitrate ($Ca(NO_3)_2{\bullet}4H_2O$, 236.15 g mol^{-1}), magnesium chloride ($MgCl_2{\bullet}6H_2O$, 203.30 g mol^{-1}), magnesium nitrate ($Mg(NO_3)_2{\bullet}6H_2O$, 256.41 g mol^{-1}), copper chloride ($CuCl_2{\bullet}2H_2O$, 170.48 g mol^{-1}), zinc chloride ($ZnCl_2$, 136.29 g mol^{-1}), zinc nitrate ($Zn(NO_3)_2{\bullet}6H_2O$, 297.48 g mol^{-1}) and potassium thiocyanate (KSCN, 97.181 g mol^{-1}) were acquired from Chempur, Sigma-Aldrich and PoCh, respectively, and used as received (without further purification).

The antimicrobial activity of the tested compounds was determined against: i) yeasts, ii) dermatophyte, iii) Gram-negative bacterium and iv) Gram-positive bacteria strains. For the yeasts, it was used one type strain from the American Type Culture Collection (ATCC) reference culture (*Candida albicans* ATCC 10231) and one clinical isolate strain (*Candida tropicalis* LF34), while for the dermatophyte, two clinical strains isolated from nails and skin (*Trichophyton mentagrophytes* FF7, *Epidermophyton floccosum* FF9), as well as one type strain from the Colección Española de Cultivos Tipo (*Microsporum gypseum* CECT 2908) were used. For the Gram-negative bacterium, one type strain from the American Type Culture Collection was used, namely *Escherichia coli* ATCC 25922. For Gram-positive bacteria, it was used two *Staphylococcus aureus* clinical isolates belonging to the collection of the Institute of Microbiology from Faculty of Medicine, University of Coimbra (FMUC). The fungal and bacterial isolates were identified by standard microbiological methods and stored on Sabouraud dextrose and Tryptic soy broths, respectively, with glycerol at −80°C. Prior to the susceptibility tests, and to ensure their optimal growth, fungi isolates were subcultured in Sabouraud dextrose agar (SDA) or potato dextrose agar (PDA), whereas the bacterial isolates were inoculated on Muller-Hinton Agar (MHA). These compounds were obtained from Oxoid. To the susceptibility and viability of the fungal assay, it was used a Roswell Park Memorial Institute medium (RPMI) 1640 broth from Biochrom in which the pH was necessary to adjust to 7 with a 5M-prepared NaOH solution. To the susceptibility and viability of the bacterial assay, it was used a Muller-Hinton broth medium.

2.2. Methods

2.2.1. Preparation of the solutions

Several 0.2 M solutions of calcium(II), magnesium(II), copper(II) and zinc(II) salts were prepared. To obtain an aqueous solution of $CaCl_2•2H_2O$, 7.353 g were dissolved in 250 mL of distilled water. The same procedure was repeated for $Ca(NO_3)_2•4H_2O$, $MgCl_2•6H_2O$ and $Mg(NO_3)_2•6H_2O$ salts, but by adding 11.802 g, 10.186 g and 12.820 g, respectively. The copper(II) and zinc(II) solutions were also prepared in an identical way but in a distilled water final volume of 200 mL (6.820 g of $CuCl_2•2H_2O$, 9.306 g of $Cu(NO_3)_2•2.5H_2O$, 5.459 g of $ZnCl_2$ and 5.945 g of $Zn(NO_3)_2•6H_2O$). The 0.2 M aqueous solutions of the ligands were prepared by respectively adding 17.420 g of *L*−arginine, 3.883 g of KSCN and 3.253 g of NaN_3 into 500 mL, 200 mL and 250 mL of distilled water.

2.2.2. General synthesis of the complexes

It was attempted the synthesis of different metal complexes with different ligands in the following systems: i) [Ca(II):*L*−arg], [Mg(II):*L*−arg], [Cu(II):*L*−arg] and [Zn(II):*L*−arg], ii) [Ca(II):*L*−arg:KSCN], [Mg(II):*L*−arg:KSCN], [Cu(II):*L*−arg:KSCN] and [Zn(II): *L*−arg:KSCN] and iii) [Ca(II):*L*−arg:NaN_3], [Mg(II):*L*−arg:NaN_3], [Cu(II):*L*−arg:NaN_3] and [Zn(II):*L*−arg:NaN_3]. The metal complexes of the [X:*L*−arg] (X = Ca(II), Mg(II), Cu(II) or Zn(II)) systems were prepared by slowly adding dropwise the aqueous solution of *L*−arginine (10 or 15 mL, 0.2 M) into the different aqueous solutions of Ca(II), Mg(II), Cu(II) and Zn(II) salts (5 mL, 0.2 M) under moderate stirring. It was prepared two different mixtures for each salt in order to have final molar ratios of 1:2 and 1:3. The coordination compounds of the [X:*L*−arg:KSCN] systems were firstly prepared like the procedure above. Then, to the prepared mixture, an aqueous solution of KSCN (10 or 15 mL, 0.2 M) was also added and stirred for 10/15 minutes. In this case, the mixtures were prepared in a molar ratio of 1:2:2, 1:2:3, 1:3:2 and 1:3:3 for each salt. Finally, the preparation of the [X:*L*−arg:NaN_3] systems followed the [X:*L*−arg:KSCN] systems synthesis procedure and stoichiometries, but adding the aqueous solution of NaN_3 (10 or 15 mL, 0.2 M) instead of the KSCN one.

All of the described mixtures were left to slowly evaporate for several days at room temperature. It was observed the formation of crystals, so the respective solutions were filtered. The crystals were washed with distilled water and kept at room temperature to slowly dry.

2.2.3. Single crystal and powder X-Ray diffraction

The single-crystal structures of the synthetized metal complexes were determined at 100 or 295 K in a KUMA KM-4 diffractometer, equipped with a two-dimensional area CCD detector and with a four-circle κ-geometry. Graphite monochromated MoK_α (λ=0.71073 Å) was used as the radiation source. Data collections, cell refinement, data reduction and analysis were carried out with CrysAlis CCD and CrysAlis PRO programs.[99] The structures were solved by direct methods using SHELXT and refined using the SHELXL-2018 program.[100]

Although single crystal X-ray crystallography is the most precise source of information to resolve and obtain detailed structural information of a metal complex[101], powder X-ray diffraction (PXRD) analysis of the synthetized products was also conducted to confirm its crystallinity, as well as to check if impurities were present. Additionally, the powder diffractograms of all the ligands were also collected and compared with the coordination compounds. For the procedure, the crystalline products were gently ground in an agate mortar (to obtain the powder) and cautiously deposited in the hollow of a zero-background sample holder made of silicon. The PXRD data were collected on a Bruker AXS D8 Advance diffractometer equipped with a silicon drift LYNXEYE detector ($\lambda_{CuK\alpha}$ = 1.5418 Å). The data were collected in Bragg-Brentano (reflection) geometry, at room temperature and in a range of $2\theta = 5-60^{o}$.

2.2.4. Infrared spectroscopy

Mid-infrared (in the range of 4000–400 cm^{-1}) spectra were collected at room temperature on a Vertex 70v FT-IR spectrophotometer, equipped with a diamond attenuated total reflection infrared cell, and set to an average of 64 scans with 4 cm^{-1} of resolution. Instrument control and initial data processing were performed using OPUS software (v. 7.0 Bruker Optics, Ettlingen, Germany).

2.2.5. Magnetic studies

The magnetic susceptibility and magnetization curves of the complexes were measured using a Vibrating Sample Magnetometer (VSM) installed in a Quantum Design PPMS-Dynacool instrument that is equipped with superconducting magnet (9 T). The powdered microcrystalline samples, with a mass average of 10 mg, were placed in a teflon sample holder. New sample holders were used for each sample to avoid contamination. Magnetic susceptibility curves were measured in the temperature range of 1.8−300 K and under an applied magnetic induction field, *B*, of 0.5 T. A magnetization isotherm at $T = 1.8$ K (full hysteresis cycle) was measured with applied magnetic induction field, varying between −9 and 9 T. A diamagnetic contribution, calculated from the chemical formula using Pascal constants, was subtracted from the experimental results.

2.2.6. Antimicrobial activity

Macrodilution broth method was followed to determine the minimal inhibitory concentrations (MICs) and minimal lethal concentrations (MLCs), according to Clinical and Laboratory Standards Institute (CLSI, formerly NCCLS) reference documents M27-A3, S3,[102] M38-A2[103] and M07-A9[104] for yeasts, filamentous fungi and bacteria, respectively. The fungal or bacterial suspensions were prepared in RPMI 1640 and Mueller Hinton broths, respectively. The density of the cellular suspensions was adjusted to the reference MacFarland scale of 0.5 units. Two-fold serial dilutions of all the tested products, ranging from 4−128 μg mL^{-1}, were prepared in sterilized RPMI/Mueller Hinton broths. For *Candida* strains, the test tubes were incubated aerobically at 37ºC for 48h, while for dermatophyte the incubation was performed at 30ºC for 7 days. For bacteria, the incubation period was 24 hours at 37ºC. The MICs were defined as the lowest product concentration that inhibited the growth of the microbe by 100%. After this incubation, the MLCs were evaluated by removing 20 µL from all the negative tubes (*i.e.* showing a total absence of growth) and pipetting it into SDA plates (fungi) or MHA plates (bacteria). The incubation process was the same as described before. The MLC was defined as the lowest product concentration deprived of visible growth on SDA or MHA plates. The sensitivity of the tested strains was controlled by the use of a reference antifungal compound (Fluconazole). Additionally, for each tested strain, the sterility and the growth conditions of the medium were checked in two control tubes. All experiments were performed in duplicate and repeated independently, at least, three times.

Chapter 3.

Results and discussion

Results and discussion

3.1. Synthesis of the complexes

For all the prepared calcium(II) mixtures, colorless small crystals were obtained after some days of solvent evaporation. For the mixtures of Ca(II) and *L*−arginine, a single product was obtained in the different synthesis conditions (suggested by the analysis of the infrared spectra). For the mixtures of Ca(II), *L*−arg and KSCN, the FT-IR spectra of the obtained crystals were identical to each other, suggesting that the products have the same chemical structure. Finally, for the mixtures of Ca(II) (specifically with the $Ca(NO_3)_2{\bullet}4H_2O$ salt), *L*−arg and NaN_3, two new products were obtained. Unfortunately, all the described products did not contain *L*−arg molecules in their structure, since the bands assigned as vibrational stretching of carboxylic acid and amino groups, characteristic of *L*−arg, were not observed in the FT-IR spectra. Therefore, all of these compounds were removed from the present study.

For the solutions with magnesium(II) salts, there was not crystal formation and these mixtures were also removed from this work.

In the case of the mixtures with copper(II) salts, eight different products were obtained and the more detailed characteristics of these synthesis are present in Table 3. 1. The obtained compounds from the 14a, 14b, 16c, 16d, 18a, 18b, 18c and 18d synthesis (Table 3. 1) showed, by comparison of the FT-IR spectra, the same chemical structure. This compound was named product 1 and its vibrational spectrum is represented in Figure S. 1. For the Cu(II):*L*−arg:KSCN system, product 1 and two new products, named product 2 (from synthesis 15a, 15b (second product), 15c, 15d, 16a and 16b) and product 3 (from synthesis 15b0), were obtained. The FT-IR spectra of these products are shown in Figures S. 2 and S. 3, respectively. For the Cu(II):*L*−arg:NaN_3 system, besides the formation of product 1 again, five different products (named products 4-8, from the remaining synthesis) were obtained and their vibrational spectra are depicted in Figures S. 4-S. 8, respectively.

The comparison of the FT-IR spectra allowed the following concluding remarks: i) the successful synthesis of product 1 (described in literature[22,105]) is independent on the reagents molar stoichiometry and on the presence of SCN^- or N_3^- ions, but sensitive to the use of different Cu(II) salts [$CuCl_2{\bullet}2H_2O$ *versus* $Cu(NO_3)_2{\bullet}2.5H_2O$]; ii) the synthesis of product 2 is not only independent on the reagents molar stoichiometry, but also on the use of different Cu(II) salts; iii) product 3 was only obtained by the synthetic method 15b0 (see Table 3. 1) and its chemical structure is described in literature[106,107]; iv) the synthesis of products 4-7 is dependent on the reagents molar stoichiometry and on the use of different Cu(II) salts; and v) product 8 is dependent on the use of different Cu(II) salts and very sensitive to the reagents molar stoichiometries. Indeed, by mixing $CuCl_2$ salt, *L*−arginine and NaN_3 in 1:1,8:2 or 1:2:3,2 ratios, it is possible to obtain this compound.

Table 3. 1 – Summary table of the synthesis of Cu(II) complexes.

System		**Ratio**	**Synth. No.**		**Observations**
13	$CuCl_2$:*L*−arg	1:2	13a		No crystals growth was observed.
		1:3	13b		No crystals growth was observed.
14	$Cu(NO_3)_2$:*L*−arg	1:2	14a		In the time range of 3-13 days, blue crystals were observed and the mixture was filtered.
		1:3	14b		In the time range of 3-13 days, blue crystals were observed and the mixture was filtered.
15	$CuCl_2$:*L*−arg:KSCN	1:2:2	15a		In the time range of 22-26 days, blue crystals were observed and the mixture was filtered.
		1:2:3	15b	15b0	After 3 days, green precipitation was observed and removed from the mixture.
				15b1	In the time range of 26-27 days, blue crystals were observed and the mixture was filtered.
		1:3:2	15c		In the time range of 22-28 days, blue crystals were observed and the mixture was filtered.
		1:3:3	15d		In the time range of 20-26 days, blue crystals were observed and the mixture was filtered.
16	$Cu(NO_3)_2$:*L*−arg:KSCN	1:2:2	16a		In the time range of 15-18 days, blue crystals were observed and the mixture was filtered.
		1:2:3	16b		After 15 days, blue crystals were observed and the mixture was filtered.
		1:3:2	16c		In the time range of 12-13 days, blue crystals were observed and the mixture was filtered.
		1:3:3	16d		After 18 days, blue crystals were observed and the mixture was filtered.
17	$CuCl_2$:*L*−arg:NaN_3	1:2:2	17a		After 26 days, blue crystals were observed and the mixture was filtered.
		1:2:3	17b		In the time range of 3-12 days, the mixture was deep green and it was filtered. After 15 days, green crystals were observed and the mixture was filtered.[a]
		1:3:2	17c		After 39 days, blue crystals were observed and the mixture was filtered.
		1:3:3	17d		After 34 days, blue crystals were observed and the mixture was filtered.
18	$Cu(NO_3)_2$:*L*−arg:NaN_3	1:2:2	18a		In the time range of 12-13 days, blue crystals were observed and the mixture was filtered.
		1:2:3	18b		After 15 days, blue crystals were observed and the mixture was filtered.
		1:3:2	18c		In the time range of 13-18 days, blue crystals were observed and the mixture was filtered.
		1:3:3	18d		In the time range of 22-28 days, blue crystals were observed and the mixture was filtered.

[a] In order to try to get the green crystals again, the synthesis was repeated several times and changes in the stoichiometry were made. New products (blue and green crystals) were obtained.

The overall isolated products, resultant from the systems Cu(II):*L*−arg and Cu(II):*L*−arg:X (X = SCN^-, N_3^-), are shown in Figure 3. 1.

(1)

$\{[Cu(L\text{-}arg)_2](NO_3)_2 \cdot 3H_2O\}_n$

(2)

$[Cu(L\text{-}arg)_2(SCN)_2] \cdot 2H_2O$

(3)

$[Cu(L\text{-}arg)(SCN)_2]$

(4)

$[Cu(L\text{-}arg)_2(N_3)_2][Cu(L\text{-}arg)_2Cl](N_3) \cdot 7H_2O$

(5)

$\{[Cu_2(L\text{-}arg)_2(N_3)_2(\mu\text{-}1,3\text{-}N_3)(\mu\text{-}1,1\text{-}N_3)][Cu(L\text{-}arg)(N_3)(\mu\text{-}1,1\text{-}N_3)] \cdot 3H_2O\}_n$

(6)

$[Cu(L\text{-}arg)_2(N_3)_2][Cu(L\text{-}arg)_2(N_3)](N_3) \cdot 6H_2O$

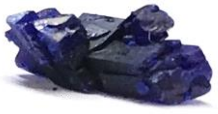

(7)

$[Cu(L\text{-}arg)_2(H_2O)_2](N_3)_2$

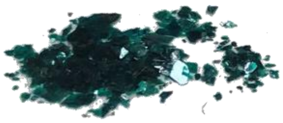

(8)

$\{[Cu(L\text{-}arg)(N_3)(\mu\text{-}1,3\text{-}N_3)]\}_n$

Figure 3. 1 – Single-crystals obtained from the different synthetized products (1-8).

Finally, for all the zinc(II) salts systems, a white precipitate in the form of $Zn(OH)_2$ was obtained. The initial pH of the samples was around 8, so HCl was added to the mixtures to adjust it to ~6. However, the $Zn(OH)_2$ dissociation into Zn(II) ions was not achieved and all the zinc(II) solutions were no longer considered in the present dissertation.

3.2. X-Ray diffraction analysis and structure determination

Product 1

The crystal structure of $[Cu(L{-}arg)_2](NO_3)_2{\bullet}3H_2O$ **(1)** is depicted in Figure 3. 2 and its crystallographic data presented in Table 3. 2. Additional crystallographic data and structure refinement can be found in the literature.[22,105]

The single-crystal X-ray diffraction analysis revealed that the unit cell of **(1)** consists of one *cis*−$[Cu(L{-}arg)_2]^{2+}$ cation, two NO_3^- anions (to balance the overall charge of the metal complex) and three lattice water molecules (see Figure 3. 2a). In the $[Cu(L{-}arg)_2]^{2+}$ complex unit, the copper(II) center is four-coordinated by two carboxylate oxygen atoms (O1 and O3) and two amino nitrogen atoms (N1 and N5), belonging to two distinct *L*−arg molecules. The $Cu{-}O_{L-arg}$ and $Cu{-}N_{L-arg}$ bond lengths are in the range of 1.93−1.98 Å (see Table 3. 3). The carboxylate group from one *L*−arg molecule links the Cu(II) ions in a one-dimensional (1D) infinite chain structure (polymeric nature, see Figure 3. 2b). The distances between the Cu(II) center and the O2 atom is 2.49 Å. This observed O−C−O bridge pattern was also described by *Şahin* and co-workers for a very similar metal complex. In their work, the polymeric nature of the metal complex was sustained by the carbonyl oxygen atom coordinated to a Na(I) ion, with a bond length of 2.62 Å.[108]

Product 1 was previously obtained and characterized by other researchers (see refs. [22] and [105]). However, different synthesis procedures were followed. For instances, *Hu* and co-workers used the copper(II) nitrate salt and *L*−arginine ligands in a molar ratio of 1:2, heated the mixture to 70ºC for 10h and then cooled it to room temperature. After several weeks of slow solvent evaporation, blue needle-like crystals were obtained.[22] *Masuda* and co-workers mixed the copper(II) nitrate salt with an acid solution of Arg-HCl (also in a 1:2 reagents molar stoichiometry), adjusted the mixture pH to 6.5 with a 1M NaOH solution and then collected the blue crystals of $[Cu(L{-}arg)_2](NO_3)_2{\bullet}3H_2O$.[105]

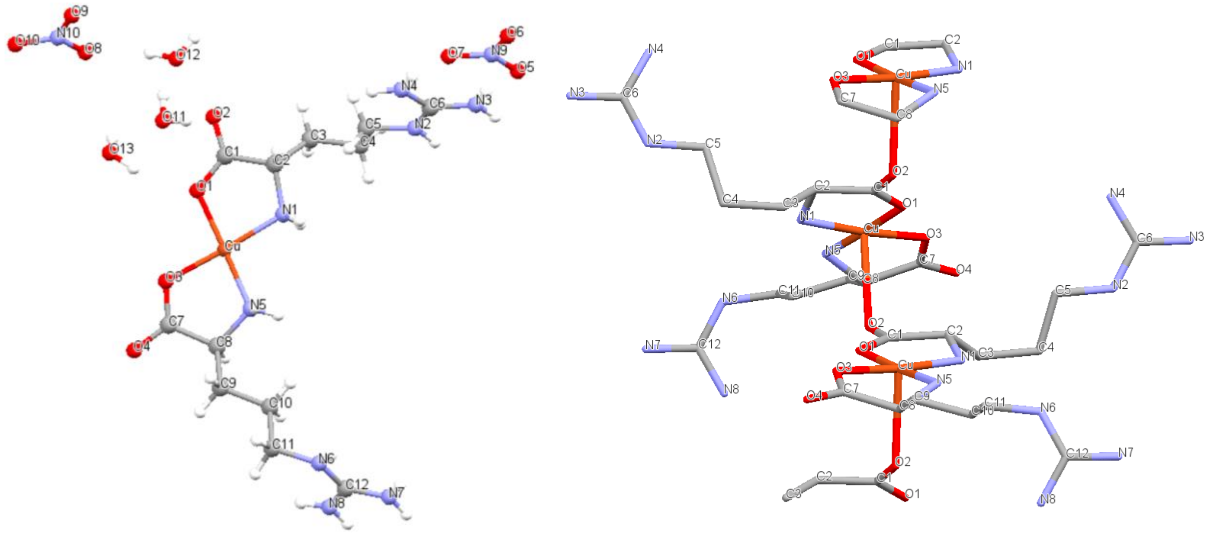

a)

b)

Figure 3. 2 – a) Unit cell of [Cu(*L*−arg)$_2$](NO$_3$)$_2$•3H$_2$O **(1)** single-crystals and **b)** 1D coordination polymer with atom numbering. The hydrogen atoms in **b)** were omitted for clarity.

Table 3. 2 – Crystallographic data and X-ray experimental details for **(1)**.

Chemical formula	$C_{12}H_{34}CuN_{10}O_{13}$
M$_r$	590.03
Crystal system, space group	Monoclinic, C2
Temperature (K)	295
***a*, *b*, *c* (Å)**	26.705(4), 7.3190(10), 12.788(2)
***β* (°)**	92.090(10)
***V* (Å^3)**	2497.8(6)
Z	4
Radiation type	MoK_α
***μ* (mm^{-1})**	0.954
Crystal size (mm)	0.1x0.2x0.2

Table 3. 3 – Selected geometric parameters (Å, deg) for **(1)**, obtained by the X-ray diffraction studies.

(1)			
Distances (Å)		**Angles (°)**	
		O1−Cu−O3	94.3(2)
Cu−O3	1.9324(16)	O1−Cu−N5	84.5(2)
Cu−O1	1.9531(18)	O1−Cu−N1	175.2(4)
Cu−N1	1.974(2)	O3−Cu−N5	177.1(3)
Cu−N5	1.980(2)	O3−Cu−N1	84.3(2)
Cu−O2#1	2.487(2)	N5−Cu−N1	96.7(2)

Symmetry transformations used to generate equivalent atoms for **(1)**: #1: $-x+1, y+\frac{1}{2}, -z+1$.

The powder diffractogram obtained for the crystal structure (found from the single-crystal X-ray analysis) is consistent with the predicted one for product 1, without traces of additional phases (see Figure 3. 3). Furthermore, the powder X-ray diffraction (PXRD) pattern of product 1 is completely different from those of the starting materials (ligands), evidencing the formation of the metal complex (Figure S. 9).

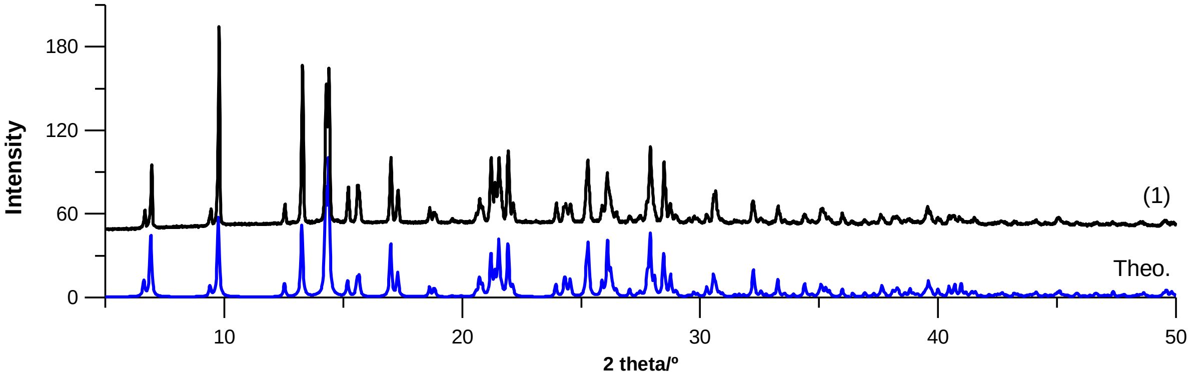

Figure 3. 3 – PXRD pattern obtained for **(1)** (black line). The blue line diffractogram (at the bottom) shows the predicted positions and relative intensity of peaks calculated from the crystal structure obtained from the single X-ray diffraction.

Products 2 and 3

The crystal structures of the [Cu(*L*−arg)$_2$(SCN)$_2$]•2H$_2$O **(2)** and [Cu(*L*−arg)(SCN)$_2$] **(3)** coordination compounds are shown in Figure 3. 4, while the crystal data are presented in Table 3. 4.

Product 2 crystallizes in a monoclinic crystal system, $P2_1$ space group. The unit cell accommodates one copper(II) ion, two *L*−arg molecules, two thiocyanate ions and two lattice water molecules (Figure 3. 4a). The copper(II) center is six-coordinated by *trans*−chelating oxygen (O1, O11) and nitrogen (N3, N13) atoms, from the two distinct *L*−arg molecules, and by two nitrogen (N1, N2) atoms, from two distinct isothiocyanates. The copper coordination sphere is a distorted octahedron where the O11, N13, O1 and N3 coordinated atoms form the basal plane. The N1 and N2 atoms are in the axial vertexes of the octahedron. Both Cu−N$_{L\text{-arg}}$ bond lengths (Cu−N3 and Cu−N13) equals 1.99 Å, while the two Cu−O$_{L\text{-arg}}$ (Cu−O1 and Cu−O11) distances are 1.94 and 1.96 Å, respectively, being typical Cu−O,N values found for copper(II):*L*−arginine coordination compounds.[22,109,110,111] The Cu−N$_{\text{NCS.}}$ bond lengths (Cu−N1 and Cu−N2) are 2.52 Å and 2.61 Å, respectively. The typical Cu−N$_{\text{NCS.}}$ bond length is around 2 Å,[112,113,114,115] thus the isothiocyanate groups are weakly coordinated to the metal center. As a matter of fact, these Cu−N$_{\text{NCS}}$ distances are longer than the Cu−O/N (O and N from *L*−arginine molecule, due to the

Jahn-Teller (J-T) effect[b], meaning that the octahedron is axially elongated. The two coordinated isothiocyanates adopt an almost linear geometry, both with N1−C1−S1 and N2−C2−S2 angles of 178.0° (see Table 3. 5). Since there is an elongation of the z axis, less repulsion is felt between the isothiocyanate electrons and the electrons of the orbitals placed in the z axis. Consequently, these orbitals are going to lower their energy and become more stabilized by the J-T effect. The reverse situation occurs for the (compressed) orbitals placed in the xy plane, that become destabilized by the J-T effect (higher energy, see Figure S. 10).

For **(3)**, the unit cell is composed by one Cu(II) ion, one *L*−arg molecule and two isothiocyanate groups, consisting of [Cu(*L*−arg)(SCN)$_2$] complex unit (Figure 3. 4b). This product crystallizes in orthorhombic crystal system, $P2_12_12_1$ space group. The Cu(II) ion is coordinated to one oxygen (O1) and one nitrogen (N3) atoms (from the *L*−arg molecule), in a bidentate chelating coordination mode, and to two different N−coordinated thiocyanate ligands (N1 and N2). The copper(II) coordination sphere is a slightly distorted square planar geometry around the Cu(II) ions, with bond angles around the metal center (N1−Cu−N2, N1−Cu−N3, N2−Cu−O1 and O1−Cu−N3) varying from 83.47° to 93.22° (see Table 3. 5). The bond distances Cu−O1, Cu−N3, Cu−N1 and Cu−N2 are 1.95 Å, 1.99 Å, 1.96 Å and 1.95Å, respectively, being comparable with literature data.[112,113,114,115]

Product 3 was previously synthetized and its crystal structure determined (see refs. [106] and [107]). However, in this present dissertation, a new synthesis is described for this compound. *Guang* and co-workers used copper nitrate salt, *L*−arginine and KSCN ligands in a molar ratio of 1:1:2 and the metal complex was obtained after one week of slow solvent evaporation (at room temperature).[106] *Wojciechowska* and co-workers, by using the same molar stoichiometry of 1:1:2 but with a different copper(II) salt (copper chloride instead) obtained this compound after 7 days of slow solvent evaporation (at room temperature).[107] In the present work, it was used $CuCl_2•2H_2O$, *L*−arginine and KSCN in a proportion of 1:2:3 and the product was obtained after only 3 days.

---

[b] Jahn-Teller (J-T) effect causes a geometrical distortion of non-linear molecules with unequal electrons occupancy in the degenerated orbitals.[153] This situation, observed in systems containing divalent copper atoms (d^9), is not stable. Therefore, a metal complex with such configuration (and with an octahedral geometry) will undergo a particularly strong J-T distortion to lower (and stabilize) the overall energy of the species.[154] Consequently, the first coordination sphere of the Cu(II) ion is going to be distorted. The most common observed situation is an elongated octahedron with two longer axial bonds and four shorter equatorial ones.[154]

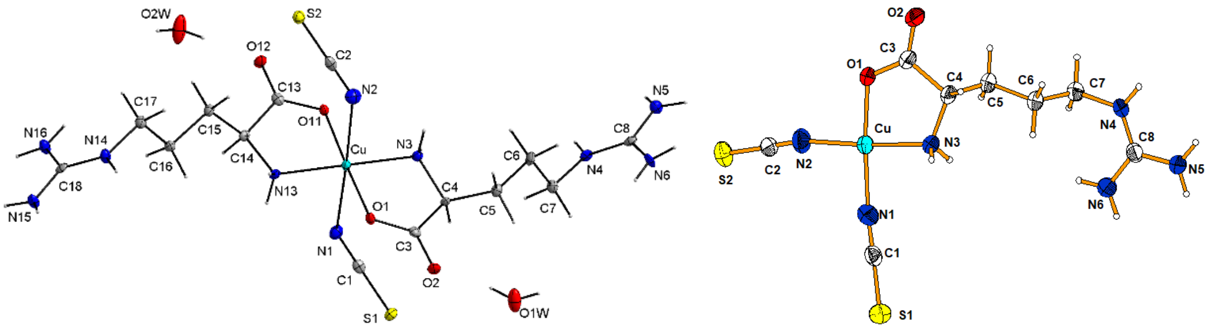
O2W
S2
O12
C2
C13
N2
C17
N16
N14
C15
O11
Cu
N3
C16
C14
C18
N13
C6
C4
C8
N5
N4
N6
N15
O1
C5
C7
N1
C3
C1
O2
S1
O1W
O2
C3
O1
C4
C6
C7
C5
Cu
N4
C8
S2
C2
N2
N3
N5
N6
N1
C1
S1

a) **b)**

Figure 3. 4 **–**Unit cell of **a)** [Cu(*L*−arg)$_2$(SCN)$_2$]•2H$_2$O **(2)** and of **b)** [Cu(*L*−arg)(SCN)$_2$] **(3)** single-crystals with atom numbering.

Table 3. 4 – Crystallographic data and X-ray experimental details for **(2)** and **(3)**.

	(2)	**(3)**
Chemical formula	$C_{14}H_{28}CuN_{10}O_4S_2.2H_2O$	$C_8H_{14}CuN_6O_2S_2$
M$_r$	564.17	353.91
Crystal system, space group	Monoclinic, *P*2$_1$	Orthorhombic, *P2$_1$2$_1$2$_1$*
Temperature (K)	100	295
a, b, c (Å)	8.3426(3), 7.9896(3), 18.1264(6)	6.0167(1), 12.1918(3), 18.4227(4)
***β* (º)**	92.733(3)	90
***V* (Å^3)**	1206.82(7)	1351.39(5)
Z	2	4
Radiation type	Mo*K$_α$*	Mo*K$_α$*
***μ* (mm^{-1})**	1.13	1.93
Crystal size (mm)	0.31x0.28x0.09	0.23x0.19x0.15

Table 3. 5 – Selected geometric parameters (Å, deg) for **(2)** and **(3)** obtained by the X-ray diffraction studies.

Distances (Å)			
(2)		**(3)**	
Cu−O1	1.955(3)		
Cu−N13	1.989(3)	Cu−O1	1.9509(18)
Cu−O11	1.938(3)	Cu−N3	1.9958(19)
Cu−N3	1.989(3)	Cu−N1	1.961(3)
Cu−N1	2.527	Cu−N2	1.945(2)
Cu−N2	2.605		
Angles (º)			
O1−Cu−N13	96.63(15)	N1−Cu−N2	93.22(11)
O1−Cu−O11	177.67(13)	N1−Cu−O1	172.55(9)
N13−Cu−O11	84.80(15)	N1−Cu−N3	90.42(10
N13−Cu−N3	179.05(19)	N2−Cu−O1	92.95(9)
O11−Cu−N3	94.88(14)	N2−Cu−N3	176.29(10)
N3−Cu−O1	83.73(15)	O1−Cu−N3	83.47(8)
N1−C1−S1	178.0(5)	N1−C1−S1	178.7(3)
N2−C2−S2	178.0(4)	N2−C2−S2	178.6(3)

The powder X-Ray diffractograms of **(2)** and **(3)** are depicted in Figure 3. 5. In both products, the PXRD patterns (experimentally obtained and simulated) are in a very good agreement between each other. In product 2, there are a few peaks in the experimental pattern that are not represented in the predicted one, possibly due to the presence of a small amount of a solvated product or due to the presence of some impurities. For **(3)**, there is a perfect match between the collected and the predicted PXRD patterns. We observe for this compound slightly higher scattered intensity below 7° (2θ) in the curved baseline of the experimental diffractogram, that may be indicative of the presence of a small amount of an amorphous product. The differences in relative intensity for some peaks may be related with texture effects of the pressed powder (preferred orientation). The obtained PXRD pattern for products 2 and 3 are different from the starting materials ($CaCl_2•2H_2O$, *L*−arginine and KSCN), indicating the formation of the metal complexes (Figure S. 10).

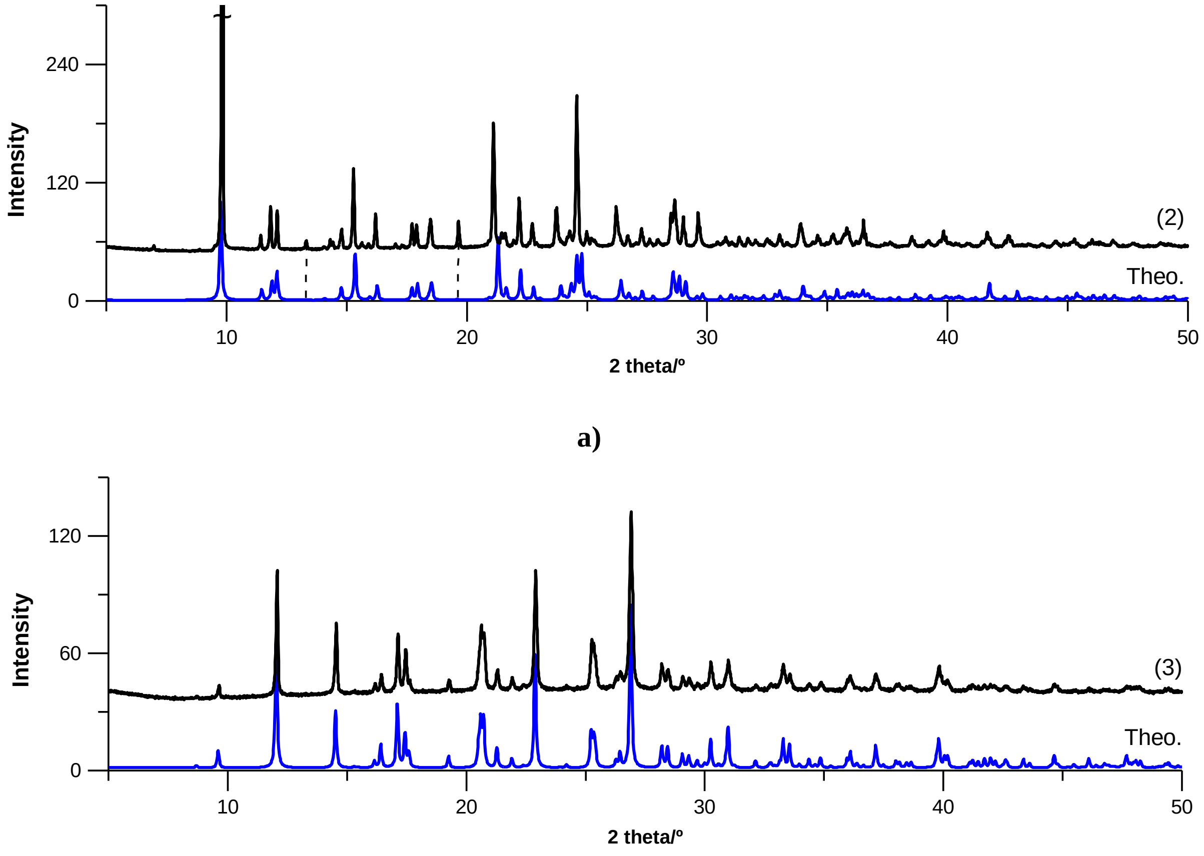

a)

b)

Figure 3. 5 – PXRD patterns obtained for **a) (2)** and for **b) (3)** (black line). The blue line diffractograms (at the bottom) show the predicted positions and relative intensity of peaks calculated from the crystal structure obtained from the single X-ray diffraction. In product 2, the intensity of the peak marked with a tilde (~) was truncated.

Products 4, 6 and 7

The crystal structures of the $[Cu(L{-}arg)_2(N_3)_2][Cu(L{-}arg)_2Cl](N_3)\bullet 7H_2O$ **(4)** and $[Cu(L{-}arg)_2(N_3)_2][Cu(L{-}arg)_2(N_3)](N_3)\bullet 6H_2O$ **(6)** metal complexes are shown in Figure 3. 6 and the crystallographic data presented in Table 3. 6.

Single-crystal X-ray analysis results show that **(4)** crystallizes in a monoclinic crystal system, with space group symmetry $P2_1$. The unit cell is composed of two metal complexes: i) a six−coordinated Cu(II) center with two *L*−arg molecules and two azide ions; and ii) a five−coordinated Cu(II) center with two *L*−arg molecules and one chlorine anion (Figure 3. 6a). Additionally, one N_3^- counterion, as well as seven lattice water molecules, are also included in the unit cell of the crystalline structure.

Product 6 crystallizes in a monoclinic crystal system with $P2_1$ space group. The unit cell also accommodates two metal complexes: i) a six−coordinated copper(II) ion with two *L*−arg molecules and two azide anions; and ii) a five−coordinated Cu(II) ion with two *L*−arg molecules and one azide anion (Figure 3. 6b). One N_3^- counterion and six lattice water molecules are also present in the unit cell.

Comparing these two products, it is possible to identify structural similarities. In the six−coordinated metal complexes of **(4)** and **(6)**, the *trans*−chelated donor atoms of the two *L*−arg molecules (O1, N1 and O11, N11 for both cases) form an octahedral environment with a CuN_2O_2 chromophore around the copper(II) ion. The distances found for $Cu{-}O_{L\text{-arg}}$ and $Cu{-}N_{L\text{-arg}}$ are in the range of 1.95 Å to 2.00 Å for each case, being in a good agreement with other $M{-}O/N_{L\text{-arg}}$ bond lenghts.[22,109,110,111] The apexes of the octahedron are occupied, in both six−coordinated compounds, by two distinct azides. However, slight changes can be found for the five-coordinated metal complexes. In **(4)**, the apex of the square pyramid is occupied by a chlorine Cl1 atom, whereas in **(6)** it is occupied by an azide ion (N3A−N3B−N3C). In product 4, the Cl1 atom acts as a Lewis base and donates a lone pair of electrons to form the dative Cu2−Cl1 bond. The Cl1 atom is distanced by 2.47 Å, a typical value found for others Cu−Cl bond lengths.[116,117] In product 6, the distance between Cu2 and N3A atom, as expected, is slightly shorter (2.35 Å, see Table 3. 7) than the Cu−Cl one. However, it is still a little bit longer comparing to others described in literature.[118,119] More, the square pyramidal (SP) geometry of **(4)** and **(6)**, evidenced by the angular parameter of the degree of trigonality (τ), is almost ideal since τ is close to zero (if it was close to one, the geometry would be similar to trigonal bipyramidal). The τ parameter is defined as:[120]

$$\tau = \frac{(\beta - \alpha)}{60} \qquad \text{Eq.3. 1}$$

where β and α correspond to the two greatest valence angles of the coordination center and β > α. For product 4, the β [O31−Cu2−O21] angle is 171.9°, while the α [N31−Cu2−N21] angle equals 169.6° (τ = 0.0383). For product 6, the β [O31−Cu2−O21] and α [N21−Cu2−N31] angles are 173.19° and 167.53°, respectively (τ = 0.0943).

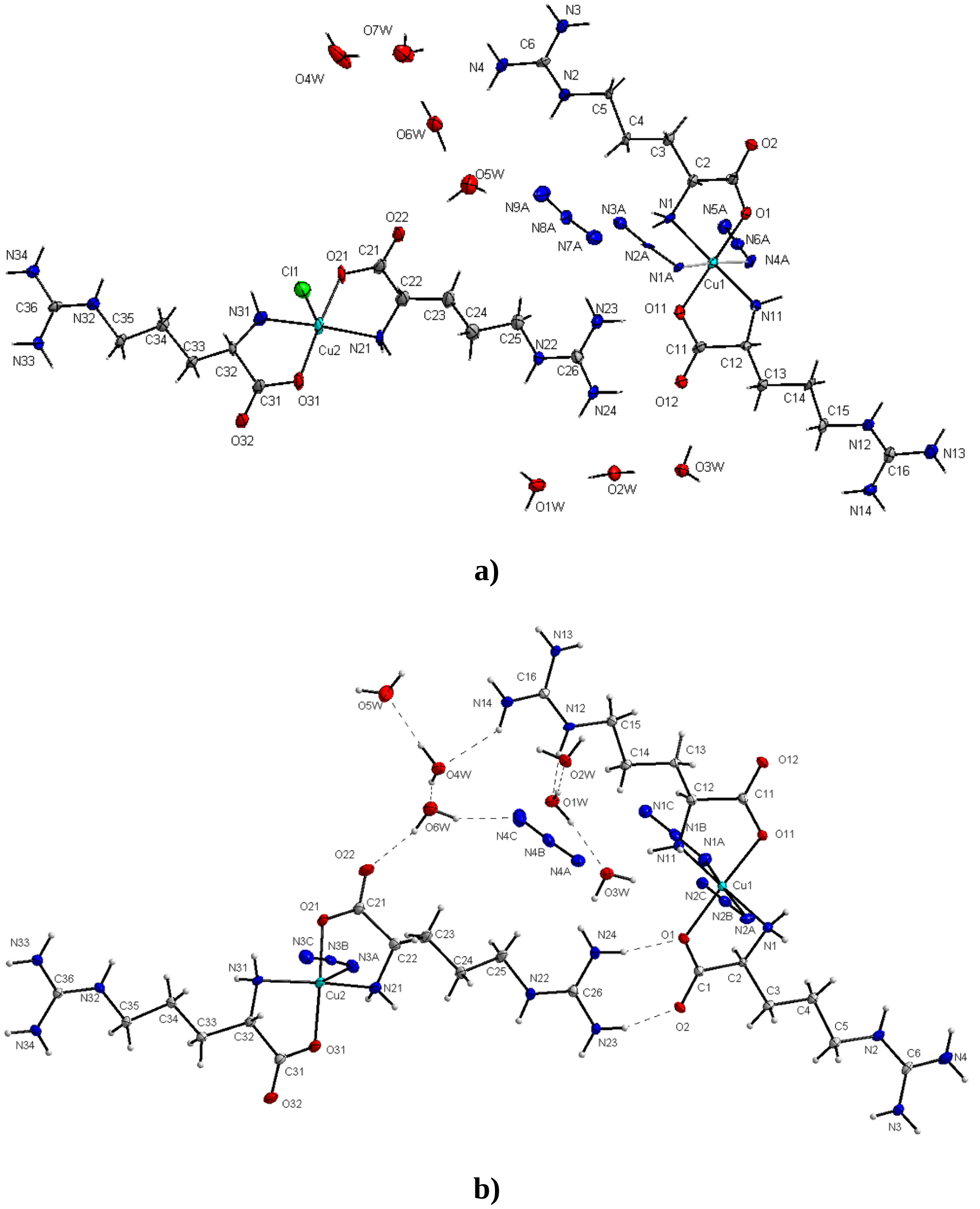

a)
O7W
O4W
O6W
O5W
N3
C6
N4
N2
C5
C4
C3
C2
O2
N1
O1
N5A
N6A
N4A
N9A
N8A
N7A
N3A
N2A
N1A
Cu1
O11
N11
C11
C12
C13
C14
C15
N12
C16
N13
N14
O12
O22
O21
C21
C22
C23
C24
C25
N22
N23
C26
N24
Cl1
N31
Cu2
N21
C32
C31
O31
O32
N34
C36
N32
C35
C34
C33
N33
O1W
O2W
O3W
b)
N13
C16
N14
N12
C15
C14
C13
C12
C11
O12
O11
O5W
O4W
O2W
O1W
O6W
O3W
N4C
N4B
N4A
N1C
N1B
N1A
N11
Cu1
N2C
N2B
N2A
N1
O22
O21
C21
C22
C23
C24
C25
N22
C26
N24
N23
O1
C1
C2
C3
O2
C4
C5
N2
C6
N4
N3
N3C
N3B
N3A
N31
Cu2
N21
C32
C31
O31
O32
N33
C36
N32
C35
C34
C33
N34

Figure 3. 6 – Unit cell of **a)** $[Cu(\textit{L}{-}arg)_2(N_3)_2][Cu(\textit{L}{-}arg)_2Cl](N_3){\bullet}7H_2O$ **(4)** and **b)** $[Cu(\textit{L}{-}arg)_2(N_3)_2][Cu(\textit{L}{-}arg)_2(N_3)](N_3){\bullet}6H_2O$ **(6)** single-crystals with atom numbering.

Table 3. 6 – Crystallographic data and X-ray experimental details for **(4)** and **(6)**.

	(4)	**(6)**
Chemical formula	$C_{12}H_{28}CuN_{14}O_4$; $C_{12}H_{28}ClCuN_8O_4$, N_3, $7H_2O$	$C_{12}H_{28}CuN_{14}O_4$; $C_{12}H_{28}CuN_{11}O_4$, N_3, $6H_2O$
M_r	1111.58	1100.16
Crystal system, space group	Monoclinic, $P2_1$	Monoclinic, $P2_1$
Temperature (K)	100	100
***a, b, c* (Å)**	a=13.0861(7), b=15.3978(8), c=13.1094(7)	a=13.0201(5), b=15.3523(4), c=13.1005(5)
β (º)	114.609(7)	114.995(5)
V (Å^3)	2401.6(3)	2373.38(16)
Z	2	2
Radiation type	MoK_α	MoK_α
μ (mm^{-1})	1.03	0.98
Crystal size (mm)	0.31x0.25x0.22	0.29x0.27x0.22

Table 3. 7 – Selected geometric parameters (Å, deg) for **(4)** and **(6)** obtained by the X-ray diffraction studies.

Distances (Å)							
(4)				**(6)**			
Cu1−O11	1.945(6)	Cu2−N31	1.994(6)	Cu1−O1	1.954(3)	Cu2−O31	1.948(3)
Cu1−N1	2.037(5)	Cu2−O21	1.967(6)	Cu1−N1	2.015(3)	Cu2−N21	2.012(3)
Cu1−O1	1.964(6)	Cu2−N21	2.003(6)	Cu1−O11	1.962(3)	Cu2−O21	1.954(3)
Cu1−N11	2.016(6)	Cu2−Cl	2.470(3)	Cu1−N11	2.024(3)	Cu2−N31	2.016(3)
Cu2−O31	1.960(7)			Cu1−N1A	2.468(12)	Cu2−N3A	2.349(16)
Angles (º)							
O11−Cu1−N1	98.3(2)	N4A-N4B-N4C	169.5(10)	O1−Cu1−N1A	94.89(8)	N3B-N3A−Cu2	123.0
O11−Cu1−O1	178.7(3)	O31−Cu2−N31	84.2(3)	N1−Cu1−N1A	88.42(9)	O31−Cu2−O21	173.19(11)
N1−Cu1−O1	82.1(2)	O31−Cu2−O21	171.9(3)	O11−Cu1-N1A	89.05(8)	N21−Cu2−N31	167.53(13)
N1−Cu1−N11	176.4(3)	O31−Cu2−N21	95.3(3)	N11−Cu1-N1A	96.09(8)	N1A−N1B−N1C	178.5
O1−Cu1−N11	95.9(2)	N31−Cu2−O21	96.3(3)	O31−Cu2-N3A	95.09(9)	N2A−N2B−N2C	177.9
N11−Cu1−O11	83.6(2)	N31−Cu2−N21	169.6(3)	N21−Cu2-N3A	99.49(10)	N3A−N3B−N3C	175.1
N1AN1B-N1C	175.4(6)	O21−Cu2−N21	82.8(3)	O21−Cu2-N3A	91.62(9)	N4A−N4B−N4C	175.2
N2A-N2B-N2C	178.0(9)			N31−Cu2-N3A	92.98(9)		

The crystal structure of the complex $[Cu(L{-}arg)_2(H_2O)_2](N_3)_2$ **(7)** is depicted in Figure 3. 7 and the crystallographic data are presented in Table 3. 8.

Product 7 crystallizes in the monoclinic $P2_1$ symmetry with a relatively small unit cell ($V = 1096.03$ Å^3, see Table 3. 8). The unit cell is composed by the $[Cu(L{-}arg)_2(H_2O)_2]^{2+}$ complex cation and two azide ions (Figure 3. 7). The positive charge of the metal complex is a consequence of the protonated guanidinium groups of the *L*−arginine ligands and so the azide anions are necessary to attain charge neutrality. The two *trans*−chelated *L*−arg molecules coordinate to the central atom through one oxygen and one nitrogen atoms from the carboxylate and the amino groups, respectively. These atoms form a basal plane where the distances between $Cu{-}O_{L\text{-arg}}$ and $Cu{-}N_{L\text{-arg}}$ are in the range of 1.95 Å to 2.00 Å (in agreement with literature data[22,109,110,111]). The presence of two water molecules (O1W and O2W) in the apexes of the basal plane contributes with a distorted octahedral geometry around the copper(II) ion. The $Cu{-}O_{water}$ bonds (Cu−O1W 2.621 Å and Cu−O2W 2.497 Å) are long, but within the range of 2.2−2.9 Å known for the axial Cu–O bond lengths.[121] The two azide counterions participate in hydrogen bonds with the water molecules. Furthermore, the azide counterions adopt an almost linear geometry, which is confirmed by the N5−N6−N7 and N15−N16−N17 angles of 177.8(4)° and 178.9(4)°, respectively (see Table 3. 9).

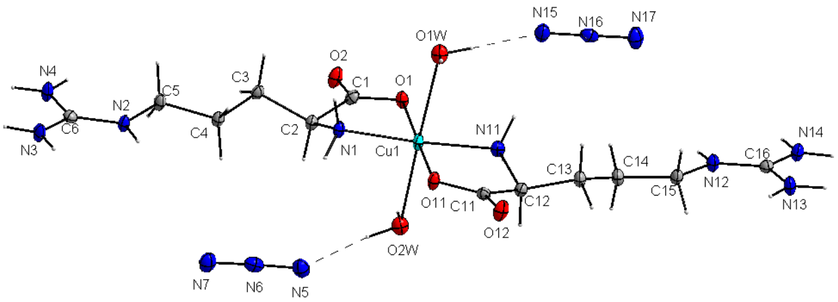

Figure 3. 7 – Unit cell of $[Cu(L{-}arg)_2(H_2O)_2](N_3)_2$ **(7)** single-crystals with atom numbering.

Table 3. 8 – Crystallographic data and X-ray experimental details for **(7)**.

Chemical formula	$C_{12}H_{32}CuN_8O_6$, $2N_3$
M_r	532.07
Crystal system, space group	Monoclinic, $P2_1$
Temperature (K)	100
a, b, c **(Å)**	a=7.5127(4), b=14.5342(8), c=10.0648(5)
β (°)	94.206(4)
V **(Å^3)**	1096.03(10)
Z	2
Radiation type	MoK_α
μ (mm^{-1})	1.06
Crystal size (mm)	0.30x0.26x0.20

Table 3. 9 – Selected geometric parameters (Å, deg) for **(7)** obtained by the X-ray diffraction studies.

(7)			
Distances (Å)		**Angles (º)**	
		O1−Cu−N1	82.57(11)
Cu−O1	1.964(3)	O1−Cu−O11	177.42(11)
Cu−N1	2.013(3)	O1−Cu−N11	96.18(11)
Cu−O11	1.946(3)	N1−Cu−O11	96.56(11)
Cu−N11	2.000(3)	N1−Cu−N11	176.05(13)
Cu−O1W	2.621	O11−Cu−N11	84.52(11)
Cu−O2W	2.497	N5−N6−N7	177.8(4)
		N15−N16−N17	178.9(4)

The PXRD patterns of **(4)**, **(6)** and **(7)** are depicted in Figure 3. 8. The obtained PXRD pattern for **(4)** is quite different from the theoretical one (see Figure 3. 8a). This can be either because i) the obtained crystal structure of the chosen single-crystal is not the dominant one in the sample or ii) over time, the product may have become hydrated and therefore it presents a different crystalline structure from the starting material. The experimental PXRD patterns of **(6)**, up to around 23º (2θ), is in a fairly good agreement with the predicted pattern, except at 8.91º and 13.15º (2θ) where those peaks do not have a correspondent peak in the predicted diffractogram (indicated by a dashed line in Figure 3. 8b). In the angular region between 25º to 30º (2θ), a strong discrepancy between the experimental and the theoretical patterns is observed, with strong peaks not matching the experimental pattern. These extra peaks may be due to the presence of a secondary phase, most likely a hydrated form, or a contaminant. In addition, the observed peaks seem to be slightly shifted when compared to the predicted ones, which could be due to a small misalignment of the sample. For **(7)**, all the experimental peaks were observed in the measured diffractogram but, again, in the region between 25º to 29º (2θ), two very intense peaks do not match the experimental ones. Despite the differences mentioned above, the PXRD patterns of these three products are completely different from those of the starting materials, indicating the formation of the metal complexes (Figure S. 12).

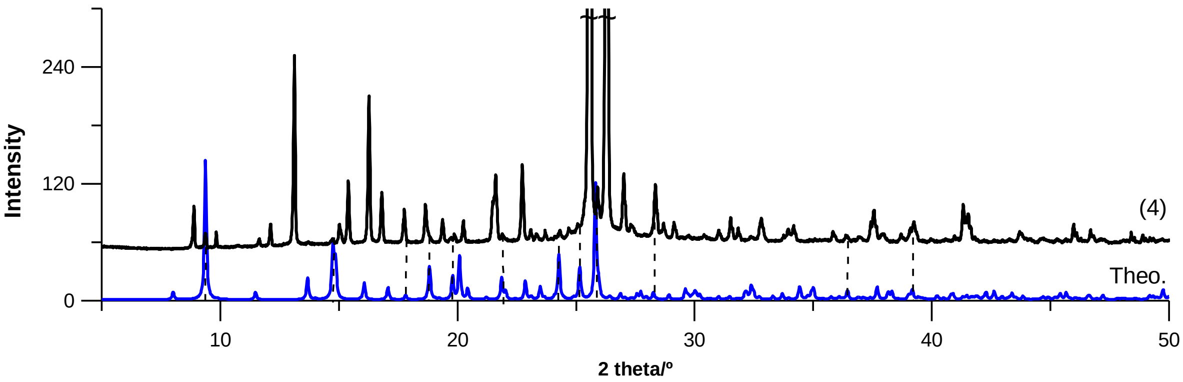

a)

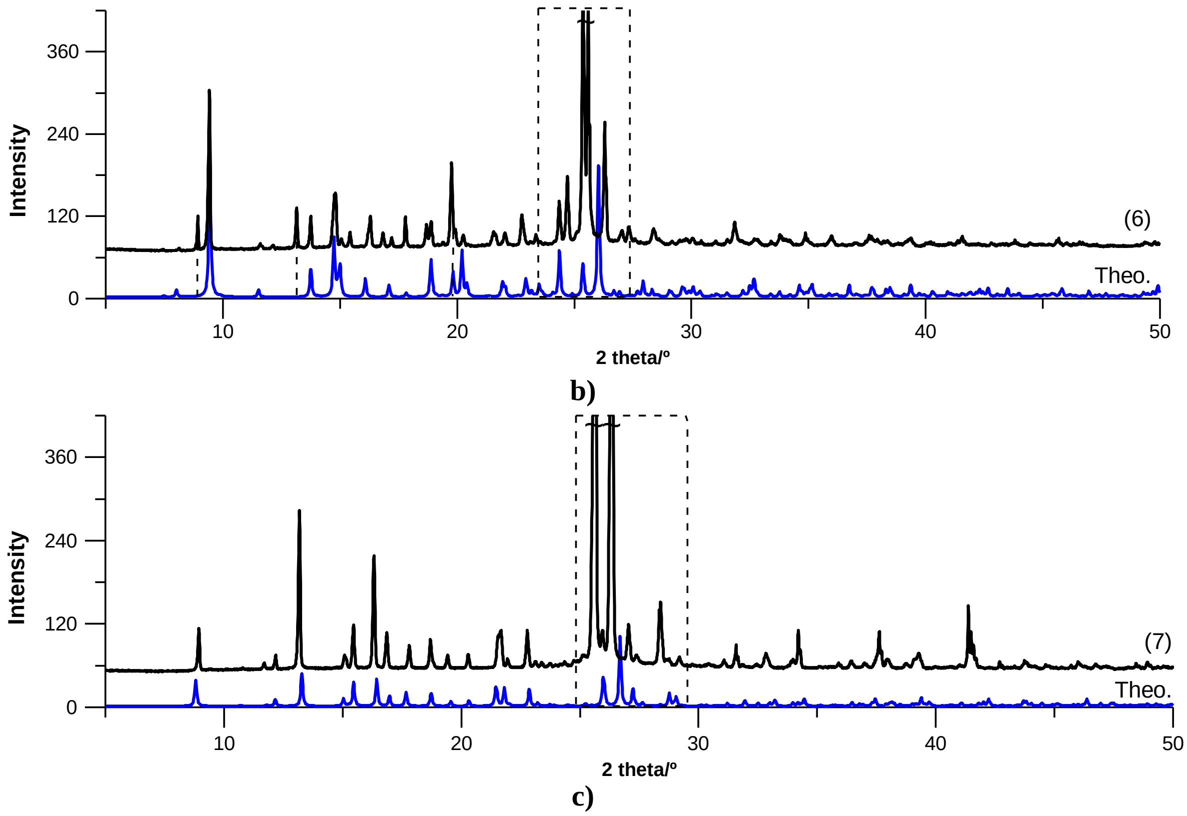

Figure 3. 8 – PXRD patterns obtained for **a) (4)**, **b) (6)** and **c) (7)** (black line). The blue line diffractograms (at the bottom) show the predicted positions and relative intensity of peaks calculated from the crystal structure obtained from the single X-ray diffraction. The inset highlights the mismatch between the experimental data (black line) and the theoretical one (blue line). The intensity of the peaks marked with a tilde (~) was truncated.

Products 5 and 8

The crystal structures of the coordination compounds $\{[Cu_2(L{-}arg)_2(N_3)_2(\mu{-}1,3{-}N_3)(\mu{-}1,1{-}N_3)][Cu(L{-}arg)(N_3)(\mu{-}1,1{-}N_3)]{\bullet}3H_2O\}_n$ **(5)** and $\{[Cu(L{-}arg)(N_3)(\mu{-}1,3{-}N_3)]\}_n$ **(8)** are shown in Figure 3. 9 and the crystallographic data presented in Table 3. 10.

Product 5 crystallizes in an orthorhombic crystal system, $P2_12_12_1$ space group. The unit cell is composed by two MC with a total of three Cu(II) centers, three *L*−arg ligands, seven azide ions and three lattice water molecules (see Figure 3. 9a1). All of the Cu(II) centers are five-coordinated by one *L*−arg molecule and by different azide ions. The *L*−arg ligands are similar to each other and chelate to the different Cu(II) ions through one oxygen and one nitrogen atoms from the carboxylate and the amino groups, respectively. The experimental distances between the Cu(II) centers and the O,N atoms from the *L*−arg molecules range from 1.96−2.00 Å (typical values according to the literature[22,109,110,111]). For the azide ions, a monodentate coordination (N2−N3−N4, N32−N34−N35 and N52−N53−N54) as well as two types of bridging (N12−N13−N14 and N22−N23−N24/N42−N43−N44) are observed. For the Cu(II) dimer (Figure 3. 9a2), the monodently coordinated azide ions are distanced to Cu1 (Cu−N2) and Cu2 (Cu−N32) atoms by 1.97 and 1.96 Å, respectively (Table 3. 11). On the other hand, the N12−N13−N14 azide ion plays as an end-to-end bridge, where the N12 and N14 atoms are respectively linked to Cu1 and Cu2 with bond lengths of 2.03 and 2.51 Å. According to the literature, the typical distances between Cu(II) centers and the N atom from the azide anion should be less than 2 Å,[122,123,124,125] meaning that this bridge is weakly coordinated to the metal ions. The distance between Cu1 and Cu2 equals 5.28 Å, so they are largely separated to each other.[126,127,128] On the other hand, the N22−N23−N24 azide ion plays as a single-atom bridge that coordinates to both Cu1 and Cu2 through the N22 atom. The distances between Cu1−N22 and Cu2−N22 are 2.47 and 1.98 Å, respectively, while Cu1···Cu2 are distanced by 3.57 Å. The distances between the metal centers in the polymeric Cu1−Cu2−Cu1−Cu2 chain suggest the long and short contact of Cu(II) ions. Looking to Figure 3. 9a3), it is possible to note the double coordination pattern of the azide ligands (monodently coordinated and bridged) and the polymeric nature of the MC. In this case, the monodently coordinated N52−N53−N54 azide ion is distanced to Cu3 by 1.88 Å and it is slightly deviated from linearity by presenting a 163^{o} angle value (see Table 3. 11). In the single-atom N42−N43−N44 azide bridge, the N42 atom is distanced to Cu3 by an average of 2.125 Å.

Product 8 crystallizes in a monoclinic crystal system with $P2_1$ space group. The unit cell is composed by one Cu(II) ion that is five-coordinated by chelating carboxylate oxygen and amine nitrogen atoms from one *L*−arg molecule and by three azide ions (see Figure 3. 9b1). The coordination sphere is described as a square pyramid with a τ parameter of 0.0453 (β [O1−Cu−N5] = 175.4 and α [N8−Cu−N1] = 172.68). The distances from the Cu(II) ion to basal O1 oxygen and N1 nitrogen (from *L*−arg) are in the range of 1.97−2.00 Å, in a close agreement with other Cu(II):*L*−arg coordination compounds.[22,109,110,111] The N8−N9−N10 azide ligand is monodently coordinated to Cu(II) ion and the Cu−N8 atoms are distanced by 1.98 Å (in agreement with literature data[122,123,124,125]). The N8−N9−N10 azide adopts an almost linear geometry that is confirmed by the 178.5^{o} angle (Table 3. 11). The N5−N6−N7 azide ion plays as an end-to-end bridge (Figure 3. 9b2) and the distances between Cu−N5 and Cu−N7 are 1.98 and 2.55 Å, respectively. These different bond lengths contribute to an asymmetric projection of the chain, where both Cu(II) centers are separated to each other by 5.33 Å.

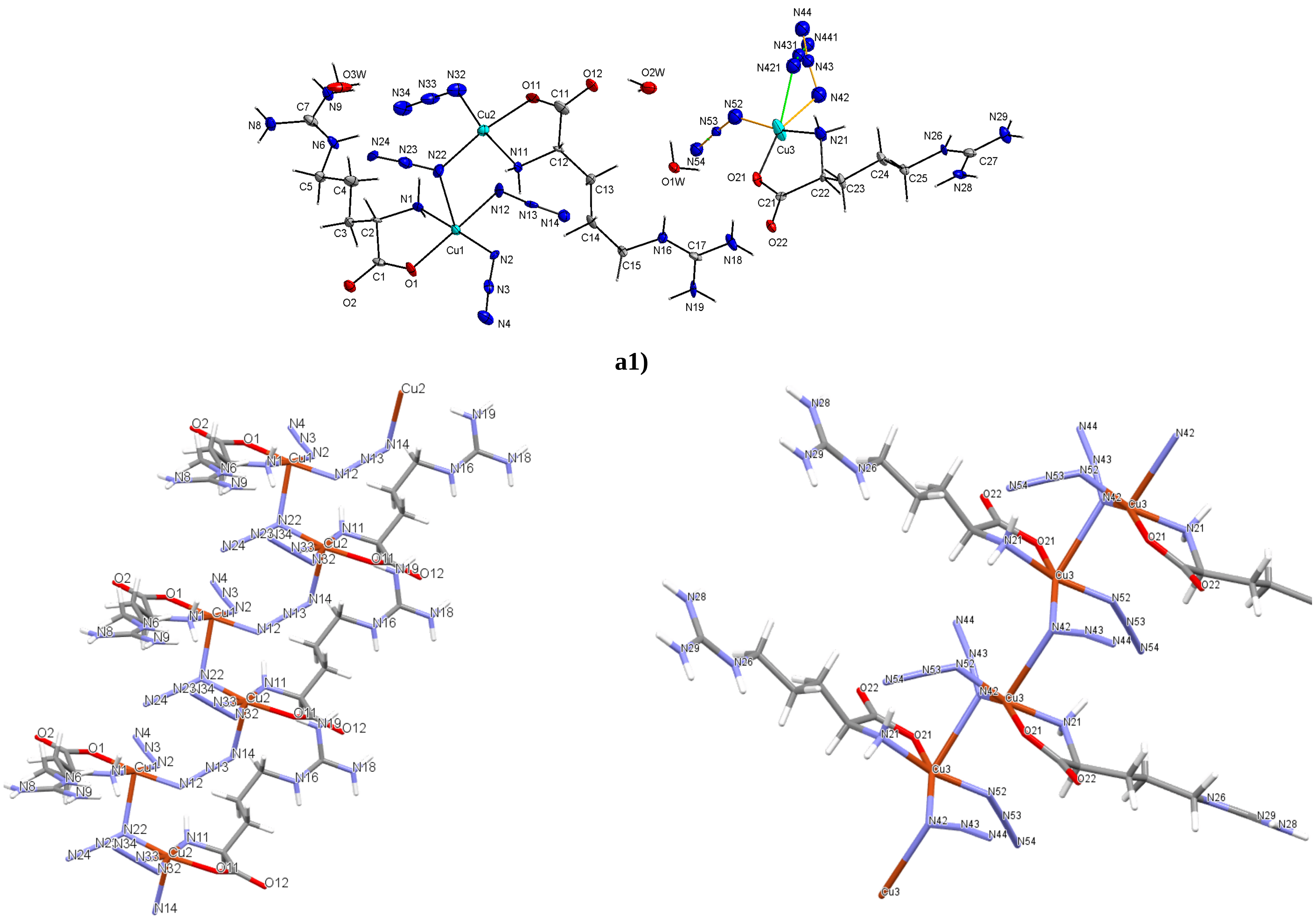
O3W
N9
C7
N8
N6
C5
C4
C3
C2
N1
C1
O1
O2
Cu1
N2
N3
N4
N34
N33
N32
Cu2
N24
N23
N22
O11
C11
O12
N11
C12
N12
N13
N14
C13
C14
C15
N16
C17
N18
N19
O2W
O1W
N52
N53
N54
N44
N441
N431
N421
N43
N42
Cu3
N21
O21
C21
O22
C22
C23
C24
C25
N26
C27
N29
N28

a1)

a2)

a3)

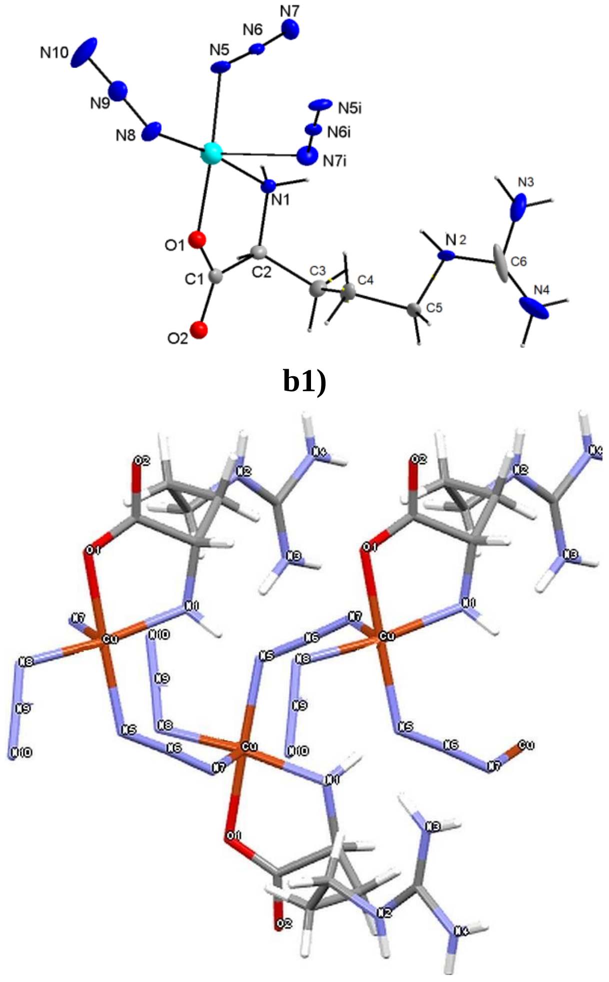

b1)

b2)

Figure 3. 9 – Unit cell of **a)** $\{[Cu_2(L{-}arg)_2(N_3)_2(\mu{-}1,3{-}N_3)(\mu{-}1,1{-}N_3)][Cu(L{-}arg)(N_3)(\mu{-}1,1{-}N_3)]\bullet 3H_2O\}_n$ **(5)** and **b)** $\{[Cu(L{-}arg)(N_3)(\mu{-}1,3{-}N_3)]\}_n$ **(8)** single-crystals with atom numbering.

Table 3. 10 – Crystallographic data and X-ray experimental details for **(5)** and **(8)**.

	(5)	**(8)**
Chemical formula	$2(C_{12}H_{28}Cu_2N_{20}O_4)$ $2(C_6H_{14}CuN_{10}O_2)$ $4(H_2O)\bullet H_2O$	$C_6H_{14}CuN_{10}O_2$
M$_r$	2020.95	321.82
Crystal system, space group	Orthorhombic, $P2_12_12_1$	Monoclinic, $P2_1$
Temperature (K)	100	100
a, b, c (Å)	6.8684(1), 12.1770(2), 46.6560(6)	8.4966(5), 5.8681(2), 12.5380(5)
β (°)	90	91.339(5)
V (Å^3)	3902.14(10)	624.96(5)
Z	2	2
Radiation type	MoK_α	MoK_α
μ (mm^{-1})	1.71	1.766
Crystal size (mm)	0.29x0.13x0.12	0.28x0.24x0.21

Table 3. 11 – Selected geometric parameters (Å, deg) for **(5)** and **(8)** obtained by the X-ray diffraction studies.

Distances (Å)					
(5)				**(8)**	
Cu1−N2	1.965(7)	Cu2−N14	2.505(3)	Cu−O1	1.973(3)
Cu−O1	1.987(6)	Cu3−N52	1.881(19)	Cu−N1	1.998(3)
Cu1−N1	1.993(7)	Cu3−N421	2.11(2)	Cu−N5	1.977(3)
Cu1−N22	2.473(9)	Cu3−N42	2.14(3)	Cu−N8	1.987(3)
Cu1−N12	2.037(7)	Cu3−N21	1.964(8)	Cu−N7	2.548(3)
Cu2−N32	1.962(10)	Cu3−O21	1.967(7)	Cu…Cu	5.330 (4)
Cu2−O11	1.963(7)	Cu1…Cu2	5.278; 3.566		
Cu2−N11	1.996(7)	Cu3…Cu3	3.838		
Cu2−N22	1.977(8)				
Angles (º)					
N2−Cu1−O1	97.1(3)	N52−Cu3−N421	94.7(10)		
N2−Cu1−N1	176.2(3)	N52−Cu3−N42	91.3(9)		
N2−Cu1−N22	94.4(3)	N52−Cu3−N21	167.4(8)		
N2−Cu1−N12	89.9(3)	N52−Cu3−O21	99.3(6)		
O1−Cu1−N1	83.1(3)	N421−Cu3−N21	88.3(7)	O1−Cu−N8	89.45(13)
O1−Cu1−N22	101.2(3)	N421−Cu3−O21	154.4(7)	O1−Cu−N5	175.40(14)
O1−Cu1−N12	170.6(3)	N42−Cu3−N21	90.9(7)	O1−Cu−N1	83.39(11)
N1−Cu1−N22	89.3(3)	N42−Cu3−O21	157.8(8)	N8−Cu−N5	89.91
N1−Cu1−N12	89.6(3)	N21−Cu3−O21	83.0(3)	N8−Cu−N1	172.68(15)
N22−Cu1−N12	84.5(3)	N2−N3−N4	176.2(10)	N5−Cu−N1	97.10(13)
N32−Cu2−O11	87.7(4)	N12−N13−N14	177.8(10)	N5−N6−N7	176.6(4)
N32−Cu2−N11	171.2(4)	N22−N23−N24	179.0(7)	N8−N9−N10	178.5(5)
N32−Cu2−N22	97.3(4)	N32−N33−N34	175.2(9)		
O11−Cu2−N11	83.7(3)	N42−N43−N44	169(3)		
O11−Cu2−N22	170.5(3)	N421−N431−N441	177(3)		
N11−Cu2−N22	91.1(3)	N52−N53−N54	163(3)		

Since the yield of the synthesis of product 5 was too low (around 3%), it was repeated several times in order to obtain a sufficient amount of crystalline material. However, such attempts were unsuccessful, so it was not possible to collect the powder X-ray diffractogram (see Figure S. 13 for the predicted PXRD pattern). The collected PXRD pattern of **(8)**, presented in Figure 3. 10, matches the theoretical one (based on the single-crystal structure). The collected diffractogram shows sharp and intense peaks that indicate high crystallinity. The differences in relative intensity for some peaks may be related with texture (preferred orientation) effects. Only a few peaks do not perfectly match, probably due to a very small amount of impurities. The comparison of the PXRD patterns of product 8 and the ligands used in its synthesis are represented in Figure S. 14. Again, the PXRD diffractogram of **(8)** is completely different from those of the starting materials, being indicative of the metal complex formation.

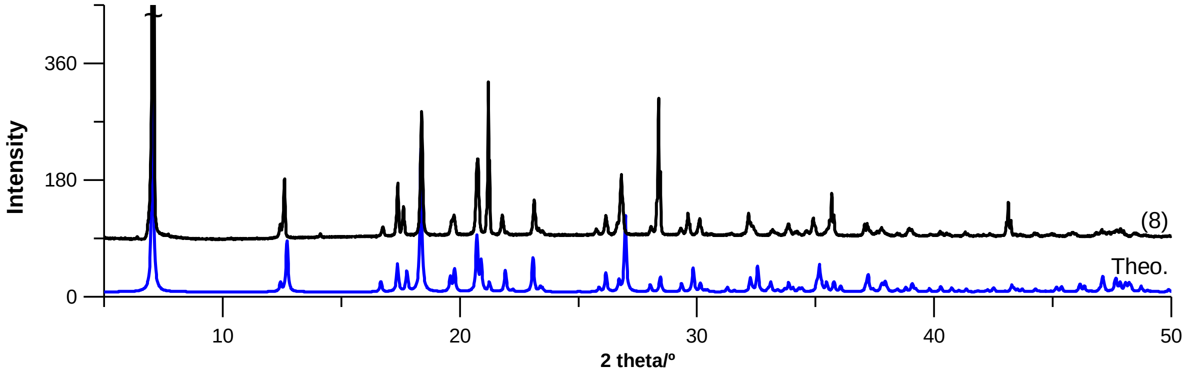

Figure 3. 10 – PXRD pattern obtained for **(8)** (black line). The blue line diffractogram (at the bottom) shows the predicted positions and relative intensity of peaks calculated from the crystal structure obtained from the single X-ray diffraction. The intensity of the peak marked with a tilde (~) was truncated.

3.3. Infrared spectroscopy

a) [Cu(*L*−arg)$_2$](NO$_3$)$_2$•3H$_2$O (1)

The FT-IR spectrum of **(1)** is presented in Figure 3. 10. The broad absorption at *ca.* 3250 cm^{-1} is assigned to the ν(OH) stretching vibration in the water molecules, while the sharp bands with maxima at 3348, 3272 and 3199 cm^{-1} correspond to the ν_{as}(NH$_2$) and ν_s(NH$_2$) stretching vibrations in the *L*−arginine guanidinium group.[129] The bands centered at 1693, 1629 and 1589 cm^{-1} shall be assigned to the guanidinium group amino scissoring δ(NH$_2$), to the guanidinium group asymmetric stretching ν_{as}(CNN) and to the asymmetric stretching of the carboxylate group ν_{as}(COO$^-$).[130,131] The band found at 1384 cm^{-1} indicates the presence of uncoordinated NO$_3^-$ ions,[132] while the one at 1350 cm^{-1} is assigned to the wagging vibration mode ω(CH$_2$) of the *L*−arginine methylene group.[130]

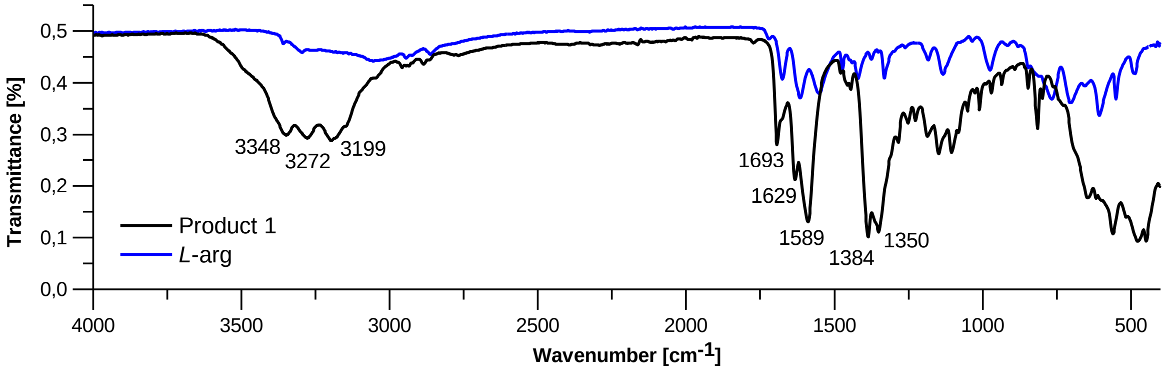

Figure 3. 11 – FT-IR spectra of product 1 (black line) and *L*-arginine (blue line).

b) $[Cu(\textit{L}-arg)_2(SCN)_2]\bullet 2H_2O$ (2) and $[Cu(\textit{L}-arg)(SCN)_2]$ (3)

The FT-IR spectra of both products 2 and 3 is shown in Figure 3. 12. Unlike to what was observed in the spectrum of **(1)**, a very intense and characteristic band is centered at 2102 and 2088 cm^{-1} for **(2)** and **(3)**, respectively, being ascribed as the stretching vibration ν(CN) of the thiocyanate ligand.[133,134] Similarly to the bands assigned to the product 1, the spectra of products 2 and 3 contain a set of intense bands in the [1680−1590 cm^{-1}] spectral range. The vibrational nature of these bands must be similar to the one discussed before for **(1)**, *i.e.* it should be attributed to the amino group scissoring mode, but also to the asymmetric stretching of the guanidinium and carboxylate groups.[130,131] The bands found at 1377 and 1347 cm^{-1} for **(2)** and at 1374 and 1338 cm^{-1} for **(3)** should be ascribed as the symmetric stretching $\nu_s(COO^-)$ of the carboxylate group and/or the wagging vibration mode $\omega(CH_2)$ of the methylene group.[135,136]

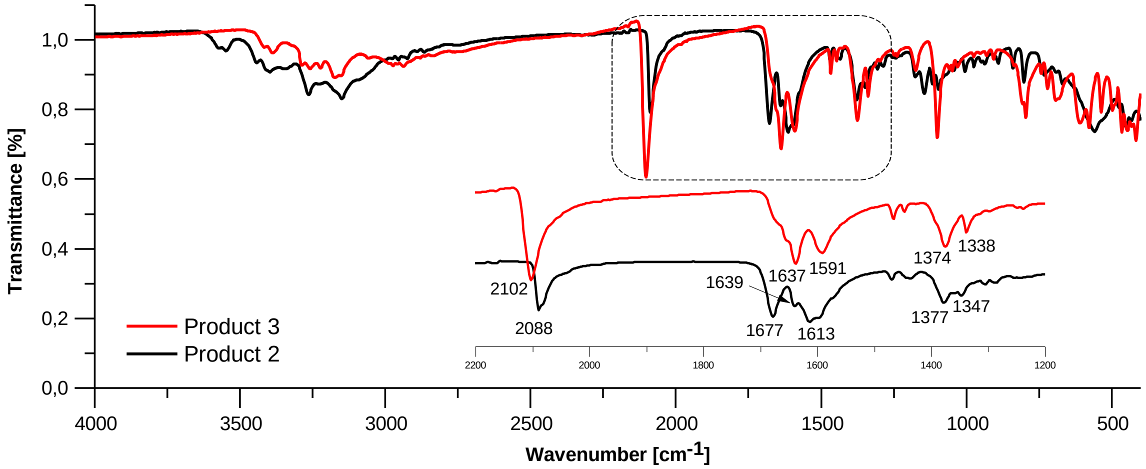

Figure 3. 12 – FT-IR spectra of product 2 (black line) and 3 (red line). The inset highligts the [2200 – 1200 cm^{-1}] region.

c) $[Cu(\textit{L}-arg)_2(N_3)_2][Cu(\textit{L}-arg)_2Cl](N_3)\bullet 7H_2O$ (4), $[Cu(\textit{L}-arg)_2(N_3)_2][Cu(\textit{L}-arg)_2(N_3)](N_3)\bullet 6H_2O$ (6) and $[Cu(\textit{L}-arg)_2(H_2O)_2](N_3)_2$ (7)

The FT-IR spectra of **(4)**, **(6)** and **(7)** is characterized by an intense band in the frequency range of 2069−2026 cm^{-1} (see Figure 3. 13). Although very similar to the thiocyanate ν(CN) band (observed for products 2 and 3), the former is shifted to lower frequencies and is assigned to the asymmetric stretching vibration of the azide group $\nu_{as}(N_3)$.[137,138] The multiple splitting with maxima at 2069 and 2056 cm^{-1} for **(4)**, 2066 and 2026 cm^{-1} for **(6)** and 2066 and 2057 cm^{-1} for **(7)** suggests the presence of two types of N_3^- ions, *i.e.* coordinated and uncoordinated. The bands found at 1683, 1637 and 1590 cm^{-1} for **(4)**, at 1683, 1632 and 1602 cm^{-1} for **(6)** and at

1693, 1633, 1602 and 1589 cm^{-1} for **(7)** are related to the $\delta(NH_2)$, $\nu_{as}(CNN)$ and $\nu_{as}(COO^-)$ vibrations.[130,131] The ones located at 1390 and 1345 cm^{-1} for these three products may be assigned to the $\nu_s(COO^-)$ and/or the wagging vibration mode $\omega(CH_2)$ of the methylene group.[135,136] The difference between the $\nu_{as}(COO^-)$ and $\nu_s(COO^-)$ frequencies, *i.e.* the splitting values $\Delta\nu(COO^-)$ between the two carboxylate vibrations lie within the range of 255−335 cm^{-1} for products 4, 6 and 7, as commonly reported for compounds with a monodentate bonding of the carboxylate group[136,139]

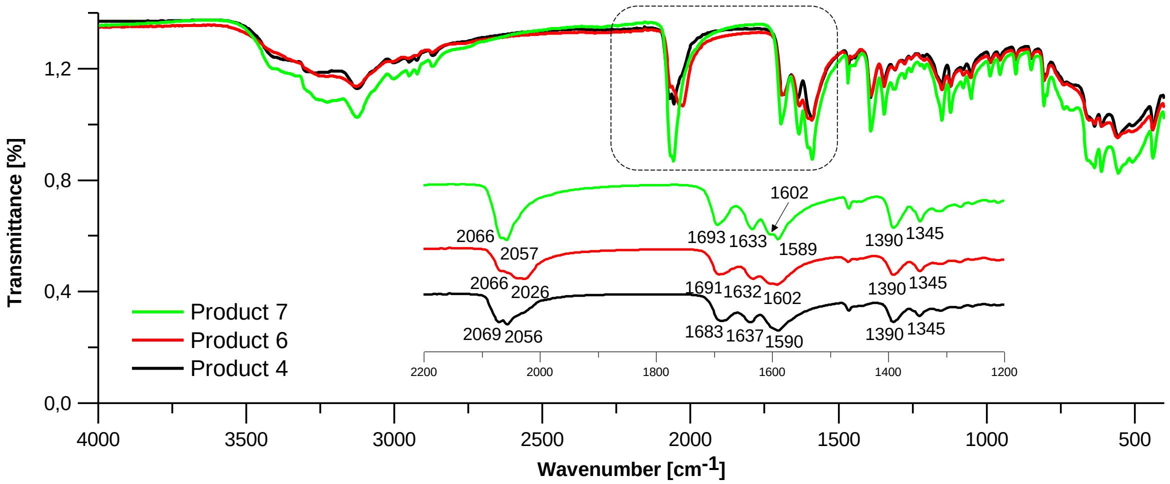

Figure 3. 13 – FT-IR spectra of products 4 (black line), 6 (red line) and 7 (green line). The inset highligts the [2200 – 1200 cm^{-1}] region.

d) {[Cu_2(*L*−arg)$_2$(N_3)$_2$(μ−1,3−N_3)(μ−1,1−N_3)][Cu(*L*−arg)(N_3)(μ−1,1−N_3)]•3H_2O}$_n$ (5) and {[Cu(*L*−arg)(N_3)(μ−1,3−N_3)]}$_n$ (8)

Similarly to the spectra depicted in Figure 3. 13, a strong band displayed across the [2090−2033 cm^{-1}] range can be observed and assigned to the asymmetric stretching of the azide group $\nu_{as}(N_3)$ (see Figure 3. 14).[137,138] In both products 5 and 8, the azide groups are no longer solely monodently coordinated or behaving as counterions (as it is in the case of products 4, 6 and 7). This time, these ligands are also arranged as bridges, resulting in a more pronounced split of this particular vibrational mode. For instance, in the case of product 5, two types of bridges were observed in the crystal structure (see Figure 3. 9a), which may be correlated with the two observed components of the $\nu_{as}(N_3)$ band, centered at 2070 and 2033 cm^{-1}. At lower frequencies, the FT-IR spectra of products 5 and 8 are dominated by the previous discussed *L*−arginine bands: a very broad and splitted set of bands ranging from 1690 to 1580 cm^{-1}, which shall contain the overlapping $\nu_{as}(COO^-)$, $\nu_{as}(CNN)$ and $\delta(NH_2)$ vibrations, and the bands found in the region of 1400−1380 cm^{-1}, which shall be assigned to the symmetric stretching of the carboxylate group and/or to the wagging mode of the methylene group.[135,136]

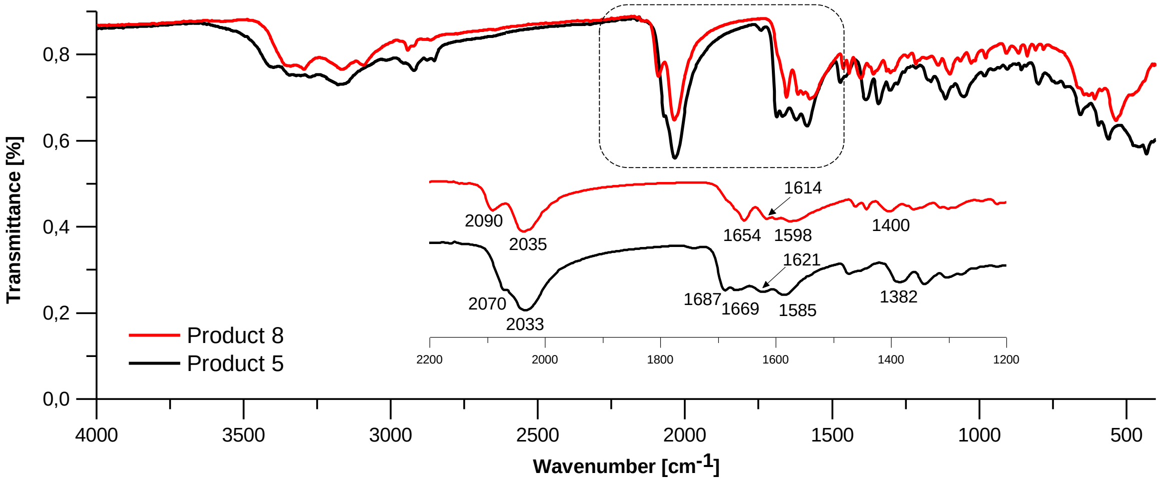

Figure 3. 14 – FT-IR spectra of products 5 (black line) and 8 (red line). The inset highligts the [2200 – 1200 cm^{-1}] region.

Detailed analysis of SCN^{-} and N$_3^{-}$ bands in FT-IR spectra

Thiocyanate and azide are triatomic ions that can act as counterions or as ligands (monodentate or bridging ligands) in the MC.

Thiocyanate Lewis structure can be described by two distinct resonance structures (see Figure 1. 5a) and hence coordinate with the metal center ion either through sulfur or nitrogen atoms.[140] However, in metals of Class A (which is the case of copper(II) ions), the coordination typically occurs through the nitrogen atom[141] (like it is observed for both products 2 and 3). The S− or N− coordinated thiocyanate gives rise to different vibrational frequencies of this ligand, which allows to correlate the coordination pattern with the wavenumber changes of the SCN^{-} vibrations,[142] *i.e.* the stretching C−N vibration ν(CN), the stretching C−S vibration ν(CS) and the doubly degenerated in-plane and out-of-plane deformation vibration δ(NCS).[140] An allusive representation of the atom displacement upon these vibrational modes is shown in Figure 3. 15. Note that the different geometric figures are an analogy to the different chemical elements of the thiocyanate ion.

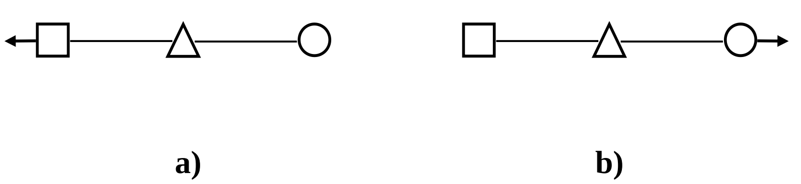

Figure 3. 15 –Vibrational normal modes of the SCN^- ion. **a)** C−N stretching ν(CN), **b)** C−S stretching ν(CS) and **c)** degenerated in-plane and out-of-plane bending modes δ(NCS). Adapted from ref. [143].

The comparison of the infrared bands of the free thiocyanate and products 2 and 3 is presented in Figure 3. 16. The frequency values of ν(CN), ν(CS) and δ(NCS) vibrations are reported in Table 3. 12. The thiocyanate deformation frequencies are above 450 cm^{-1}, suggesting that the coordination with the central atom occurs through the thiocyanate nitrogen atom[144] (in agreement with the X-ray crystal structure data, see Figure 3. 4). The ν(CS) bands are normally weak and therefore challenging to identify. However, the comparison of the metal complexes and the free thiocyanate bands allowed the proposed assignment of this particular vibration mode, located in the [810−800 cm^{-1}] range, as it lies within the range for others N−coordinated structures (between 870−760 cm^{-1}).[140,144] The C−N stretching vibration in KSCN is found at 2036 cm^{-1}, while in the spectra of products 2 and 3 this vibration generate higher energetic bands (near or below 2100 cm^{-1}), indicating, once more, that the thiocyanate group is linked to the central metal through the nitrogen atom (since otherwise this band would be found above 2100 cm^{-1}).[140,144]

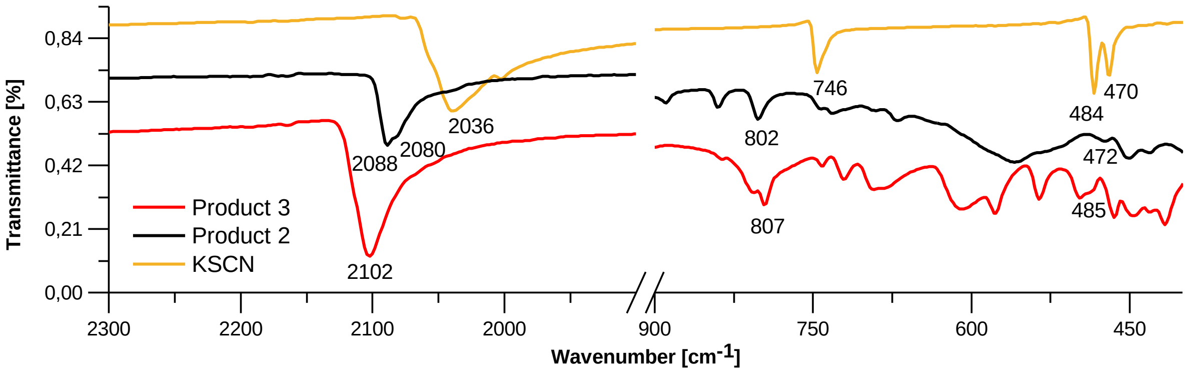

Figure 3. 16 – FT-IR spectra of pure KSCN (orange line), and of products 2 and 3 (black and red lines, respectively).

Table 3. 12 – Vibrational frequencies (in cm^{-1}) of the ν(CN), ν(CS) and δ(NCS) bands for the pure KSCN and for the coordinated one (in products 2 and 3).

Compound	ν(CN)	ν(CS)	δ(NCS)
KSCN	2036	746	484, 470
Product 2	2088, 2080	802	472
Product 3	2102	807	485

For the remaining products (4-8), sodium azide salt was used in the MC preparation. The uncoordinated N_3^- ions structure contains equal bond distances between the three nitrogen atoms. However, upon coordination, that is no longer the case. The structure of the azide remains linear, but the bond lengths are affected.[145] Thus, the IR spectra analysis of the N_3^- vibrational modes (asymmetric stretching vibration $\nu_{as}(N_3)$, symmetric stretching vibration $\nu_s(N_3)$ and doubly degenerated deformation frequency $\delta(N_3)$, see Figure 3. 17) shall give valuable insight in the interpretation of how the metal center is coordinated by the azide ligand.

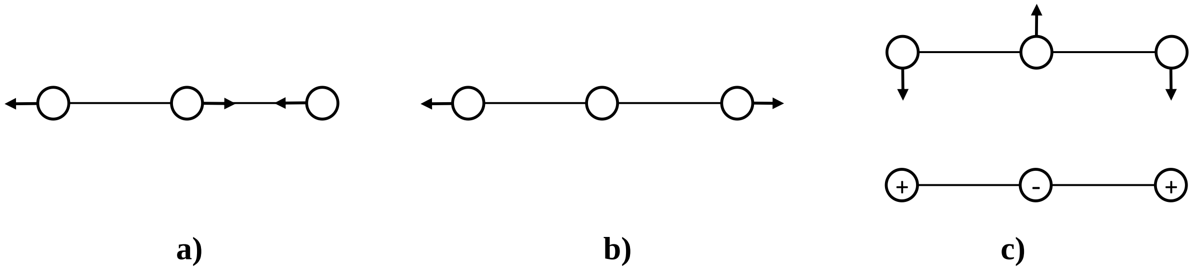

Figure 3. 17 –Vibrational normal modes of the N_3^- ion. **a)** asymmetric stretching $\nu_{as}(N_3)$, **b)** symmetric stretching $\nu_s(N_3)$ and **c)** degenerated in-plane and out-of-plane bending modes $\delta(N_3)$. Adapted from ref. [143].

The infrared spectra of products 4-8 and pure NaN_3 salt are compared in Figure 3. 18. For simplicity purposes, the FT-IR spectra of the metal complexes was separated into three different regions: i) the $\delta(N_3)$ bending region (640−590 cm^{-1}), ii) the $\nu_s(N_3)$ symmetric stretching region (1405−1340 cm^{-1}) and iii) the $\nu_{as}(N_3)$ antisymmetric stretching region (2090−2030 cm^{-1}). The frequency values of these vibrations are summarized in Table 3. 13. Additionally, the ν(MN) stretching vibration between the copper(II) metal center and the coordinated azide nitrogen atom is also included. A weak to medium intensity band between 437 and 430 cm^{-1} is observed for products 4, 5 and 6, being comparable with other previously reported cases.[146]. For product 7, it is also observed a band around 437 cm^{-1}. However, as it is possible to confirm by the crystal structure (see Figure 3. 7), there is no coordination between the azide ligand and the copper(II) center, suggesting that this band may be to the Cu-N$_{L\text{-arg}}$ bond. For product 8, the ν(MN) stretching band in the [450−400 cm^{-1}] range is very poorly observed. The bending $\delta(N_3)$

vibration mode in products 4-8 is shifted to lower frequency values when compared to the frequency for the free azide ion (636 cm^{-1}). As expected, no symmetric stretching vibration $\nu_s(N_3)$ is observed in the free azide spectrum, since this vibration is not infrared active. However, upon coordination with the metal center, this vibrational mode becomes active. For products 4, 6 and 7 two low to medium intensity components of this band are found at 1390 and 1344 cm^{-1}, while for products 5 and 8 these components are centered at 1382/1340 cm^{-1} and at 1404/1354 cm^{-1}, respectively. For both products 5 and 8, the $\nu_s(N_3)$ band has very low intensity, which might be a consequence of the azide bridge pattern. In fact, upon its bridging coordination, this mode becomes almost infrared inactive (see Figure 3. 18**)**. Finally, upon coordination, the asymmetric stretching $\nu_{as}(N_3)$ of all the products show a shift to lower frequencies in the [2090–2020 cm^{-1}] spectral range, comparing to pure NaN_3 found at 2102 cm^{-1}. In the spectrum of **(7)**, the maxima are close to each other (2065 and 2057 cm^{-1}), which is caused by the uncoordinated N_3^- ions in crystal structure (see Figure 3. 7). If the N_3^- is monodently or bridged coordinated, the separation of the band components, assigned as $\nu_{as}(N_3)$, increases (as in the cases of products 4, 5, 6 and 8).

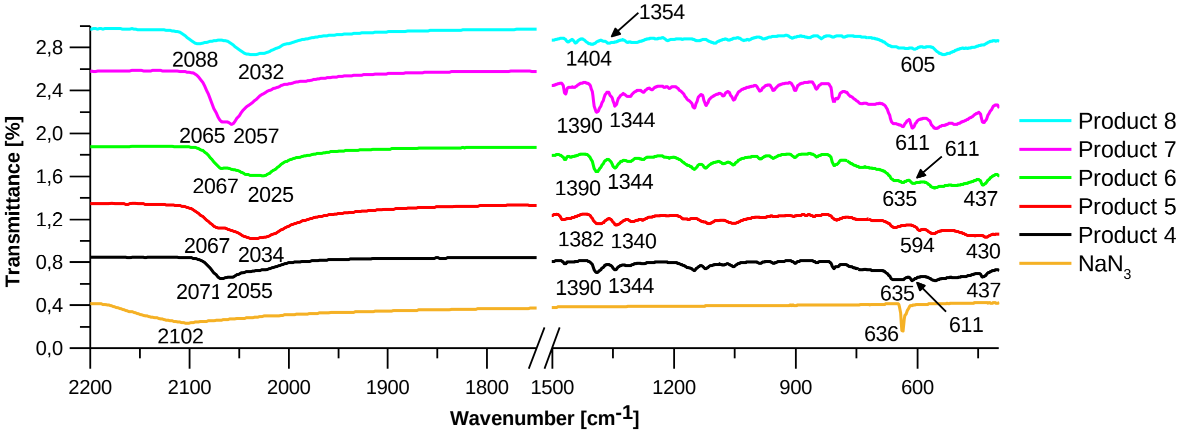

Figure 3. 18 – FT-IR spectra of pure NaN_3 (orange line), and of products 4 (black), 5 (red), 6 (green), 7 (pink) and 8 (blue).

Table 3. 13 – Vibrational frequencies (in cm^{-1}) of the $\nu_{as}(N_3)$, $\nu_s(N_3)$, $\delta(N_3)$ and $\nu(MN)$ bands for the pure NaN_3 and for the coordinated one (in products 4-8).

Compound	**$\nu_{as}(N_3)$**	**$\nu_s(N_3)$**	**$\delta(N_3)$**	**$\nu(MN)$**
NaN_3	2102	–	636	–
Product 4	2071, 2055	1390, 1344	635, 611	437
Product 5	2067, 2034	1382, 1340	594	430
Product 6	2067, 2025	1390, 1344	635, 611	437
Product 7	2065, 2057	1390, 1344	611	–
Product 8	2088, 2032	1404, 1354	605	–

3.3. Magnetic properties

The copper(II) ions carry an individual magnetic moment due to one free electron that is not paired with other electrons (d^9). Typically, a Cu(II) salt is paramagnetic, with atomic magnetic moments of the metal ion disordered due to thermal motion. However, when such ions are exposed to an external magnetic field (*H*), they acquire a small magnetization (*M*) that is due to the alignment of the magnetic moment of the unpaired electrons with the applied field. The magnetic susceptibility (χ) is defined as:

$$\chi = \frac{M}{H} \qquad \text{Eq.3. 2}$$

where the magnetization *M* is defined as the magnetic moment per unit volume (alternatively, the susceptibility can be defined with the magnetization per unit mass, χ_g, or mol, χ_M). The susceptibility of a paramagnetic substance varies with temperature in a characteristic way (to be described below), from which it is possible to infer the value of the atomic magnetic moment.

The magnetic susceptibility of **(2)**, **(4)**, **(6)**, **(7)** and **(8)** was measured under an applied field of 0.5 T and in the temperature range 1.8–300 K, both in the field-cooled (FC) and zero field-cooled regime (ZFC). The FC and ZFC curves gave very similar results, as expected for a paramagnetic substance. For products 1 and 3, there were not performed magnetometric studies because they are already described in literature (see ref. [147] for product 1 and refs. [106,107] for product 3). For product 5, it was also not possible to do the measurements because there was not enough material available.

The temperature dependence of the magnetic susceptibility of a paramagnet is described by the Curie's law. The law states that the magnetization of a material is inversely proportional to temperature and mathematically can be expressed as:

$$\chi = \frac{C}{T} = \frac{M}{H} \qquad \text{Eq.3. 3}$$

where C is a material-specific Curie constant and is given, in SI units, by:

$$C = \frac{\mu_0 N g^2 \mu_B^2 J(J+1)}{3k_B}$$

and *N* is the number of magnetic atoms per unit of volume, μ_B the Bohr magneton, J the angular momentum quantum number and k_B the Boltzmann constant.

The theoretical effective magnetic moment of the Cu(II) ion is 1.73 μ_{B} and observed values typically range between 1.70 and 2.20 μ_{eff}. The deviations from the ideal spin-only value account for any small contribution of orbital moment, typically quenched (L ~0) in crystalline compounds.

In all the studied products, the magnetization followed the related Curie-Weiss law, which describes the magnetic susceptibility of paramagnetic compounds for compounds that have a residual magnetic interaction that would tend to align the magnetic moments, either ferromagnetically or antiferromagnetically, at a very low temperature:

$$\chi_M = \frac{C}{T - \theta} + \chi_0 \qquad \text{Eq.3. 4}$$

here the Curie-Weiss temperature θ is a small positive number for compounds with residual ferromagnetic interactions and a small negative number for those with antiferromagnetic interactions. The temperature independent term, χ_0, accounts for a diamagnetic contribution of the non-magnetic atoms. By fitting such law to the measured susceptibility, one can extract the effective magnetic moment of the magnetic ions from the value of the C constant. From the value and sign of θ, it is possible to deduce the presence of residual ferromagnetic or antiferromagnetic exchange interactions between these ions.

The magnetic susceptibility of product 2 (Figure 3. 19) shows the Curie-Weiss behavior in the whole temperature range with a Weiss constant (θ) of −0.05 K and an effective magnetic moment of 1.83 μ_{B}. This value is close to the theoretical value for the Cu(II) ions and in agreement with other values found for Cu(II) compounds.[148] The χ_M *versus* temperature plot displays the typical paramagnetic behavior with a Curie-Weiss temperature close to zero.

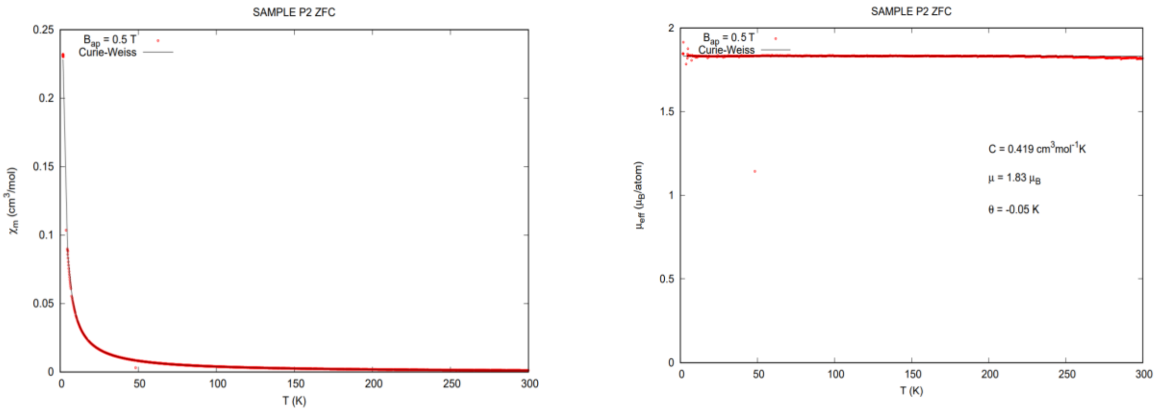

a) **b)**

Figure 3. 19 – a) Representation of the magnetic molar susceptibility *versus* temperature and **b)** representation of the effective magnetic moment *versus* temperature for product 2.

The magnetic properties of products 4 and 6 are shown in Figure 3. 20. Again, the χ_M values do not deviate significantly from the Curie law. Figure 3. 21 depicts the effective magnetic moment (μ_{eff}) *versus* T for **(4)** and **(6)** with the fitted Weiss constants of −0.06 K for both products and magnetic moments of 1.86 and 1.88 μ_B for **(4)** and **(6)**, respectively. These last values lie within the range of observed values for others Cu(II) compounds.[148] In these two compounds, the negative sign of the fitted θ constant would point the presence of antiferromagnetic interactions between the Cu(II) ions, but the small absolute value of theta shows that these interactions, if present, are very small.

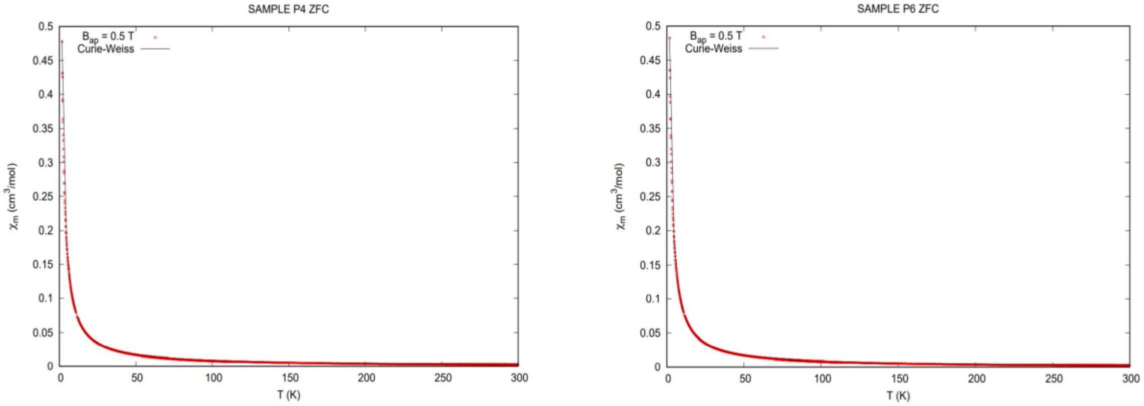

a) **b)**

Figure 3. 20 –Representation of the magnetic molar susceptibility *versus* temperature for **a**) **(4)** and for **b) (6)**.

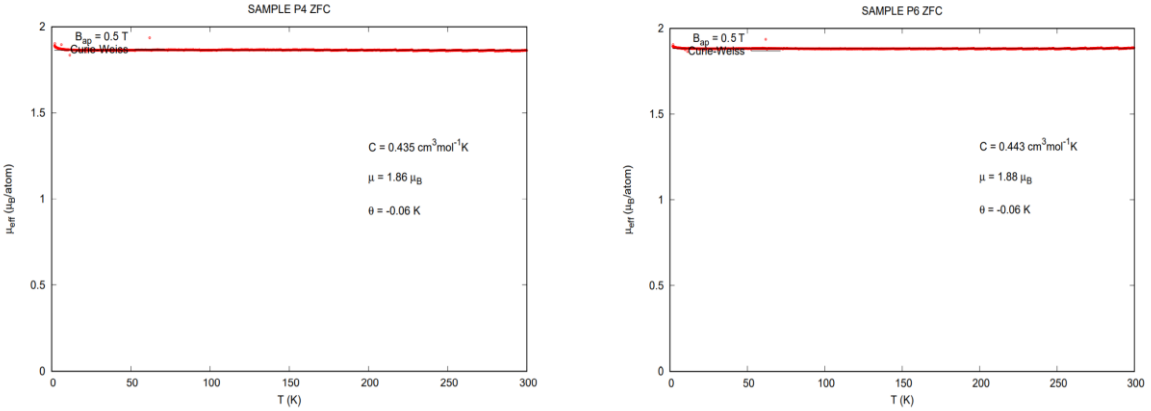

a) **b)**

Figure 3. 21 –Representation of the effective magnetic moment *versus* temperature for **a) (4)** and for **b) (6)**.

For **(7)**, the effective magnetic moment, extracted from the fitted Curie-Weiss law (Figure 3. 22), is also constant within the whole temperature range and the effective magnetic moment of the Cu(II) ions close to the theoretical value. The small negative θ value would signal, once more, very weak residual antiferromagnetic interactions, but the small absolute value of theta shows that these interactions, if present, are very small.

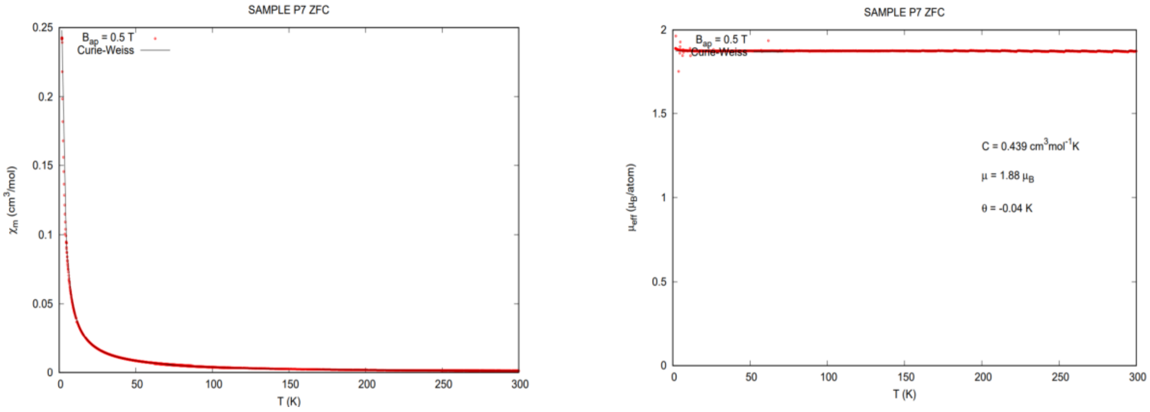

a) **b)**

Figure 3. 22 – a) Representation of the magnetic molar susceptibility *versus* temperature and **b)** representation of the effective magnetic moment *versus* temperature for product 7.

For **(8)**, as it is possible to see in Figure 3. 23, the fitted modified Curie-Weiss law can only correctly describe the magnetic susceptibility for temperatures above ~15 K. The fit gives a positive value for the Weiss constant (+3.45 K), being indicative of ferromagnetic interactions. This is also clearly shown in the $\chi_M T$ vs T plot, which features an upturn at low temperature (see Figure S. 15). In the high temperature range, the effective magnetic moment is constant and close to the theoretical value. The observed downturn at low-temperatures signals the region where the modified Curie-Weiss law no longer fits the data – this is expected for temperatures near and below θ, particularly for those cases, like the present one, where the susceptibility does not diverge at finite temperature, as no long-range ferromagnetic order occurs since the exchange interaction is too week.

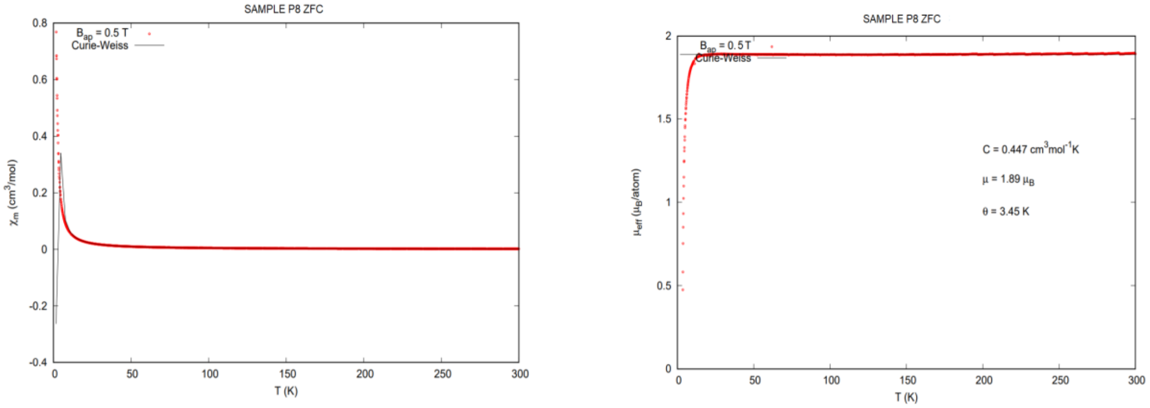

a) **b)**

Figure 3. 23 – a) Representation of the magnetic molar susceptibility *versus* temperature and **b)** representation of the effective magnetic moment *versus* temperature for product 8.

The magnetic hysteresis cycle (between -9 and 9 T) of **(2)**, **(4)**, **(6)**, **(7)** and **(8)** was also measured and Figure 3. 24 displays magnetization isotherms between 0 and 9 T of the powder samples of these products. The graphs have the usual shape of paramagnets, converging to the expected value of Cu(II) moment (slightly above 1 Bohr magnet) under intense magnetic fields and very low temperature. However, the high saturation magnetization of product 8 suggests, once more, its soft ferromagnetic behavior.

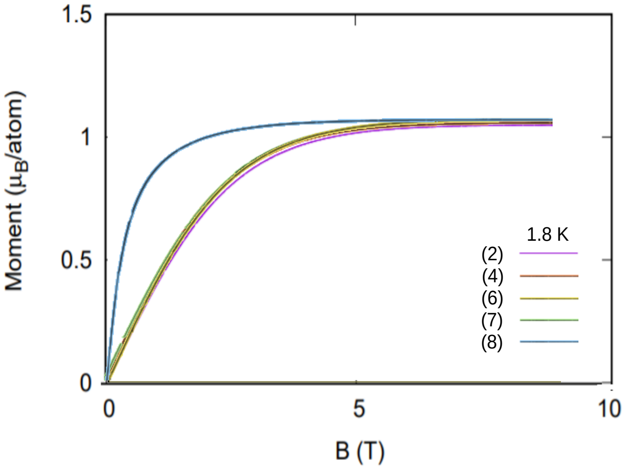

Figure 3. 24 – Isothermal magnetization (M) curves for products 2, 4, 6, 7 and 8.

3.4. Antimicrobial studies

Over the years, it has been shown that copper ions, especially copper(II) ions, have a toxic effect on microbes, including yeast, bacteria and viruses.[149] Although the mechanisms by which copper(II) destroys the microbes are not completely understand yet, a lot of work has been done to understand the broad spectrum efficacy of this metal ion.[26] The entry of these ions into the microorganisms, by interaction with lipids and consequent peroxidation of these molecules (*i.e.* disruption of the cell membrane), may cause leakage of essential solutes and, therefore, cell death.[26] Additionally, complexation may increase the lipophilic character of coordination compounds and enhance their ability to cross the cell membrane of microorganisms. The respiration cell process, as well as the synthesis of proteins by the microbes may, in turn, be compromised, hindering further growth and proliferation of the microorganisms (as previously discussed).

Products 1, 2, 3, 4, 6, 7 and 8 were screened for their antifungal activity against *C. albicans*, *C. tropicalis*, *T. mentagrophytes*, *M. gypseum* and *E. floccosum* and for their antibacterial effect against *E. coli* and *S. aureus*. The antimicrobial activities of the metal complexes were quantified by the determination of their MICs and MLCs, in order to determine and correlate the fungicidal/bactericidal and fungistatic/bacteriostatic effects of the tested compounds, respectively.[150] The *in vitro* antifungal and antibacterial susceptibility examinations of the tested products were carried out at different concentrations, between 4 µg mL^{-1} and 128 µg mL^{-1}. The results were from three or more independent experiments performed in duplicate. When different MIC/MLC values were obtained, a range of values was presented.

Among the eight microorganisms tested in this study, *T. mentagrophytes*, *M. gypseum* and *E. floccosum* were sensitive to the seven metal complexes. In fact, all of the metal complexes proved to have a significant inhibitory efficacy against the dermatophyte strains when compared to the standard drug (Fluconazole), with MIC/MLC values listed in Table 3. 14. Products 3, 7 and 8 stand out for their highest antifungal activities against *T. mentagrophytes* with MIC and MLC values between 8−16 µg mL^{-1}. Against *M. gypseum*, all the metal complexes showed a very good fungicidal and fungistatic effect. In particular product 8 is highlighted for its MIC and MLC values of 16 µg mL^{-1}, when Fluconazole has a MIC value of 128 µg mL^{-1}. Finally, all the coordination compounds displayed, once more, a better inhibitory effect against *E. floccosum*. In particular, products 3, 6, 7 and 8 showed the highest inhibitory effects against this fungal strain, with MIC and MLC values ranging from 8 and 16 µg mL^{-1}. These results allow the conclusion that product 8 is the most effective compound against dermatophyte. Looking to the crystal structure of this compound, we see that it has three azide ligands coordinated to one central metal atom (see Figure 3. 9b), suggesting that if the number of coordinated azide ligands increase in relation to Cu(II) ions, the antifungal properties are better. Interestingly, comparing products 4 and 6, which are structurally very similar (as previously discussed in Section 3.2), it is possible to verify that **(6)** shows a slightly superior antifungal activity against *E. floccosum* comparing to **(4)**. This suggests that the presence of azide ligands (instead of a chlorine) influences the metal complex’s ability of interacting and destroying the fungi cell membrane. It has also been suggested that the ions that are outside the coordination sphere (*i.e.* the counterions) may impart great effect on the inhibition of antimicrobial activities,[151,152] as it can be observed for product 7. This coordination compound, that has two uncoordinated azides in its crystal structure (see Figure 3. 7), proved to have an important role in the improvement of the biological activity against dermatophytes. Despite the good values of the tested metal complexes against dermatophytes, the yeasts (*C. albicans* and *C. tropicalis*) and the bacteria (*E. coli* and *S. aureus*) strains were not sensitive to all the products in the tested concentrations.

Table 3. 14 - Antimicrobial activity of products 1, 2, 3, 4, 6, 7 and 8 against dermatophyte strains.

	Product 1		**Product 2**		**Product 3**		**Product 4**		**Product 6**		**Product 7**		**Product 8**		**Fluconazole**	
	MIC[a)]	MLC[a)]	MIC[a)]	MLC[a)]	MIC[a)]	MLC[a)]	MIC[a)]	MLC[a)]	MIC[a)]	MLC[a)]	MIC[a)]	MLC[a)]	MIC[a)]	MLC[a)]	MIC[a)]	MLC[a)]
Trichophyton mentagrophytes	16	16	16	16	8	8	16	16	16	16	8-16	8-16	8	8	16-32	32-64
Microsporum gypseum	32	32	32	32	32	32	32	32	32	32	32	32	16	16	128	>128
Epidermophyton floccosum	16	16	16	16	8	8	16	16	8-16	8-16	8	8	8	8	16	16

a) MICs and MLCs were determined by a macrodilution method and expressed in µg mL^{-1} (*w/v*).

Conclusions and future perspectives

In the present work, eight different metal complexes were synthetized: $\{[Cu(L{-}arg)_2](NO_3)_2{\bullet}3H_2O\}_n$ **(1)**, $[Cu(L{-}arg)_2(SCN)_2]{\bullet}2H_2O$ **(2)**, $[Cu(L{-}arg)(SCN)_2]$ **(3)**, $[Cu(L{-}arg)_2(N_3)_2][Cu(L{-}arg)_2Cl](N_3){\bullet}7H_2O$ **(4)**, $\{[Cu_2(L{-}arg)_2(N_3)_2(\mu{-}1,3{-}N_3)(\mu{-}1,1{-}N_3)][Cu(L{-}arg)(N_3)(\mu{-}1,1{-}N_3)]{\bullet}3H_2O\}_n$ **(5)**, $[Cu(L{-}arg)_2(N_3)_2][Cu(L{-}arg)_2(N_3)](N_3){\bullet}6H_2O$ **(6)**, $[Cu(L{-}arg)_2(H_2O)_2](N_3)_2$ **(7)** and $\{[Cu(L{-}arg)(N_3)(\mu{-}1,3{-}N_3)]\}_n$ **(8)**. The metal complexes were obtained by different stoichiometric combinations of several aqueous mixtures of copper(II) salts, *L*−arginine and/or KSCN/NaN_3 salts. The synthesis of product 1 was independent on the reagents molar stoichiometry used, but sensitive to the use of different copper(II) salts. The synthesis of product 2 was equally independent on the reagents molar stoichiometry and on the use of different copper(II) salts. The coordination of products 3-8 were dependent on both of these factors. The presence of the different SCN^- or N_3^- ions affected the synthesis (and the overall geometry) of all the products except for **(1)**.

The crystal structure of products 1 and 3 was already described in literature. However, in this work, a new synthetic method for both compounds is presented. The single-crystal X-ray analysis results show that the unit cell of **(1)** consists of one *cis*−$[Cu(L{-}arg)_2]^{2+}$ cation with a four-coordinated copper(II) center. Due to its structural similarity to the Netropsin antibiotic, the antimicrobial activities were evaluated against fungi (particularly, against yeasts and dermatophytes) and bacteria, but this coordination compound only proved to have antifungal activity against the dermatophytes. The crystal structure of **(3)**, similarly to **(1)** has a four-coordinated metal center. Regarding to its biological activity, product 3 showed to have one of the best antifungal effects against dermatophyte strains by presenting lower MIC and MLC values comparing to Fluconazole standard drug reference. Products 2 and 7 exhibit a *trans*−distorted octahedral geometry with a basal environment of N_2O_2 atoms from *L*−arginine. However, for **(2)**, the elongated axial vertexes of the octahedron are occupied by two distinct isothiocyanate groups (N−coordinated), while for **(7)** the apexes of the octahedron are occupied by two water molecules. The unit cell of **(7)** is composed by the $[Cu(L{-}arg)_2(H_2O)_2]^{2+}$ complex cation with two azide behaving as counterions to attain the positive charge of the coordination compound. The presence of these counterions seemed to be relevant in the evaluation of the antimicrobial activity, since product 7, just like product 3, had one of the best antifungal effects against dermatophytes. Products 4 and 6 are structurally very similar to each other. Both coordination compounds crystallize in the monoclinic crystal system with $P2_1$ space group. Their unit cells accommodate two different metal complexes, one with a five-coordinated metal center and other with a six-coordinated one. In both compounds, the azide ion act either as chelating or as bridging ligand. The value of the τ parameter (0.0383 for **(4)** and 0.0943 for **(6)**) confirms a square pyramidal geometry around Cu(II) ions in these products. Interestingly, regarding to their biological activities, it is possible to verify that **(6)** shows a slightly superior antifungal activity against *E. floccosum* comparing to **(4)**. This suggests that the presence of azide ligands (instead of a chlorine) influences the metal complex's ability of interacting and destroying the fungi cell membrane. Product 5, similarly to products 4 and 6, presents two different metal complexes in the unit cell, but here all of the copper(II) centers are five-coordinated. The azide ion plays, once more, either as a chelating or bridging ligand. However, in this case, two types of bridging are observed: an end-to-end bridge and a single-atom bridge. This end-to-end bridge was also observed for **(8)**, where its crystal structure revealed a five-coordinated metal complex with a coordination sphere described as a square pyramid (τ = 0.0453). Product 8 was the most interesting synthetized coordination compound, since the magnetic properties of its greenish single-crystals indicated a positive value for the Weiss constant (being indicative of weak ferromagnetic interactions). Additionally, product 8 was the most effective compound against *Trichophyton mentagrophytes*, *Microsporum gypseum* and *Epidermophyton floccosum* strains, suggesting that the higher the number of coordinated azides comparing to the number of Cu(II) ions, the strongest the antifungal effects are.

The detailed characterization of metal complexes (by the means of X-ray crystallography, infrared spectroscopy or magnometry) is essential to establish a relationship between their structure and activity. In addition, the copper(II):*L*−arginine complexes proved to have strong antifungal effects against all the dermatophyte strains, so other amino acids should be consider in the preparation of others coordination compounds. In this line of reasoning, a comparative study between different [copper(II):amino acids] complexes could be done to understand how different biomolecules structurally and biologically affect these type of coordination compounds. Additionally, further biological studies such as cytotoxic studies or DNA biding could be carried out in order to understand the potential of copper-based metallodrugs as valid alternatives for some pathologies.

References

1. Hartshorn, R. M., Hellwich, K. H., Yerin, A., Damhus, T., Hutton, A. T. *Pure Appl. Chem.* **2015**, 87, 1039–1049.
2. Chen, J., Fukuzumi, K., Ip, B., Florence, Cid, Andres, A.P. *Int. J. Pharm. Biol. Chem. Sci.* **2014**, 3, 36–45.
3. Castillo-Blum, S. E., Barba-Behrens, N. *Coord. Chem. Rev.* **2000**, 196, 3–30.
4. Soldatović, T. *Correlation between HSAB Principle and Substitution Reactions in Bioinorganic Reactions*. In Substitution Reaction, IntechOpen. **2020**.
5. McNaught, A.D., Wilkinson, A. IUPAC. *Compendium of Chemical Terminology*, 2nd Edition (The 'Gold Book'). Blackwell Sci. Publ. Oxford. **1997**.
6. Pearson, R. G. *Coord. Chem. Rev.* **1990**, 100, 403–425.
7. Pearson, R. G. *J. Am. Chem. Soc.* **1963**, 85, 3533–3539.
8. Sodhi, R. K., Paul, S. *Canc Ther. Oncol Int J.* **2019**, 14.
9. Bagchi, A., Mukhergee, P., Raha, A. *Int. J. Recent Adv. Pharm. Res.* **2015**, 5(3), 171-180.
10. Dursch, T. J. *Trends Chem.* **2019**, 1, 455–456.
11. Turel, I. *Molecules* **2015**, 20, 7951–7956.
12. Housecroft, C. E., Thomas, C. M., Lim, M. H. *Dalt. Trans.* **2019**, 48, 9405–9407.
13. LibreTexts. *Werner's Theory of Coordination Compounds*. **2019**.
14. Blacque, O., Berke, H. *Educ. Quim.* **2015**, 26, 330–345.
15. Constable, E. C., Housecroft, C. E. *Chem. Soc. Rev.* **2013**, 42, 1429–1439.
16. Bowman-James, K. *Acc. Chem. Res.* **2005**, 38, 671–678.
17. Bhatt, V., Ram, S. *Chem. Sci. Rev. Lett.* **2015**, 4, 414–428.
18. Remko, M., Fitz, D., Rode, B. M. *Structure* **2008**, 7652–7661.
19. Saczewski, F., Balewski, Ł. *Expert Opin. Ther. Pat.* **2009**, 19, 1417–1448.
20. Xu, B., Jacobs, M. I., Kostko, O., Ahmed, M. *ChemPhysChem.* **2017**, 18, 1503–1506.
21. Shimazaki, Y., Takani, M. & Yamauchi, O. *Dalt. Trans.* **2009**, 7854–7869.

22. Hu, R., Yu, Q., Liang, F., Ma, L., Chen, X., Zhang, M., Liang, H., Yu, K. *J. Coord. Chem.* **2008**, 61, 1265–1271.

23. Wojciechowska, A., Kochel, A., Zierkiewicz, W. *J. Coord. Chem.* **2016**, 69, 886–900.

24. Patra, A. K., Bhowmick, T., Ramakumar, S., Chakravarty, A. R. *Inorg. Chem.* **2007**, 46, 9030-9032.

25. Wojciechowska, A., Gągor, A., Zierkiewicz, W., Jarząb, A., Dylong, A., Duczmal, M. *RSC Adv.* **2015**, 5, 36295–36306.

26. Wojciechowska, A., Szuster-Ciesielska, A., Sztandera, M., Bregier-Jarzębowska, R., Jarząb, A., Rojek, T., Komarnicka, U., Bojarska-Junak, A., Jezierska, J. *Appl. Organomet. Chem.* **2020**, 34, 0–16.

27. Eljazouli, H., Laabd, M., Elamine, M., Albourine, A. J. *Mater. Environ. Sci.* **2017**, 8, 2469-2473.

28. Li, D., Yang, C., Liu, P., Wang, Y., Sun, Y. *Indian J. Microbiol.* **2016**, 56, 214–218.

29. Haas, K. L., Franz, K. J. *Chem. Rev.* **2009**, 109, 4921–4960.

30. Cánovas, D., Marcos, J. F., Marcos, A. T., Strauss, J. *Curr. Genet.* **2016**, 62, 513–518.

31. Schairer, D. O., Chouake, J. S., Nosanchuk, J. D., Friedman, A. J. *Virulence* **2012**, 3, 271–279.

32. Missall, T. A., Lodge, J. K., McEwen, J. E. *Eukaryot. Cell.* **2004**, 3, 835–846.

33. Fang, F. C. *J. Clin. Invest.* **1997**, 99, 2818–2825.

34. Sreesha, S. *Transition Metal Complexes of Schiff Bases with Azide and Thiocyanate as Coligands: Spectral and Structural Investigations (*Doctoral dissertation). Cochin University of Science And Technology, India. **2008**.

35. Kong, L., Li, W-J., Li, X-L., Geng, W-Q., Hao, F-Y., Wu, J-Y., Zhou, H-P., Yang, J-X., Tian, Y-P., Jin, B-K. *Polyhedron.* **2010**, 29, 1575–1582.

36. Shurdha, E., Moore, C., Rheingold, A., Lapidus, S., Stephens, P., Arif, A., Miller, J. *Inorg. Chem.* **2013**, 52, 10583–10594.

37. Hazari, A., Das, L. K., Bauzá, A., Frontera, A., Ghosh, A. *Dalt. Trans.* **2014**, 43, 8007-8015.

38. Xue, L. W., Zhao, G. Q., Han, Y. J., Feng, Y. X. *Synth. React. Inorg. Met. Nano-Metal Chem.* **2011**, 41, 141–146.

39. Shaabani, B., Khandar, A. A., Dusek, M., Pojarova, M., Mahmoudi, F., Feher, A., Kajňaková, M. *J. Coord. Chem.* **2013**, 66, 748–762.

40. Berger, A. *Crystal Field Theory and d-block Metal Chemistry*. **2019**.

41. Keppler, H. *Crystal field theory*. *Encyclopedia of Earth Sciences Series.* **2018**.

42. Libre Texts. *Crystal Field Theory : Optical and Magnetic Properties*. **2020**.

43. Wang, D. *Colors of Coordination Complexes Colors of Coordination Complexes: Crystal Field Splitting*. **2020**.

44. Dalal, M. *A Textbook of Inorganic Chemistry* (Chapter 9). 1st Edition. Dalal Institute, **1869**.

45. Bennett, D., Larsen, D., Davis, U. C. *Susceptibility of Paramagnets*. **2016**.

46. Weiss, G., Carver, P. L. *Clin. Microbiol. Infect.* **2018**, 24, 16–23.

47. Ballou, E. R., Wilson, D. *Curr. Opin. Microbiol.* **2016**, 32, 128–134.

48. Trevors, J. T., Oddie, K. M., Belliveau, B. H. *FEMS Microbiol. Lett.* **1985**, 32, 39–54.

49. Pitt, D., Ugalde, U. O. *Plant. Cell Environ.* **1984**, **7**, 467–475.

50. Jones, E. B. G., Jennings, D. H. *New Phytol*. **1965**, 64, 86–100.

51. Groisman, E. A., Hollands, K., Kriner, M. A., Lee, E-J., Park, S-Y., Pontes, M. H. *Annu. Rev. Genet.* **2013**, 47, 625–646.

52. Gupta, S. P. *MOJ Bioorganic Org. Chem.* **2018**, 2, 221–224.

53. Bailão, E. F. L. C., Parente, A. F. A., Parente, J. A. Silva-Bailão, M. G., Castro, K. P., Kmetzsch, L., Staats, C. C., Schrank, A., Vainstein, M. H., Borges, C. L., Bailão, A. M., Soares, C. M. A. *Curr. Fungal Infect. Rep.* **2012**, 6, 257–266.

54. Ladomersky, E., Petris, M. J. *Metallomics.* **2015**, **7**, 957–964.

55. Ou, Z. B., Lu, Y. H., Lu, Y. M., Chen, S., Xiong, Y. H., Zhou, X. H., Mao, Z. W., Le, X. Y. *J. Coord. Chem.* **2013**, 66, 2152–2165.

56. Raman, N., Joseph, J., Velan, A. S. K., Pothiraj, C. *Mycobiology.* **2006**, 34, 214.

57. Bhasin, H., Bhatt, V. *J. Chem. Chem. Sci.* **2018**, 8, 595–605.

58. Gopalakrishnan, S., Joseph, J. *Mycobiology*. **2009**, **37**, 141.

59. Chohan, Z. H., Pervez, H., Khan, K. M., Rauf, A., Maharvi, G. M., Supuran, C. T. *J. Enzyme Inhib. Med. Chem.* **2004**, 19, 85–90.

60. Iqbal, M. S., Khurshid, S. J., Iqbal, M. Z. A. *J. Pak. Med. Assoc.* **1990**, 40, 221–222.

61. Ahmad, S., Yousaf, A., Tahir, M. N., Isab, A. A., Monim-ul-Mehboob, M., Linert, W., Saleem, M. *J. Struct. Chem.* **2015**, 56, 1653–1657.

62. Hemissi, H., Nasri, A., Rzaigui, M. *J. Mol. Struct.* **2019**, 1186, 307–316.

63. Abdel-Mottaleb, M. S. A., Ismail, E. H. *J. Chem.* **2019**.

64. Takayama, A., Yoshikawa, R., Iyoku, S., Kasuga, N. C., Nomiya, K. *Polyhedron.* **2013**, 52, 844–847.

65. Jockusch, R. A., Price, W. D., Williams, E. R. *J. Phys. Chem. A* **1999**, 103, 9266–9274.

66. Bathula, S., Kotra, K. K. *Int. J. Adv. Eng. Res. Sci.* **2019**, 6, 306–314.

67. Antonilli, M., Bottari, E., Festa, M. R., Gentile, L. *Chem. Speciat. Bioavailab.* **2009**, 21, 33-40.

68. Selvaganapathy, M., Raman, N. *J. Chem. Biol. Ther.* **2016**, 01, 1–17.

69. Ndagi, U., Mhlongo, N., Soliman, M. E. *Drug Des. Devel. Ther.* **2017**, 11, 599–616.

70. Hossain, M. S. *Am. J. Heterocycl. Chem.* **2018**, 4, 1.

71. Pathirana, R. U., McCall, A. D., Norris, H. L., Edgerton, M. *Front. Microbiol.* **2019**, 10, 1–12.

72. Kothavade, R. J., Kura, M. M., Valand, A. G., Panthaki, M. H. *J. Med. Microbiol.* **2010**, 59, 873–880.

73. Expósito, C. *Arginine- based surfactants and Chemo-enzymatic synthesis of novel Amphiphiles Studies on antimicrobial activity of arginine-based surfactants and chemo-enzymatic synthesis of novel amphiphiles based on L -arginine and D -fagomine* (Doctoral dissertation). Universitat Autònoma de Barcelona, Spain. **2006**.

74. Silhavy, T. J., Kahne, D., Walker, S. *Cold Spring Harb Perspect Biol.* **2010**, 2, 1–16.

75. Garber, G. *Drugs* **2001**, 61, 1–12.

76. Singh, A., Verma, R., Murari, A., Agrawal, A. *J. Oral Maxillofac. Pathol.* **2014**, 18, 81-85.

77. K. Mazu, T., A. Bricker, B., Flores-Rozas, H., Y. Ablordeppey, S. *Mini-Reviews in Medicinal Chemistry*. **2016**, 16.

78. Garcia-Rubio, R., de Oliveira, H. C., Rivera, J., Trevijano-Contador, N. *Front. Microbiol.* **2020**, 10, 1–13.

79. Gow, N. A. R., Latge, J., Munro, C. A. *The Fungal Kingdom.* **2017**, 267–292.

80. Silver, L. L. *Cold Spring Harb. Perspect. Med.* **2016**, 6, 1–7.

81. Coates, A., Hu, Y., Bax, R., Page, C. *Nat. Rev. Drug Discov.* **2002**, 1, 895–910.

82. Turecka, K., Chylewska, A., Kawiak, A., Waleron, K. F. *Front. Microbiol.* **2018**, 9, 1-14.

83. Lopes, G., Pinto, E., Salgueiro, L. *Mycopathologia.* **2017**, 182, 143–167.

84. Konaklieva, M. I. *Antibiotics* **2014**, 3, 128–142.

85. Castillo, K. F., Bello-Vieda, N. J., Nuñez-Dallos, N. G., Pastrana, H. F., Celis, A. M., Restrepo, S., Hurtado, J. J., Ávila, A. G. *J. Braz. Chem. Soc.* **2016**, 27, 2334–2347.

86. Reygaert, W. C. *AIMS Microbiol.* **2018**, 4, 482–501.

87. Zuzarte, M., Gonçalves, M. J., Canhoto, J., Salgueiro, L. *Sci. against Microb. Pathog. Commun. Curr. Res. Technol. Adv.* **2011**, 2, 1167-1178.

88. Anacona, J. R., Mago, K., Camus, J. *Appl. Organomet. Chem.* **2018**, 32, 1–9.

89. Raman, N., Kulandaisamy, A., Thangaraja, C., Manisankar, P., Viswanathan, S., Vedhi, C. *Transit. Met. Chem.* **2004**, 29, 129–135.

90. Al-Amiery, A. A., Kadhum, A. A. H., Mohamad, A. B. *Bioinorg. Chem. Appl.* **2012**.

91. Panchal, P. K., Pansuriya, P. B., Patel, M. N. *J. Enzyme Inhib. Med. Chem.* **2006**, 21, 453–458.

92. Raman, N., Kulandaisamy, A., Shunmugasundaram, A., Jeyasubramanian, K. *Transit. Met. Chem.* **2001**, 26, 131–135.

93. Raman, N., Sobha, S., Thamaraichelvan, A. *Spectrochim. Acta - Part A Mol. Biomol.*

Spectrosc. **2011**, 78, 888–898.

94. Shaabani, B., Khandar, A. A., Mobaiyen, H., Ramazani, N., Balula, S. S., Cunha-Silva, L. *Polyhedron.* **2014**, 80, 166–172.
95. Hartinger, C. *Angew. Chemie Int. Ed.* **2015**, 54, 2324–2324.
96. Schwietert, C. W., McCue, J. P. *Coord. Chem. Rev.* **1999**, 184, 67–89.
97. Fairlie, D. P., Jackson, W. G., Skelton, B. W., Wen, H., White, A. H., Wickramasinghe, W. A., Woon, T. C., Taube, H. *Inorg. Chem.* **1997**, 36, 1020–1028.
98. Pantos, A., Tsogas, I., Paleos, C. M. *Biochim. Biophys. Acta - Biomembr.* **2008**, 1778, 811-823.
99. CrysAlis CCD and CrysAlis PRO 1.171.38.43. *Rigaku Oxford Diffr.* **2015**, 44, 1–53.
100. Sheldrick, G. M. *Acta Cryst., C71, 3.* **2015**, 71, 3–8.
101. Khan, M. I., Hussain, A., Khan, M. A., Gul, S., Iqbal, M., Khuda, F. *Inorg. Chem. Commun.* **2013**, 35, 104–109.
102. Clinical and Laboratory Standarts Institute (CLSI). *Approved Standard-Third Edition M27-A3 and Third Informational Supplement M27-S3.* Wayne, PA, USA. **2008**, 28, 0-13.
103. Clinical and Laboratory Standards Institute (CLSI). *Approved Standard-Second edition M38-A2*. Wayne, PA, USA. **2008**, 28, 0–13.
104. Clinical and Laboratory Standarts Institute (CLSI). *Approved Standard-Ninth Edition M07-A9*. Wayne, PA, USA. **2012**, 32.
105. Masuda, H., Odani, A., Yamazaki, T., Yajima, T., Yamauchi, O. *Inorg. Chem.* **1993**, 32, 1111-1118.
106. Fan, G., Ling-Juan, D., Zhan-Ying, M., Xiao-Bo, L., Yin-Li, Z., Jia-Juan, S. *Jiegou Huaxue* **2016**, 35, 100–106.
107. Wojciechowska, A., Janczak, J., Rojek, T., Gorzsas, A., Malik-Gajewska, M., Duczmal, M. *J. Coord. Chem.* **2019**, 72, 1358–1377.
108. Sahin, Z. S., Öztürk, Z., Yurdakul, O., Köse, D. A. *Hittite J. Sci. Eng.* **2016**, 3, 41–49.
109. Santana, R. C., Carvalho, J. F., Vencato, I., Napolitano, H. B., Bortoluzzi, A. J., Barberis, G. E., Rapp, R. E., Passeggi, M. C. G., Calvo, R. *Polyhedron.* **2007**, 26, 5001–5008.

110. Wojciechowska, A., Kochel, A., Duczmal, M. *Mater. Chem. Phys.* **2016**, 182, 472–480.
111. Yajima, T., Giuseppe, M., Takani, M., Contino, A., Arena, G., Takamido, R., Hanaki, M., Funahashi, Y., Odani, A., Yamauchi, O. *Chem. - A Eur. J.* **2003**, 9, 3341–3352.
112. Breneman, G. L., Parker, O. J. *Polyhedron.* **1993**, 12, 891–895.
113. Tsague Chimaine, F., Yufanyi, D. M., Colette Benedicta Yuoh, A., Eni, D. B., Agwara, M. O. *Cogent Chem.* **2016**, 2, 1–14.
114. Machura, B., Świtlicka, A., Palion, J., Kruszynski, R. *Struct. Chem.* **2013**, 24, 89–96.
115. Świtlicka, A. Czerwińska, K., Machura, B., Penkala, M., Bieńko, A., Bieńko, D., Zierkiewicz, W. *CrystEngComm.* **2016**, 18, 9042–9055.
116. Kumar, S. B., Mahendrasinh, Z., Ankita, S., Mohammedayaz, R., Pragna, P., Suresh, E. *Polyhedron.* **2012**, 36, 15–20.
117. Song, Y., Xu, Z., Sun, Q., Su, B., Gao, Q., Liu, H., Zhao, J. *J. Coord. Chem.* **2007**, 60, 2351-2359.
118. Luo, J., Zhou, X-G., Gao, S., Weng, L-H., Shao, Z-H., Zhang, C-M., Li, Y-R., Cai, R-F. *Polyhedron.* **2004**, 23, 1243–1248.
119. Rahaman, S. H., Fun, H. K., Ghosh, B. K. A. *Polyhedron.* **2005**, 24, 3091–3097.
120. Trans, D., Addison, A. W., Rao, T. N. S. *J. Chem. Soc. Dalt. Trans.* **1984**.
121. Wojciechowska, A., Gągor, A., Jezierska, J., Duczmal, M. *RSC Adv.* **2014**, 4, 63150-63161.
122. Wojciechowska, A., Janczak, J., Zierkiewicz, W., Rytlewski, P. Rojek, T., Duczmal, M. *Mater. Chem. Phys.* **2019**, 228, 272–284.
123. Mauro, A. E., Haddad, P. S., Zorel, H. E., Santos, R. H. A., Ananias, S. R., Martins, F. R., Tarrasqui, L. H. R. *Transit. Met. Chem.* **2004**, 29, 893–899.
124. Goher, M. A. S., Mautner, F. A. *Polyhedron.* **1995**, 14, 1439–1446.
125. Liu, J. J., He, X., Shao, M., Li, M. X. *J. Mol. Struct.* **2009**, 919, 189–195.
126. Fielden, J., Sprott, J., Long, D. L., Kögerler, P., Cronin, L. *Inorg. Chem.* **2006**, 45, 2886-2895.
127. Feng, H., Zhou, x. P., Wu, T., Li, D., Yin, Y. G., Ng, S. W. *Inorganica Chim. Acta.* **2006**,

359, 4027–4035.

128. Das, A., Todorov, I., Dey, S. K., Mitra, S. *Inorganica Chim. Acta.* **2006**, 359, 2041–2046.
129. Drozd, M. *Mater. Sci. Eng. B Solid-State Mater. Adv. Technol.* **2007**, 136, 20–28.
130. Kumar, S., Rai, S. B. *Indian J. Pure Appl. Phys.* **2010**, 48, 251–255.
131. Sheppard, N. *Trans. Faraday Soc.* **1956**, **53**, 589–600.
132. Goebbert, D. J., Garand, E., Wende, T., Bergmann, R., Meijer, G., Asmis, K., Neumark, D. M. *J. Phys. Chem. A.* **2009**, 113, 7584–7592.
133. Jones, L. H. *J. Chem. Phys.* **1956**, 25, 1069–1072.
134. Coates, J. *Encycl. Anal. Chem.* **2004**, 1–23.
135. Barth, A. *Prog. Biophys. Mol. Biol.* **2000**, **74**, 141–173.
136. Mautner, F. A., Louka, F. R., Gallo, A. A., Albering, J. H., Saber, M. R., Burham, N. B., Massoud, S. S. *Transit. Met. Chem.* **2010**, 35, 613–619.
137. Diana, E., Gatterer, K., Kettle, S. F. A. *Phys. Chem. Chem. Phys.* **2016**, 18, 414–425.
138. Lieber, E., Rao, C. N. R., Hoffman, C. W. W., Chao, T. S. I. *Anal. Chem.* **1957**, 29, 916-918.
139. Deacon, G. B., Phillips, R. J. *Coord. Chem. Rev.* **1980**, 33, 227–250.
140. Kabesova, M.;Gazo, J. *Chem. Rev.* **1980**, 34, 41.
141. Toeniskoetter, R. H., Solomon, S. *Inorg. Chem.* **1968**, **7**, 617–620.
142. Ahmed, A., Lal, R. A. *Arab. J. Chem.* **2017**, 10, S901–S908.
143. Tobias, R. S. *J. Chem. Educ.* **1979**, 56, A209.
144. Baranyi, A. D., Makhija, R., Onyszchuk, M. *Can. J. Chem.* **1976**, 54, 1189–1196.
145. Dori, Z., Ziolo, R. F. *Chem. Rev.* **1973**, 73, 247–254.
146. Gaelle, D. S. Y., Agwara, M. O., Yufanyi, D. M., Nenwa, J., Jagan, R. *Inorg. Nano-Metal Chem.* **2017**, 47, 618–625.
147. Gerard, M. F., Aiassa, C., Casado, N. M. C., Santana, R. C., Perec, M., Rapp, R. E., Calvo, R. *J. Phys. Chem. Solids.* **2007**, 68, 1533–1539.

148. Lancashire, R. J. *Magnetic Moments of Transition Metals*. LibreTexts. **2016**.

149. Pires, A. S., Batista, J., Murtinho, D., Nogueira, C., Karamysheva, A., Ramos, M. L., Milne, B. F., Tavares, N. T., Gonçalves, J. Gonçalves, A. C., Abrantes, A. M., Soares, R., Gonçalves, T., Botelho, M. F., Serra, M. E. S. *Appl. Organomet. Chem.* **2020**, 34, 1-18.

150. Palmeira-de-Oliveira, A., Salgueiro, L., Palmeira-de-Oliveira, R., Martinez-de-Oliveira, J., Pina-Vaz, C., queiroz, J. A., Rodrigues, A. G. *Mini-Reviews Med. Chem.* **2009**, 9, 1292–1305.

151. Rehman, S., Ikram, M., Subhan, F., Sinnokrot, M., Khan, W. *Open Chem.* **2019**, 17, 936-942.

152. Mailhot, G., Brand, N., Astruc, M., Bolte, M. *Appl. Organomet. Chem.* **2002**, 16, 17–20.

153. Halcrow, M. A. *Chem. Soc. Rev.* **2013**, 42, 1784-1795.

154. Kurzydłowski, D. *Crystals.* **2018**, 8, 1–13.

Supplementary material

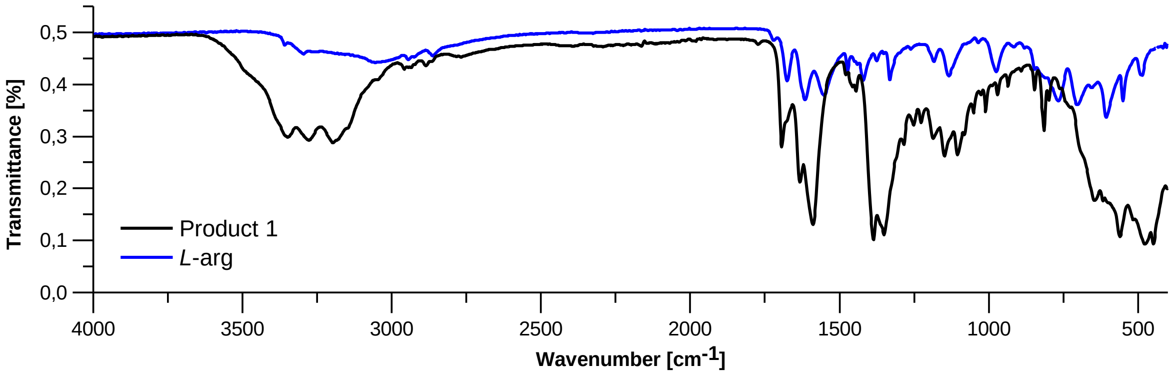

Figure S. 1 – FT-IR spectra of **(1)** and *L*-arg.

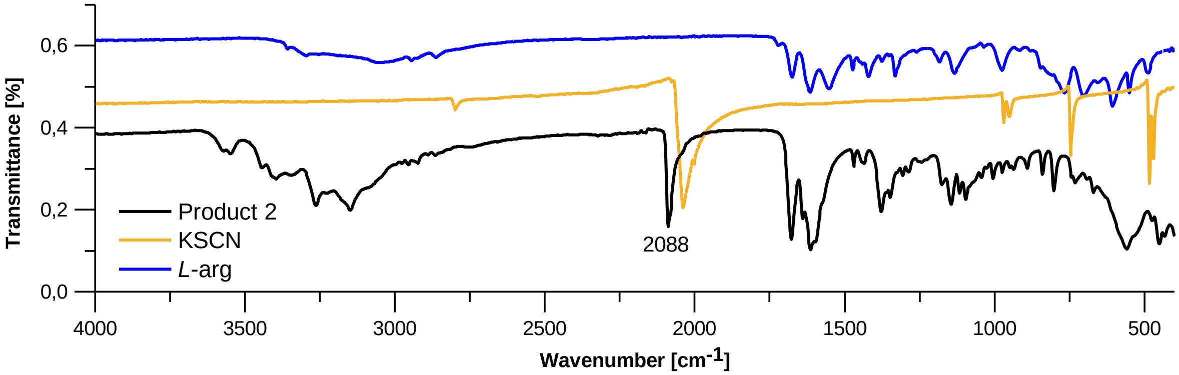

Figure S. 2 – FT-IR spectra of **(2)**, *L*-arg and KSCN.

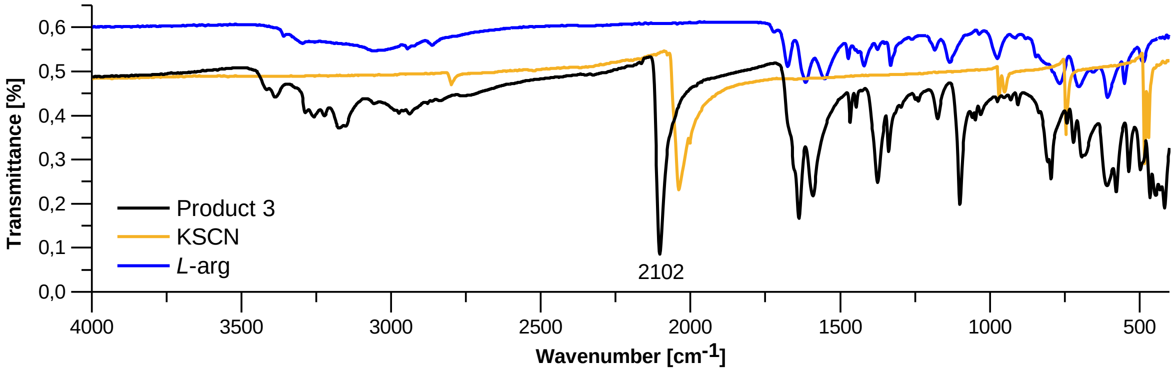

Figure S. 3 – FT-IR spectra of **(3)**, *L*-arg and KSCN.

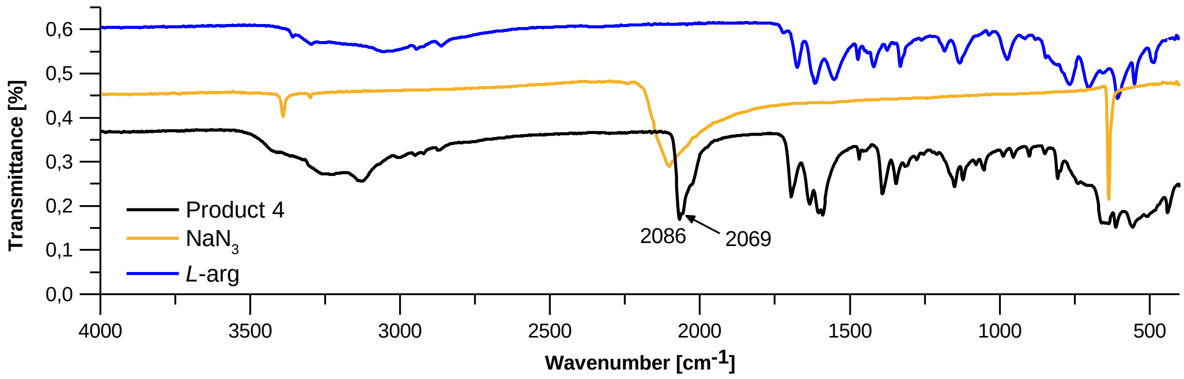

Figure S. 4 – FT-IR spectra of **(2)**, *L*-arg and NaN$_3$.

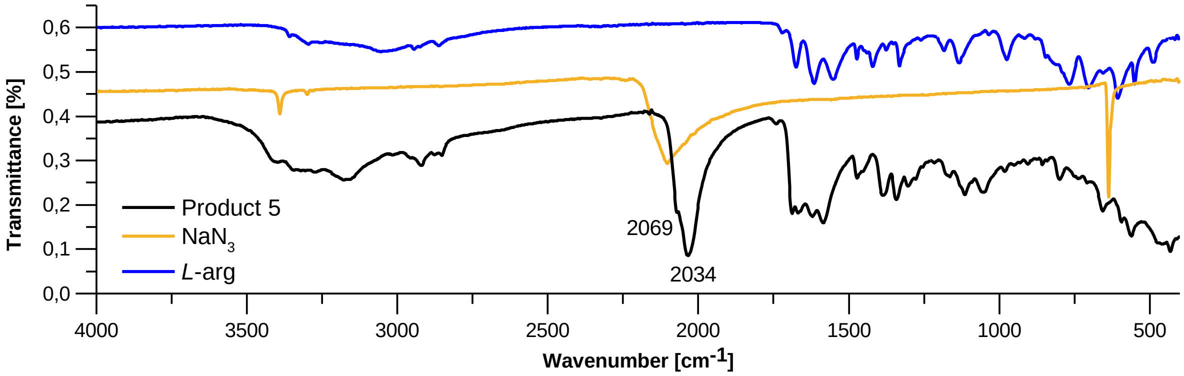

Figure S. 5 – FT-IR spectra of **(5)**, *L*-arg and NaN$_3$.

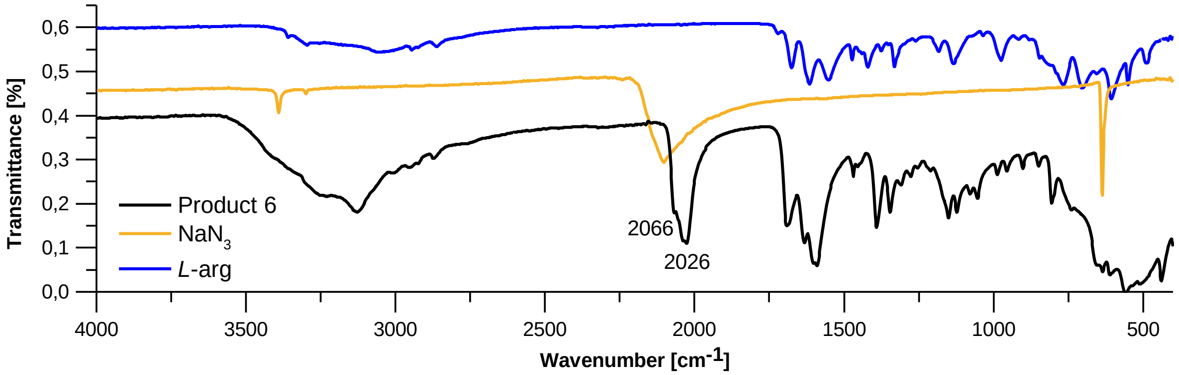

Figure S. 6 – FT-IR spectra of **(6)**, *L*-arg and NaN$_3$.

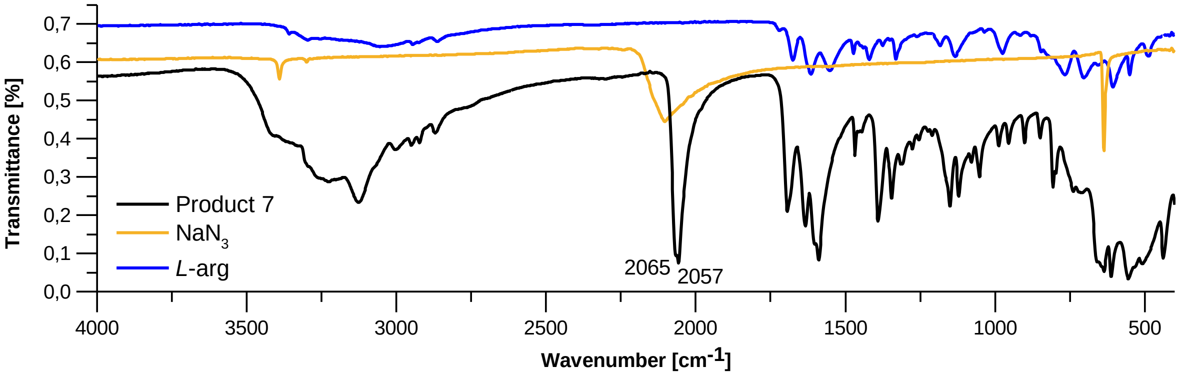

Figure S. 7 – FT-IR spectra of **(7)**, *L*-arg and NaN_3.

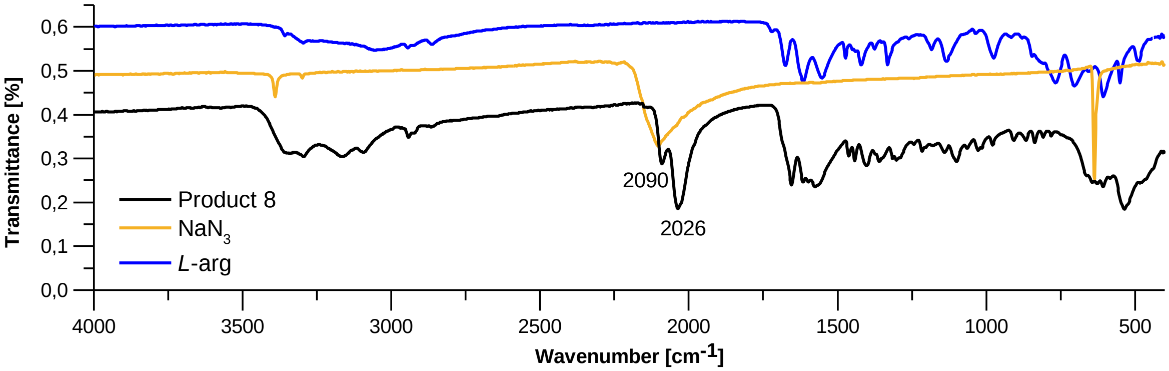

Figure S. 8 – FT-IR spectra of **(8)**, *L*-arg and NaN_3.

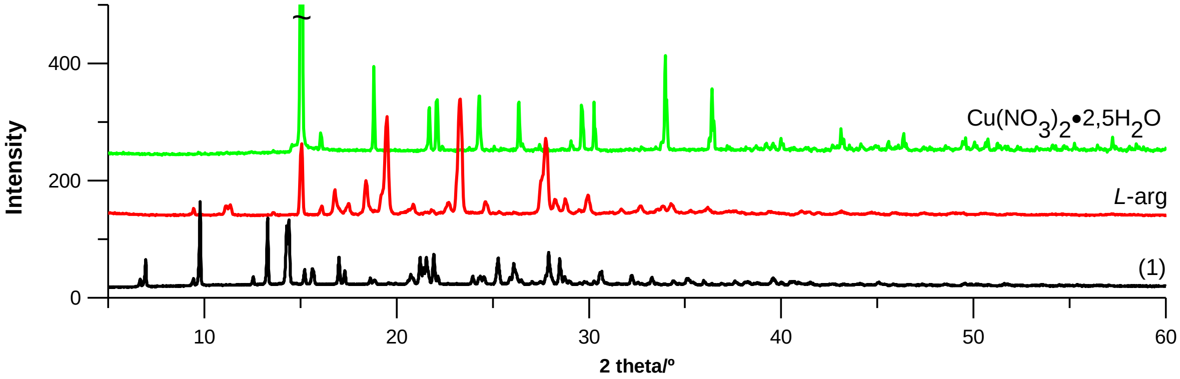

Figure S. 9 – PXRD pattern obtained for product 1 and for the ligands used in its synthesis. The data of **(1)** shows the presence of new peaks when compared to *L*-arg and $Cu(NO_3)_2$•2,5H_2O, indicating the formation of the metal complex. The intensity of the peak marked with a tilde (~) was truncated.

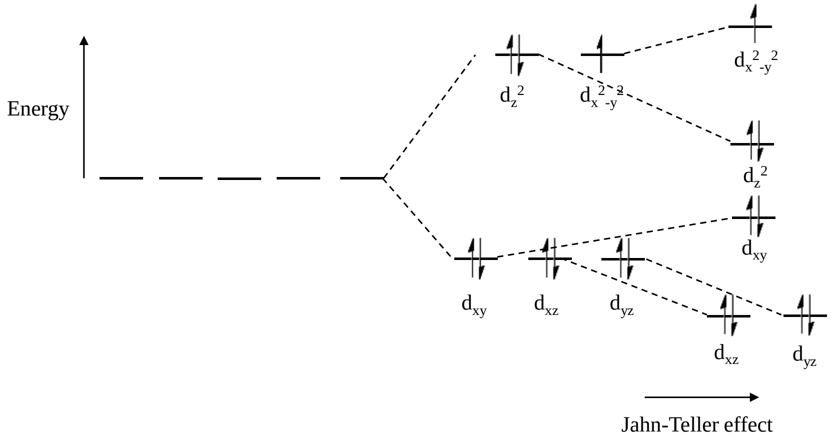

Figure S. 10 – Jahn-Teller distortion observed for copper(II) ions under an octahedral geometry

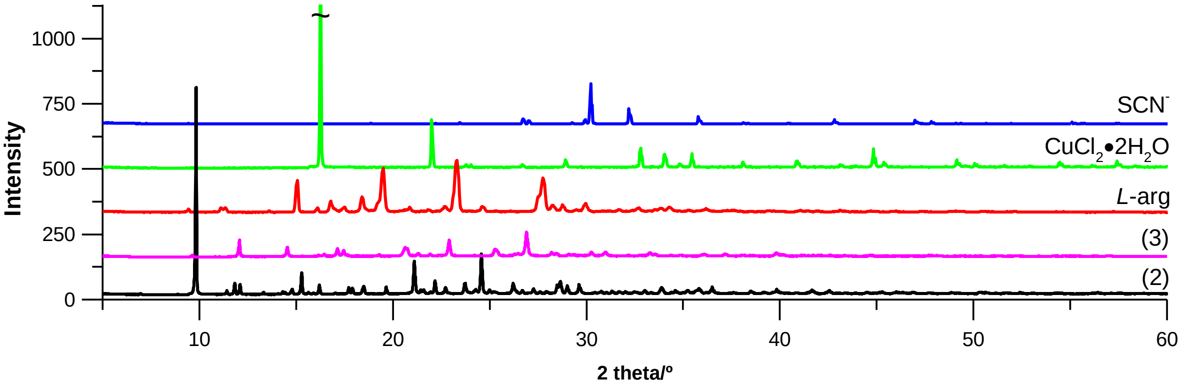

Figure S. 11 – PXRD pattern obtained for products 2 and 3 and for the ligands used in their synthesis. The data of **(2)** and **(3)** show the presence of new peaks when compared to *L*-arg, Cu(Cl$_2$)$_2$•2H$_2$O and SCN$^-$, indicating the formation of the metal complex. The intensity of the peak marked with a tilde (~) was truncated.

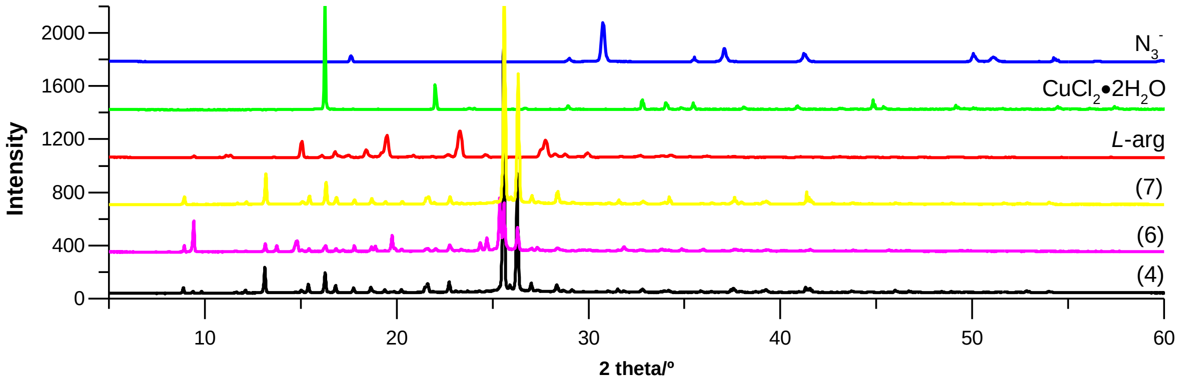

Figure S. 12 – PXRD pattern obtained for products 4, 6 and 7 and for the ligands used in their synthesis. The data of **(4)**, **(6)** and **(7)** show the presence of new peaks when compared to *L*-arg, Cu(Cl$_2$)$_2$•2H$_2$O and N$_3^-$, indicating the formation of the metal complex.

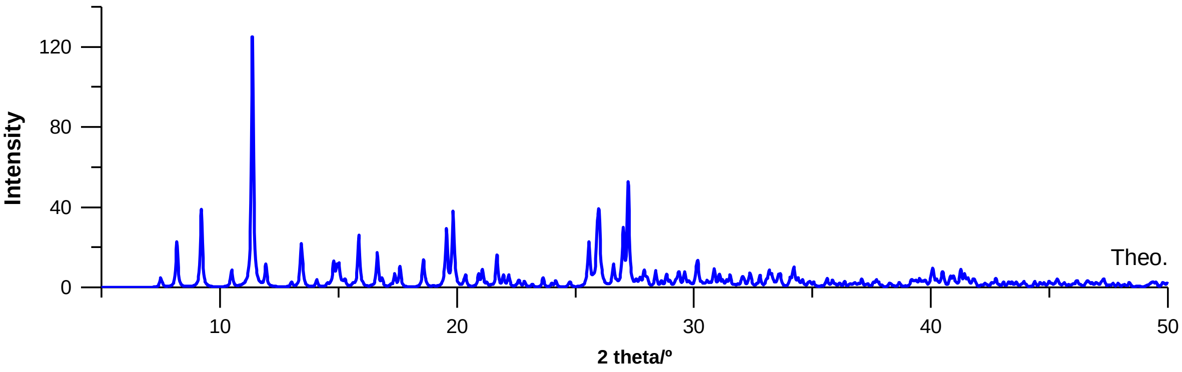

Figure S. 13 – PXRD pattern predicted for product 5 with expected positions and relative intensity of peaks calculated from the crystal structure obtained from the single X-ray diffraction.

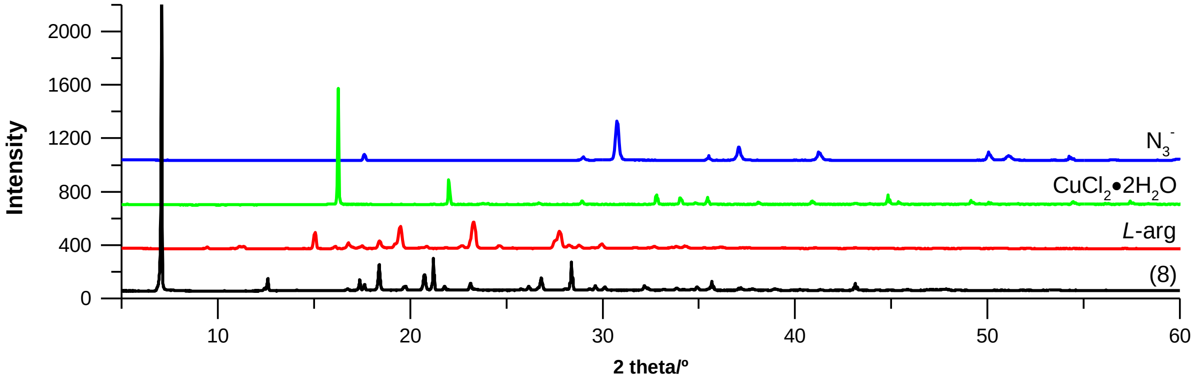

Figure S. 14 – PXRD pattern obtained for product 8 and for the ligands used in its synthesis. The data of **(8)** shows the presence of new peaks when compared to *L*-arg, $Cu(Cl_2)_2•2H_2O$ and N_3^-, indicating the formation of the metal complex.

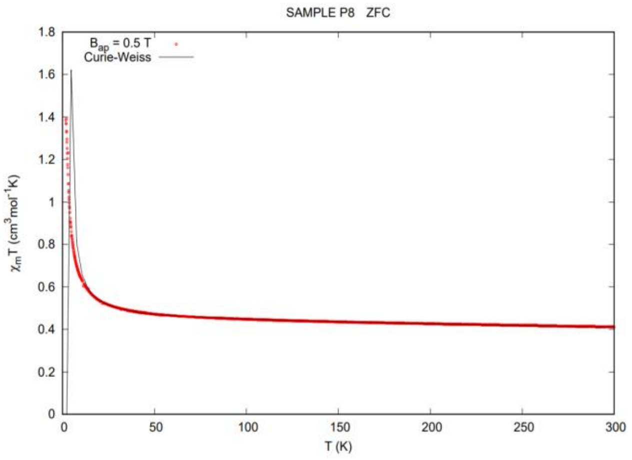

Figure S. 15 – Variation of the magnetic susceptibility in the $\chi_M T$ *versus* temperature form. The observed rapid increase of the $\chi_M T$ value in the low-temperature region suggests the presence of a weak ferromagnetic interaction.